TECHNICAL UNIVERSITY OF CRETE
ELECTRICAL AND COMPUTER ENGINEERING DEPARTMENT
DIGITAL IMAGE & SIGNAL PROCESSING (DISPLAY)
LABORATORY

BAND SPECIFIC OSCILLATIONS IN COMBINED EEG/MEG SOURCE ANALYSIS: CASE STUDY IN DRUG RESISTANT EPILEPSY

by

Glykeria Sdoukopoulou

A THESIS SUBMITTED IN PARTIAL FULFILLMENT OF
THE REQUIREMENTS FOR THE DIPLOMA OF
ELECTRICAL AND COMPUTER ENGINEERING

THESIS COMMITTEE

Professor Michail Zervakis, *Thesis Supervisor*
Professor Athanasios Liavas
Professor Carsten H. Wolters

Abstract

Objective: In the current study, we investigate the contribution of High Frequency Oscillations (HFOs) on the indication of the epileptogenic zone (EZ). We also study new approaches for the automatic detection of the non cerebral activity.

Motivation: We deployed an integrated pipeline for the detection of the EZ, incorporating HFOs-based and interictal spikes-based source analysis on a multi-focal epilepsy case. HFOs have been shown similar and/or better accuracy on the indication of the EZ compared to interictal spikes. Moreover, a combination of the non-invasive modalities electro- and magneto-encephalography (EEG) and (MEG), EMEG, has been shown to outperform single EEG or MEG in source analysis.

Novelty: In this thesis, we provide a patient-specific pipeline to investigate HFOs contribution on source localization compared to annotated interictal spikes. We have detected scalp HFOs on each modality using a thresholding technique in combination with an energy-based clustering approach. A calibrated realistic FEM head modelling is used to implement HFOs-based and interictal spikes-based source localization, independently.

Methods: The brain activity is recorded by EEG and MEG on a patient who suffered from multi-focal epilepsy. The first step for the EEG/MEG processing was the preprocessing, including filtering and artifact detection and correction methods in combination with information theory metrics. We also investigate new approaches towards the restriction of the non cerebral activity. Consequently, scalp HFOs are detected on both EEG and MEG. The detection algorithm consists of 3-phases sequentially implemented incorporating a thresholding technique, visual inspection and energy-based clustering approach. Source analysis is performed on detected HFOs and anno-

tated spikes. For each epileptic indicator, a solution to source localization is calculated, using the sLORETA algorithm, for different time instances and for each modality. A realistic head model including six tissue compartments, white matter anisotropy and calibrated skull conductivities has been used. A comparison between HFOs and interictal spikes-based source reconstructions is performed.

Results and Conclusions: Independently for HFOs and interictal spikes, four time instances have been chosen for each modality to explain better the underlying epileptic activity and the propagation phenomenon of the activity between the lesions. The results show that there is a concordance between the HFOs-based and spikes-based source estimation in all modalities. Although, single EEG and MEG source analysis indicates successfully the first less challenging lesion, their source reconstructions are far away from the second lesion. EMEG source reconstruction is able to indicate both lesions, revealing also a pathway between them, especially when using HFOs. Therefore, bi-lesional epileptic activity can be detected through the synergy of EEG and MEG with HFOs on the basis of realistic head model.

Keywords: Epilepsy, Interictal spikes, HFOs, EEG, MEG, FEM, Source Analysis

Περίληψη

Καινοτομία: Στην παρούσα μελέτη διερευνούμε τη συμβολή των High Frequency Oscillations (HFOs) στον εντοπισμό της επιλεπτογόνου περιοχής. Επίσης, διερευνούμε νέες μεθόδους αυτόματου εντοπισμού μη εγκεφαλικής δραστηριότητας.

Κίνητρο: Αναπτύξαμε ένα ολοκληρωμένο σύστημα ανίχνευσης της επιλεπτογόνου περιοχής, χρησιμοποιώντας HFOs και interictal spikes για την ανάλυση εγκεφαλικών πηγών σε περίπτωση ασθενή που πάσχει από πολυ-εστιακή επιληψία. Τα HFOs φαίνεται να εντοπίζουν ακριβέστερα την επιλεπτογόνο περιοχή συγκριτικά με τα interictal spikes. Ο συνδυασμός (EMEG) των μη επεμβατικών μεθόδων της ηλεκτρο- και μαγνητο- εγκεφαλογραφίας (EEG και MEG) δίνει καλύτερα αποτελέσματα από την κάθε μέθοδο ξεχωριστά στην ανάλυση πηγών.

Στόχος: Η παρούσα διπλωματική διερευνά τη συμβολή των HFOs στον εντοπισμό της επιλεπτογόνου περιοχής συγκριτικά με τα interictal spikes, υλοποιώντας τον αλγόριθμο εντοπισμού των HFOs και τεχνικές ανάλυσης εγκεφαλικών πηγών.

Μέθοδοι: Η καταγεγραμμένη εγκεφαλική δραστηριότητα μέσω των μη επεμβατικών μεθόδων της ηλεκτρο- και μαγνητο- εγκεφαλογραφίας, προέρχεται από ασθενή που πάσχει από πολυ-εστιακή επιληψία. Αρχικά τα σήματα προεπεξεργάζονται μέσω φιλτραρίσματος και τεχνικές ανίχνευσης και διόρθωσης του θορύβου. Επίσης, εξετάζουμε νέες μεθόδους περιορισμού της μη εγκεφαλικής δραστηριότητας. Εν συνεχεία, εφαρμόζεται ο αλγόριθμος ανίχνευσης των HFOs, ο οποίος αποτελείται από τρεις διαδοχικές φάσεις: μια μέθοδο κατωφλίωσης, την επιθεώρηση των σημάτων, καθώς και την ομαδοποίηση βασισμένη στην ενέργεια. Η ανάλυση των εγκεφαλικών πηγών βασίζεται τόσο στα ανιχνευμένα HFOs, όσο και τα σημειωμένα από επιληπτιολόγο interictal spikes. Η

λύση στο πρόβλημα εντοπισμού των εγκεφαλικών πηγών υπολογίζεται με βάση τον αλγόριθμο sLORETA, για διάφορες χρονικές στιγμές. Χρησιμοποιήθηκε, επίσης, ένα ρεαλιστικό μοντέλο κεφαλής, το οποίο απαρτίζεται από έξι (6) τμήματα ιστών, ανισοτροπία λευκής ουσίας και βαθμονομημένη διαγωγιμότητα κρανίου.

Αποτελέσματα και Συμπεράσματα: Η ανάλυση των εγκεφαλικών πηγών έχει γίνει σε τέσσερις (4) επιλεγμένες χρονικές στιγμές, με στόχο την καλύτερη απεικόνιση της υποβόσκουσας επιληπτικής δραστηριότητας και της διάδοσης της μεταξύ των κακώσεων. Σύμφωνα με τα αποτελέσματα υπάρχει συμφωνία των επιλεπτογόνων περιοχών που επιδεικνύονται τόσο από τα HFOs, όσο και από τα interictal spikes. Αν και η ανάλυση πηγών μέσω ηλεκτροεγκεφαλογραφήματος και μαγνητοεγκεφαλογραφήματος εντόπισε επιτυχώς την πρώτη μη απαιτητική κάκωση, η ανακατσκευή των εγκεφαλικών πηγών απέχει πολύ απο τη δεύτερη κάκωση. Η ανακατασκευή εγκεφαλικών πηγών βασισμένη στο συνδιασμό EMEG εντόπισε ακριβέστερα και τις δυο κακώσεις και αποκάλυψε το μονοπάτι-σύνδεσμο μεταξύ τους, ειδικά αξιοποιώντας τα HFOs. Συνεπώς, η διαταραγμένη εγκεφαλική δραστηριότητα από τις κακώσεις μπορεί να εντοπιστεί μέσω της συνέργειας του ηλεκτροεγκεφαλογραφήματος και μαγνητοεγκεφαλογραφήματος, χρησιμοποιώντας ρεαλιστικό μοντέλο κεφαλής.

Λέξεις Κλειδιά: Επιληψία, Ταλαντώσεις Υψηλών Συχνοτήτων, Ηλεκτροεγκεφαλογράφημα, Μαγνητοεγκεφαλογράφημα, Πεπερασμένο Μοντέλο Κεφαλής, Ανάλυση Πηγών

Acknowledgements

First of all, I would like to thank my supervisor Prof. Michail Zervakis for the opportunities that he gave me to prove myself, the trust that he showed, and the feedback throughout the process of my thesis. Furthermore, I would like to thank Dr. Marios Antonakakis for his guidance and patience that contributed highly in this work and for teaching me how the academic world operates. Additionally, I would like to thank Dr. Vasilios Tsiaras for his valuable advice regarding the HFOs detection part of this work.

I would also like to thank Prof. Carsten H. Wolters and Prof. Athanasios Liavas for giving their time to evaluate this work.

And especially my friends and family for their support.

Contents

List of Figures

Chapter 1

Introduction

1.1 Thesis Structure

The current study investigates a novel indicator of epileptic activity alongside with interictal spikes. The so-called High Frequency Oscillations (HFOs) are used to identify the seizure onset zone from measurements acquired by non-invasive electro- and magneto-encephalography (EEG and MEG) techniques. The aim and objective are presented at the end of this chapter, after addressing the framework of the current study. More specifically, the thesis structure proceeds as follows.

In **Chapter 2** the reader is introduced to the fundamental and theoretical knowledge of the topics covered in this thesis. The chapter starts with the basics of human brain anatomy and functionality, with emphasis on epilepsy. A short elaboration is given about the fundamental EEG and MEG operations, concluding with a comparison between the two measurement modalities.

Chapter 3 focuses on the theoretical background of this work, giving the mathematical formulations and derivations of the implemented algorithms and methodologies. Moreover, the pipeline of the thesis is elaborated. Beginning with the description of the preprocessing techniques, the next coming is the explanation of the semi-automated HFOs detection algorithm, including the clustering step. Consequently, the source analysis is fully defined, consisting of the definition and description of the forward and the inverse problem.

Chapter 4 presents all the experimental results. Furthermore a detailed pipeline of each module is explained. The chapter starts with the preprocessing results and the regarding explanations, it continues with the detection and clustering of HFOs. Finally, the results of spikes-based and HFOs-based

source analysis are presented for the EEG, MEG and combined EEG/MEG modalities.

Chapter 5 makes a comparison with other studies in order to highlight the new findings and discuss the value of the joint processing of EEG and MEG. Furthermore, it provides the concluding remarks and important methodological notes resulting from the current study.

Chapter 6 briefly introduces the reader to the user interface of the two toolboxes used on this thesis work: FieldTrip and Brainstorm. A concise comparison is made and the main merits of each toolbox are highlighted.

1.2 Aims and Innovation

The main aim of this thesis is to study the contribution of High Frequency Oscillations (HFOs) as indicators of epileptic activity. HFOs are used to identify the seizure onset zone. Also, annotated spikes are used for the seizure onset zone identification and a comparison between HFOs-based and spikes-based source analysis results is made. When the epileptic foci is distributed into more than one brain regions the diagnosis is getting complex, making the harmonization of several trials and modalities important. The goals of this thesis work are the following:

1. **First goal:** clean the recordings from the possible artifacts in order to increase the signal to noise ratio and assist source localization. EEG and/or MEG sensors record not only brain activity but also artifactual signals such as oculars, cardiac, muscular or head movements.

2. **Second goal:** detect and cluster scalp HFOs on EEG/MEG recordings. Because HFOs detection is a laborious and time consuming humans in the loop task, a semi-automated detection algorithm with a clustering approach is examined in order to assist epileptologist's work.

3. **Third goal:** study the concordance between source reconstructions using HFOs and Interictal Spikes. The capabilities of head modelling

and localization methods were examined, particularly using realistic head modelling with FEM and sLORETA, respectively.

4. **Forth goal:** study the potential of joint source analysis of EEG and MEG recordings. Even though this study examines an EEG dominant epilepsy case, MEG accurately detects epileptic activity on different brain regions. Nevertheless, EEG resolution is lower and its localization potential is weaker that MEG. Consequently, combined EEG/MEG source analysis takes into account the different characteristics of each modality and deploys EEG/MEG complementary nature.

These issues are studied in the next sections and applied on real EEG and MEG recordings, kindly provided by Prof. Carsten Hermann Wolters (University of Münster, Institute for Biomagnetism and Biosignalanalysis IBB).

1.3 Related work

Preprocessing methods for noise cancellation and artifact rejection have been widely used in every study of EEG and MEG. Filtering is the most common first step of fundamental noise reduction. Furthermore, component analysis, including PCA, ICA and SSP (especially for MEG recordings) has been widely examined in association with several pathologies, such as epilepsy, Parkinson and Alzheimer. The main goal is to accurately distinguish the artifactual from the cerebral sources and suppress the first ones, while the brain activity remains totally or almost totally unaffected. For the artifactual components' identification a lot of methods have been developed incorporating techniques both on time and time-frequency domain [1], [2], while machine and deep learning alongside with tensor decomposition have been introduced for EEG/MEG processing [3], [4], [5], [6]. High Frequency Oscillations (HFOs) detection algorithms are a subject undergoing intense studying. A variety of algorithms on time and/or time frequency domain has been implemented, incorporating thresholding or statistical techniques [7], [8], [9], [10], [11]. The most recent advances in presurgical epilepsy diagnosis

integrate detection of scalp HFOs [12]. Also, recent studies use machine or deep learning approaches for HFOs detection [13]. Localization of the brain activity of interest has been widely exploited for both EEG and MEG recordings. Interictal spikes are well-established indicators of epileptic activity and they have been extensively used for the identification of the epileptogenic zone [14], [15]. Combined EEG/MEG source analysis is an emerging approach for solving the Forward Problem as it yields superior results in terms of source estimation according to studies [16], [17], [18]. On the other hand, HFOs are newly introduced indicators of epileptic activity, meaning that they are not a fully exploited research topic [19]. Studies show that scalp and intracranial HFOs represent the same brain phenomena. Localization of scalp HFOs is an emerging research topic, with a limited number of studies examining HFOs-based source analysis on MEG recordings [12], [20].

Chapter 2

Fundamentals

In this chapter all the medical background and the description of the modalities are given. The chapter begins with a brief description of the anatomy of the human head and continuous with the explanation of the Nervous System. This thesis work study a focal epilepsy case, so a definition of focal epilepsy as a disorder is given including the definition of interictal spikes, High Frequency Oscillations (HFOs) and the applied focal epilepsy treatments. Finally, EEG and MEG modalities are explained, while a comparison between them is made. Also, the advantages of combined EEG/MEG are highlighted, especially when studying focal epilepsy cases.

2.1 Anatomy and Physiology of the Human Brain

Brain is the most complex organ, responsible for processing all body functions, integrating, and coordinating the information it receives from the sense organs, and making decisions, accordingly. It is enclosed by the skull and it is surrounded by the CSF that is also flowing inside the brain through the cerebral ventricles. Additionally, brain is the most important organ of the nervous system. It consists of the cerebrum, diencephalon, cerebellum and brainstem (Fig. 2.2a [1]). The Nervous System comprises of nerves and neurons that transmit electrical and chemical signals across all body parts. A typical neuron consists of a cell body (soma), dendrites, and an axon with an axon terminal. The electrical impulses that are conveyed by the signals are called Action Potentials (AP) and are caused when the neuron's membrane

[1] https://www.visiblebody.com/learn/nervous/brain

potential temporary changes from negative to positive (Fig. 2.1a). This potential shift is caused by the abrupt influx and outflow of ions.

Cerebrum is the largest part of the brain and its outer segment (cerebral cortex) consists of the right and left cerebral hemispheres. Each hemisphere controls the bilateral part of the human body and they are responsible for the performance of higher intellectual functions. The cerebral hemispheres consist of the grey matter which is the outer layer and the white matter which is the inner layer. The outer layer of the grey matter is called cerebral cortex (2.1b). The cerebral cortex is about 3mm thick and takes over almost half of the weight of the brain. The surface is highly folded, forming ridges and valleys which are called gyri and sulci, respectively. The distinct fissures of the cerebral hemispheres divide the brain into four lobes (2.2b [2]) for each hemisphere.

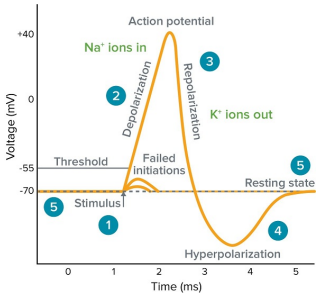

(a) The states of the Action Potential (AP). Adapted from https://www.moleculardevices.com.

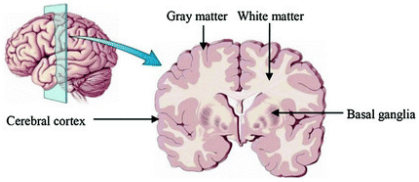

(b) Cerebrum consists of the grey and white matter. Grey matter is the outer layer of the cerebrum, while the inner layer is called white matter. The outer layer of the grey matter is called cerebral cortex. Adapted from *Autism Spectrum Disorder: Brain Images and Registration.*

Figure 2.1: Action Potential and cerebral cortex.

Diencephalon located in the central region of the brain, it i responsible for the relay and process of the sensory information and the autonomic control.

Cerebellum is located underneath the cerebrum and coordinates muscle movements, maintain posture, and balance.

[2] https://www.nbia.ca/brain-structure-function/

Brainstem relays signals between the cerebrum, cerebellum and to the spinal cord. It is responsible for automatic functions.

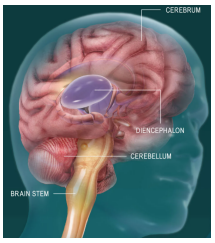

(a) The compartments of the human head.

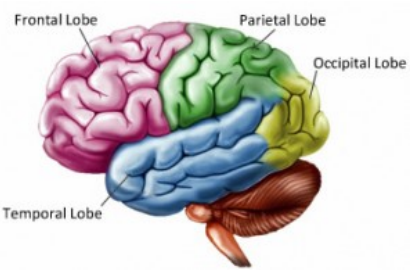

(b) Brain lobes.

Figure 2.2: Brain compartments and lobes.

2.2 Epilepsy

2.2.1 Epilepsy as a Disorder

Epilepsy is a common central nervous system disorder, affecting 1% of people worldwide and 2% in EU. More than 5 million cases are diagnosed annually. It has been estimated that approximately 7%–8% of the global population have at least 1 epileptic seizure during their lifetime. Epilepsy is expressed as an unconscious recurrent occurrence of synchronous electrical discharges in cerebral cortical neurons, called epileptic seizures. It is caused by temporally abnormal brain activities which result in uncontrollable and unconscious jerking, temporary confusion, loss of consciousness and awareness and feelings such as fear, anxiety or déjà vu. Each type of seizure may be expressed with different symptoms. Commonly, the patients show the same type of epileptic seizure during each episode, so the symptoms will be similar each time.

2.2.2 Focal Epilepsy

The main categories of epilepsy are the grand mal, the petit mal, and the focal epilepsy [21]. In this thesis, only focal epilepsy has been studied. This type of epilepsy can arise from any lobe of the brain or deeper structures of

brain stem. Initially, it affects only one part of the brain which is the whole hemisphere or a part of the lobe from which the seizure generated. Usually, focal seizures arise from brain lesions due to a brain injury, brain infection, or functional abnormalities such as a tumor region. The surface of this cortical region varies from a few millimeters to centimeters. The semiology of these seizures depend on the brain region in which the synchronous electrical discharges are generated. In this research work, the case study is a frontal lobe epilepsy. Usually, frontal lobe seizures last less than 30 seconds and tend to occur at night. Due to the numerous connections between the frontal and temporal lobe, it can be difficult to determine which section of the brain is being affected.

2.2.3 Interictal Spikes

Generally, spikes are generated by the synchronous electrical discharges of a group of neurons [22]. Interictal spikes are the spikes detected between seizures (interictally). Also, they may occur before (preictally), during (ictally) and after (postictally) a seizure. They are correlated with epilepsy because the brain region that generates them is highly associated with the epileptogenic zone. The epileptogenic zone (EZ) is defined as the cortex area responsible for the epileptic seizures initiation (EZ is integral for the epileptic seizures). An alternative definition of the epileptogenic zone is the *minimum amount of cortex that must be resected (inactivated or completely disconnected) to produce seizure freedom* [21]. The seizure onset zone is the cortex area that actually generates the epileptic seizures [21]. The volume of tissue that is responsible for the interictal spikes generation is called irritative zone (IZ) [23]. To mention that interictal spikes are a part of the interictal discharges and they are followed by sharp waves. Interictal discharges express high amplitude ($> 50\mu V$), interictal spikes have less that 50ms duration and sharp waves last from about $50ms$ to $200ms$ [14].

2.2.4 High Frequency Oscillations

High Frequency Oscillations (HFOs) have been emerged as a new biomarker in epilepsy. The frequency band that is mainly used in the majority of clinical cases is below 100 Hz. However, HFOs can be found on the frequency band between 80Hz and 500Hz and they are excessively studied in order to understand their contribution in epilepsy. HFOs are divided into two categories: ripples (80Hz-250Hz) and fast ripples (250Hz-500Hz) [24]. Studies [25] indicate that some ripples may exist physiologically in the brain and they are associated with memory consolidation. On the other hand, fast ripples are highly connected with the epileptogenic cortex [26]. Frequency itself is not adequate to determine if HFOs are pathologically or not. For example, ripples generated by the dentate gyrus are always connected with epileptic activity [27]. The classification of HFOs as pathological or normal is still under investigation [27]. Probably, normal ripples are generated by the summation of synchronous IPSPs generated by subsets of interneurons that regulate the discharges of principal cells, while fast ripples often reflect the synchronized firing of abnormally bursting neurons [26], [27]. Invasive EEG recording methods serve as the golden standard for HFOs study. However, studies have shown that HFOs can be recorded using scalp EEG and MEG [19], [28], [12]. In order to catch HFOs the sampling frequency of the recordings must be at least 2000Hz and it is advisable to acquire the measurements during the NREM sleep. Regarding to spikes, HFOs can be detected in three different ways: (1) HFOs visible in spikes (2) HFOs invisible in spikes (3) HFOs independent of spikes [29]. According to literature most HFOs occur the same time with spikes [29], [28].

2.2.5 Focal Epilepsy Treatments

The most common treatment is the anti-epileptic drugs, which help approximately 60% of the patients to become seizure free after the initial dose (WHO, 2019). Additional medication can be slightly more effective, since the 70% of the patients will be seizure free. A proportion of 30% of patients suffer from refractory epilepsy. For those cases the most promising treatment option is

the epilepsy surgery (WHO, 2019). The holy grail in epilepsy surgery is to find the brain regions responsible for generating the epileptic activity. The aim of the presurgical evaluation is to precisely define the epileptogenic zone (subsection 2.2.3). The cortical zones that should be well defined during the presurgical evaluation are the [21]:

- Irritative zone (subsection 2.2.3), which is measured by invasive or non-invasive EEG, and functional magnetic resonance imaging (fMRI)
- Seizure-onset zone (subsection 2.2.3), which is mainly defined by invasive or non-invasive EEG, but can also be defined by ictal SPECT and to a lesser degree by fMRI and MEG
- Symptomatogenic zone, which is the cortex area that generates the symptoms when it is activated. This area is obtained by studying the initial seizure symptomatology.
- Epileptogenic lesion, which is the lesion responsible for the epileptic seizures. This cortex area is defined by high resolution MRI.
- Functional deficit zone, which is the dysfunctional cortex area during the interictal period. This area can be defined by using surrogate tests including neurological examination, neuropsychological examination and functional imaging (interictal SPECT and PET).

The cortical zones are devided into practical and theoretical and they are defined using the aforementioned methods [21]. The concept of the theoretical and practical zones ban be understood mentioning that spikes are generated, also, by the irritative zone which is not overlapping with the epileptogenic zone. Often, the scalp recordings underestimate the extent of the irritative zone, while the invasive recordings cannot detect accurately the irritative zone. Consequently, for a seizure-free surgical outcome, the accurate definition of the zones is integral.

2.3 Non-invasive Measurement Modalities

2.3.1 Electroencephalography

Electroencephalography (EEG) [30] is the recording method for brain's electrical activity using electrodes forming the electrode cap which is placed on the scalp surface. The activity measured is generated by the pyramidal cell 2, 3 and 4 that are perpendicularly oriented to the cortex surface. The EEG system consists of the electrodes that measure brain's electrical activity, the differential amplifier, the amplifiers that enhance the signal, low-pass and high-pass filters and an analogue to digital converter (ADC) in order to digitize the signal and transfer it to the computer or a needle (pen)-type register to draw the signal on the paper.

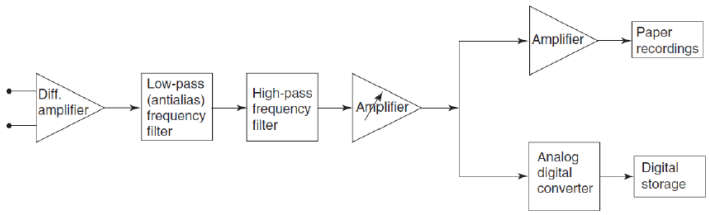

Figure 2.3: The EEG system diagram of a single channel, adapted from Wiley Encyclopedia of Biomedical Engineering, Copyright © 2006 John Wiley & Sons, Inc.

In multichannel recording systems the electrodes' positions are determined either by the 10-20 system (international system) or the $10-10$ system. The 10-20 system consists of 21 electrodes that are placed within a distance of 10% or 20% of the total front–back or right–left distance of the skull measured by the anatomic landmarks on the skull. These landmarks are the nasion (Nz), the inion (Iz) and the left and right pre-auricular points (A1 and A2). For higher density EEG measurements the $10-10$ system can be used, which consists of 75 electrodes. Each channel of EEG measures scalp's electric potential between the current channel and the reference channel in metric units μV. The reference channels depend on the montage that is used (e.g. it could be another electrode, common average reference etc.) to better display and review the data.

The electrodes names are coded regarding their location. The first letters denotes the brain area that the positions are located: Fp (Frontal pole), F (Frontal), C (Central), P (Parietal), O (Occipital) and T (Temporal), while the remaining letter can be either a number or the z letter; if it is an even number, then the position is located on the right side, if it is an odd number on the left side, while the letter z (stands for zero) implies a central position.

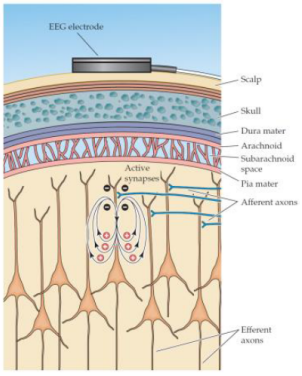

(a) The EEG electrode on the scalp. Adapted from Purves, et al., 2004.

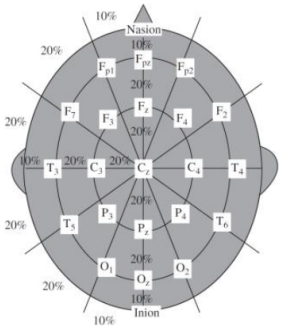

(b) The 10-20 system with 21 electrodes. Adapted from Sanei & Chambers, 2007.

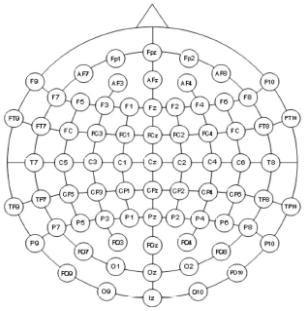

(c) An EASYCAP EEG cap with 74 electrode positions (10/10 System) as adapted from (https://www.easycap.de)

2.3.2 Magnetoencephalography

The synchronous electrical activation of neurons generate a weak perpendicular magnetic field that can be recorded using the Magnetoencephalography (MEG) [31], [32]. The amplitude of the measured signals is in fT. MEG is very sensitive to ambient magnetic fields, which are several orders of magnitude stronger than the MEG. Consequently, the MEG system is placed inside a magnetically shielded room (MSR). For instance, the magnetic noise in a typical laboratory is approximately thousand times stronger than the magnetic fields generated by brain activity while the earth's static geomagnetic filed is $8-9$ orders of magnitude stronger. Due to the very low signal-to-noise ratio of MEG, preprocessing techniques such as filtering, artifact detection, removal and averaging are highly recommended.

MEG signals can be detected only by superconducting *SQUID* (Superconducting Quantum Interference Devices) sensors. In order to achieve the

critical temperature T_c at which the materials switch from the normal to superconducting state, a coolant is necessary. In MEG, the most common coolant is liquid helium, with boiling point $4.2K$. Because of the small SQUIDs' diameter (ranges between a low of $0.9mm$ to a high of a $1.7mm$), the coupling to the magnetic field is poor. In order to improve the coupling superconducting *flux transformers* are used, which collect magnetic flux from a larger area and fed it into the SQUID loop. The coils (*pick-up coils*) more close to the head, collect the magnetic flux, a second optional coil is located in distance (*compensation coil*) and finally a *signal coil* is located on top of the SQUID loop. The two main configurations are:

1. the magnetometer, which is the simplest form with a single coil only, without compensation. It is sensitive to nearby and far away (possible ambient noise) sources. This configuration measures the magnetic field component with direction perpendicular to the surface of the pick-up coil.

2. the gradiometers, which consist of a magnetometer with a compensation coil and measures the spatial gradient of a magnetic field component. When the coils are placed in opposite directions, the noise magnetic fields do not couple to the SQUID and as a result they cannot capture distant ambient fields. Gradiometers are divided into *axial* and *planar* depending on the coil's position. The former measures the change of the radial field component along the radius since the coils are placed along the same radial axis, while on the latter the coils are placed side-by-side.

MEG does not take into account the position of the head. In order to solve this problem prior the measurement, $3-5$ Head-Position Indicator (HPI) coils are placed on fiducial landmarks of the head, for storing information of the head's position. MEG and MRI are usually measured on the same coordinate system in order to visualize MEG results on anatomical MRIs.

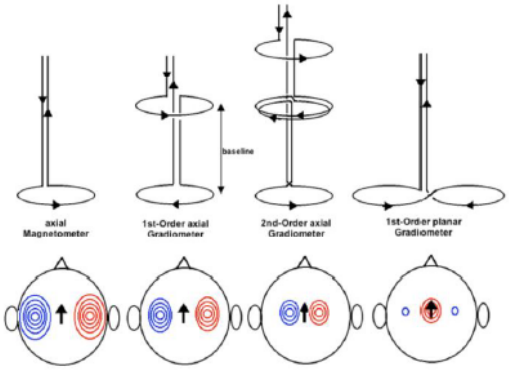

(a) Different types of pickup coils measuring the magnetic field of a source (black arrow adapted from, Singh 2006)

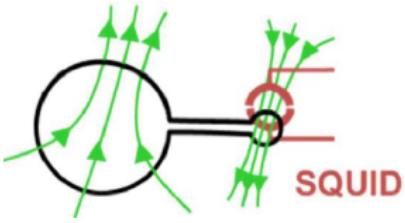

(b) A flux transformer with magnetometer that collects the magnetic flux and conveys it to the SQUID, adapted from Galán et al. 2013.

2.3.3 Comparison between EEG and MEG

Although EEG and MEG measure electrophysiological activities of the same underlying brain sources, the measuring process is different alongside with the recorded signals [33], [34]. Firstly, EEG and MEG are complementary to each other. EEG electrodes touch the scalp surface of the human head, while the MEG sensors are not in direct contact with scalp. The main advantages of EEG and MEG are the high temporal resolution in the range of milliseconds (ms) and the ability to measure the electrical brain activity directly compared to functional neuroimaging methods such as functional MRI (fMRI), that utilize indirect phenomena such as metabolic changes like blood oxygenation. However, spatial resolution of EEG and MEG is usually lower than fMRI and their sensitivity is getting weaker for deeper sources [33]. EEG can detect efficiently both quasi-radial and quasi-tangential sources, while MEG is sensitive to the quasi-tangential sources only [34], [35], [36]. Also, MEG is less sensitive to deeper sources, because they are more radially oriented. On the contrary, MEG signals have higher SNR for more superficial sources because the quasi-radial biological noise contaminates more the EEG signals [37]. The signal topographies of EEG and MEG are almost orthogonal to each other. The distance between the poles of the EEG topographies is greater than for MEG because the low skull conductivity smears out the

EEG. Consequently, combined recordings of EEG and MEG are likely to improve source analysis as they complement each other regarding the source types and orientations detected by both modalities [34], [38]. However, EEG and MEG measure signals of different quantity, leading to different units. To perform a combined source analysis both modalities need to be transferred to a common space. An SNR based transformation [39] is used in the current thesis. In this approach, the data are whitened according to the noise level of each channel to obtain unitless measurements for EEG and MEG. The EEG and MEG leadfield matrices and measurements are stacked in a row wise form after normalization with SNR to make them unitless [39].

In focal epilepsy, it has been shown that EEG and MEG can detect different interictal spikes indicating that the simultaneous acquisition of EEG and MEG yields complementary diagnosis [40], [41]. Iwasaki et al. [40] reported that MEG detects spikes on 19% of patients, EEG on 2% of patients, while both EEG and MEG detect spikes on 72% of patients. Similarly, Knake et al. [41] reported EEG spikes on 3% of patients, MEG spikes on 13% of patients and EEG/MEG spikes detected on 75% of patients. Aydin et al. showed in a single epilepsy case that combined EEG/MEG outperforms single EEG or MEG source analysis using calibrated and realistic head modeling, comparing the results with stereo EEG recordings. These results make clear that the different sensitivity profile of EEG and MEG could bring source localization closer to the epilepsy foci. Such a complementary result is presented in this thesis.

Chapter 3

Theoretical Background

In this chapter the theoretical background of all implemented methods and algorithms is given. The aim is to introduce the reader to the basic concepts of the mathematical and algorithmic background, giving brief and concise derivations. In Fig. 3.1 is shown the high level pipeline of this thesis work. The analysis of the methods follows the pipeline. To explain, the chapter begins with the definitions and derivations of the implemented *preprocessing techniques*, it continuous with the statement of the *HFOs detection algorithm* and it concludes with the *source analysis* theory.

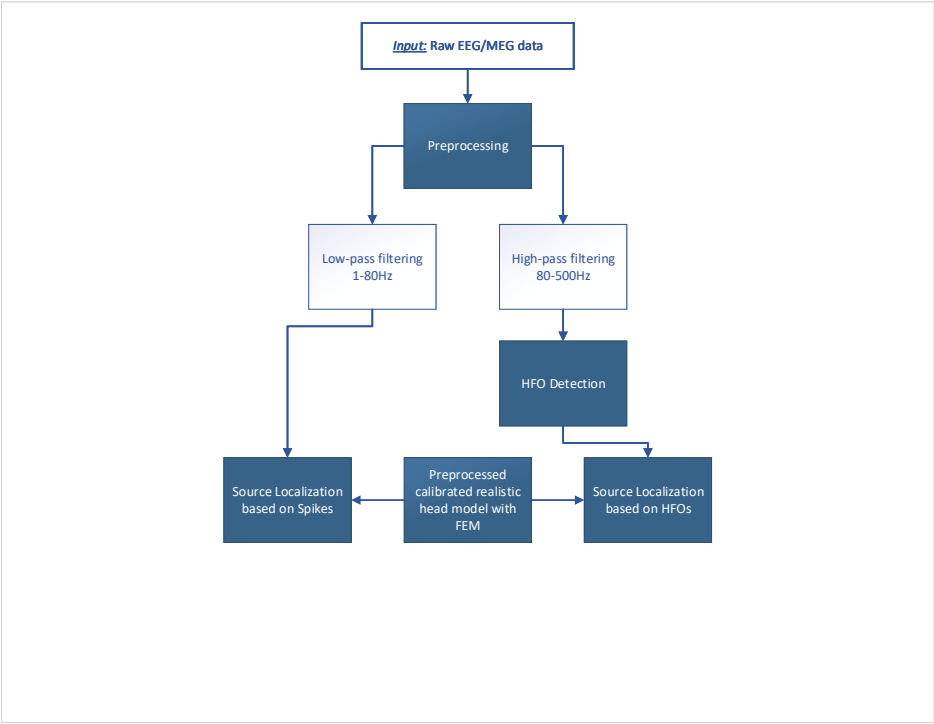

Figure 3.1: Schematic diagram of thesis.

3.1 Preprocessing Techniques

3.1.1 Downsampling and Filtering

The first step of the preprocessing pipeline is to downsample the data in order to reduce algorithms' time complexity. It is important to realize that downsampling affects only data's size in a way that time data points are numerically decreased.

Baseline Correction is another preprocessing step. The raw MEG and EEG signals from the sensors typically have a large offset. Related to MEG signals, this offset is caused by SQUID behavior which is periodic in applied flux and there is no zero level. Furthermore, there will be some low-frequency noise from the SQUIDs and slow ambient field fluctuations. In order to correct these low frequency effect, the first approach is to subtract the average value of the data across specific time intervals from the signal of each channel [42]. The interval is defined as the baseline and it must be long enough for an accurate estimate of the DC value at each sensor. Another approach is the implementation of a high pass filter with a low cut-off frequency ($< 0.3Hz$) applied on the continuous raw data. The last approach is highly recommended not to be applied on shorter epoched data since it will cause edge effects.

Apart from time domain, data are usually examined on frequency domain, where Energy Spectral Density (ESD) [43] can be calculated. Biosignal's mapping into frequency domain allows the examination and evaluation of filtering implementation, through the calculation of ESD. The continuous-time biosignals are represented to frequency domain, using Frequency Transform. Specifically, Frequency Transform is given by the following equation:

$$X(F) = \int_{\infty}^{\infty} x(t) e^{-j2\pi ft} dt, \tag{3.1}$$

where x(t) is the initial continuous-time signal and $e^{-j2\pi ft}$ is the so called phasor. To put it differently, the function $X(F)$ is called Fourier Transform of function $x(t)$ and it describes uniquely the latter on frequency domain.

$X(F)$ function shows the linear combination of complex exponential signals ($e^{-j2\pi ft}$) that comprise $x(t)$. ESD of a signal $x(t)$ describes energy distribution into frequency components that composite that signal. Given that ESD is more suitable for transients, such as brain signals, Parseval's Theorem gives the expression for the signal's energy:

$$E_{xx} = |X(F)|^2 = X^*(F)X(F), \tag{3.2}$$

where X^* is the conjugate of X.

After downsampling, the next step is filtering the frequency band of interest and the Power Line Noise (PLN) and its harmonics.

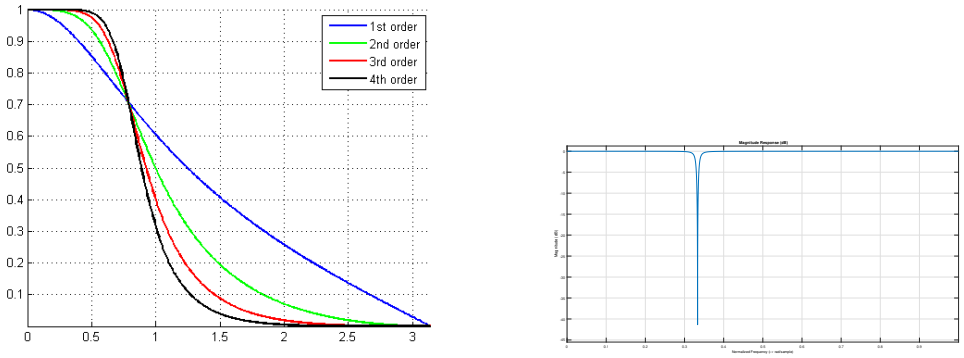

(a) Transition band of different orders of Butterworth filter[1].

(b) Cut-off frequency of Notch filter at 50Hz

Figure 3.2: Filters used on preprocessing.

3.1.2 Decomposition Methods

In the previous section, filtering was examined, to a certain degree, as a simple denoising method. Due to multichannel recordings among with cerebral activity many other physiological and non-physiological activities can be captured. For the purpose of detection and restriction of those undesirable

[1] https://dsp.stackexchange.com/questions/34127/higher-order-butterworth-filters

activities, more sophisticated methods are needed.

In this section, Component Analysis techniques are described, as they have been widely used in computational neuroscience in order to perform dimensionality reduction and data cleaning. More specific, Principal Component Analysis (PCA) performs dimensionality reduction, decreasing computational complexity, and creates new uncorrelated variables that consecutively maximize variance. On the other hand, Independent Component Analysis (ICA) searches for statistically independent components. Frequently, PCA can precede ICA as the combination of those techniques yield optimal results.

Principal Component Analysis

PCA is a statistical linear transformation technique. The goal is to compute a new basis as a linear combination of the original which better re-expresses the data. Particularly, PCA projects data samples onto a new subspace with equal or fewer dimensions than the original ones. The orthogonal axes of the subspace are the principal components, the directions of maximum variance, with the smaller total error (smaller total length of projections) [44]. Whitening is a linear transformation applied on data through PCA. In detail, transforms data's covariance matrix into identity matrix, meaning that data are uncorrelated, with unit variance.

There are two algebraic solutions of PCA: *(1)* based on Singular Value Decomposition (SVD), more general solution, and *(2)* based on the Eigenvalue Decomposition (EVD) of the covariance matrix [45]. The aforementioned solutions are briefly derived below. PCA can also be implemented prior to ICA in order to determine the optimal number of Principal Components which is equal to the Independent Components. In more detail, the number of PCs is determined by Percentage of Useful Information (PUI) [46], a metric defined as follows:

$$PUI_i = 100\frac{Eigenvalue_i}{\sum_{j=1}^{m} Eigenvalue_j}(\%), \tag{3.3}$$

where m stands for channels' number. The eigenvalues used as they resulted from PCA. To explain, the sum of PUI_i is equal to unit, hence only the *top-k* components survived with the highest PUI and sum approximately equal to 95%. In other words, the number of components which their sum is at least 95%, are those who explain better the data.

It is important to mention that EVD can be applied only on diagonalizable matrices (so the matrices must be square, too).

Mathematical formulation

Let X and Y be mxn matrices related by a linear transformation P. X is the original recorded data and Y is a re-presentation of that data:

$$Y = PX, \tag{3.4}$$

where Y stands for PCs. PCA's goal, as explained above, is to convert the covariance matrix into the identiy. Mathematically expressed:

$$S_y = \frac{1}{n-1} YY^T = I, \tag{3.5}$$

where S_y is the covariance matrix of Y. In particular, the aim is to find a matrix P such that S_y is diagonalized. The rows of P are the principal components of X. Using the (3.5):

$$\begin{aligned} S_y &= \frac{1}{n-1}(PX)(PX)^T \\ &= \frac{1}{n-1} PXX^T P^T \\ &= \frac{1}{n-1} P(XX^T)P^T \\ &= \frac{1}{n-1} PAP^T \end{aligned} \tag{3.6}$$

where $A \equiv XX^T$is the covariance matrix of X and it is symmetric. Given that A is symmetric, EVD can be applied:

$$A = EDE^T, \tag{3.7}$$

where D is a diagonal matrix and E is a matrix containing the eigenvectors of A. Each row of matrix P is an eigenvector of XX^T, so $P \equiv E^T$. Substituting into (3.7) $A = P^T DP$ and considering $P^{-1} = P^T$:

$$\begin{aligned} S_y &= \frac{1}{n-1} PAP^T \\ &= \frac{1}{n-1} P(P^T DP)P^T \\ &= \frac{1}{n-1} PP^T DPP^T \\ &= \frac{1}{n-1} PP^{-1} DPP^{-1} \\ &= \frac{1}{n-1} D \end{aligned} \tag{3.8}$$

It is obvious that the choice of P diagonalizes S_y and the PCs of X are the eigenvectors of XX^T or the rows of P.

Principal Component Analysis and Singular Value Decomposition

Singular Value Decomposition (SVD) is a factorization of a real or complex matrix (not necessarily square) that generalizes the EVD approach. Applying SVD on a matrix X_{mxn} (m is the number of channels and m the number of samples):

$$X = U\Sigma V^T, \tag{3.9}$$

where U is orthogonal matrix, such as V and I is diagonal. Keeping in mind the previously defined matrix X and given that Y is an nxm matrix:

$$Y = \frac{1}{\sqrt{n-1}} X^T, \tag{3.10}$$

where each column of Y has zero mean. Analysing YY^T:

$$\begin{aligned} Y^T Y &= (\frac{1}{\sqrt{n-1}} X^T)^T (\frac{1}{\sqrt{n-1}} X) \\ &= \frac{1}{\sqrt{n-1}} (X^T)^T X^T \\ &= \frac{1}{\sqrt{n-1}} X X^T \\ Y^T Y &= S_X \end{aligned} \tag{3.11}$$

where S_X is the covariance matrix of X.

To explain the above:

- The covariance matrix of X equals the $Y^T Y$.
- As derived above, PCs of X are the eigenvectors of S_X.
- The columns of matrix V, as it resulted from SVD calculation of Y, contain the eigenvectors of $Y^T Y = S_X$.
- As a consequence, the principal components of X are the columns of V.
- To put it differntly, V spans the row sapce of $Y \equiv \frac{1}{\sqrt{n-1}} X^T$, so spans the column space of $\frac{1}{\sqrt{n-1}} X$. To sum up, finding the principal components is equivalent with finding an orthogonal basis that spans the column space of X.

Blind Source Separation

Blind Source Separation (BSS), generally speaking, involves the analysis of mixtures of signals. The most common case of BSS, is the cocktail party

problem [47]. The cocktail party problem can be described, for instance, as the process of distinguishing the source of a specific sound among others, in a noisy and crowd party. BSS is the separation of a set of source signals from a set of mixed signals, without a priori knowledge (or with very little information) about the source signals or the mixing process. General BSS model is given below:

$$x(t) = As(t) + n(t), \tag{3.12}$$

where $s(t)$ are the signals' sources, $x(t)$ are the mixed signals and $n(t)$ stands for noise. Noise can be added by the measurements errors or the model's deficiency. The goal is to estimate the unknown mixing matrix A and the original sources of the signal when only the mixed signals s are known. The most common technique of BBS is the Independent Component Analysis, as explained below.

Independent Component Analysis

Independent Component Analysis (ICA) is a special case of BSS and was initially developed to resolve problems closely related to the cocktail party problem. ICA have been applied on many different scientific cases, such as EEG and MEG data. EEG and MEG data are generated by mixed brain activity either cerebral or non-cerebral. ICA's goal is to divide the initial multivariate signal into Independent Components (ICs) [48]. The assumptions made are:

- $x(t)$ should be a linear combination of statistically independent sources $s(t)$ that have either non-Gaussian or at least one Gaussian distribution.
- The observed data $x(t)$ should be standardized (unit variance and zero mean) and whitened (uncorrelated) using PCA.
- The mixing matrix A should be full rank.

More precisely, statistical independence holds when the joint probability

density function (pdf) of sources is equal to the product of sources' probability functions. Mathematically defined:

$$p(s_1, s_2, ..., s_i) = \Pi_i p(s_i) \tag{3.13}$$

where $s_1, s_2, ..., s_i$ are random variables. It is important to mention that statistic independence is stronger than uncorrelation since independence involves uncorrelation, but not vice versa. The key point on estimating the ICA model is non-gaussianity. To put it differently, one way to implement ICA is the maximization of non-gaussianity, since ICA allows only one (maximum) source at the time to be independent. Dependence is strongly connected with the Central Limit Theorem which tells that the distribution of a sum of independent random variables tends toward a gaussian distribution, under certain conditions.

On the other hand, there are some ambiguities about ICA. Firstly, the variances (energies) of the independent components cannot be determined. To explain, both s and A are unknown, so any scalar multiplier of the sources s_i could always be cancelled by dividing the corresponding column a_i of matrix A by the same scalar. Secondly, the order of the independent components cannot be determined. Again, both s and A are unknown, so the order of the terms in the sum can be freely changed and call any of the independent components the first one.

In order o define ICA a statistical 'latent variables' model have been used. Assume the observation of n linear mixtures $x_1, .., x_2$ of n independent components.

$$x_j = a_{j1}s_1 + a_{j2}s_2 + ... + a_{jn}s_n, \tag{3.14}$$

for all j, where $s_1, s_2, ..., s_i$ are the original source signals and $a_{j1}, a_{j2}, ..., a_{jn}$ are environmental parameters. Both signals $s(t)$ and a parameters are un-

known. For the purpose of estimating a parameters, it is enough to rely on the statistical properties of signals $s(t)$ and assume their statistical independence at each time instant t. Re-expressing the aforementioned sum by vector-matrix notation: x denotes the random vector with elements the mixtures $x_1, x_2, ..., x_n$ and s the random vector with elements $s_1, s_2, ..., s_i$. Finally, matrix A is called mixing matrix and is a square full-rank matrix. Each column a_k of mixing matrix A represents the mixing weights for all K sources. According to the previous the above mixing model can be written as follows.

$$\mathbf{X}=\mathbf{A}s \tag{3.15}$$

With this in mind, ICA model is transformed into the following equation and endeavors to estimate unmixing matrix W, which is as close as possible to A inverse.

$$\mathbf{S}=\mathbf{W}\mathbf{X} \tag{3.16}$$

Important steps prior to ICA are centering and whitening techniques. Specifically, centering refers to the calculation of vector's x mean value and its subtraction such as to make x a zero-mean variable. As mentioned on the Subsection 3.1.2, whitening yields uncorrelated components with unit variance. The mathematical formulation of whitening follows below.

First of all EVD is applied on the given data X:

$$E\{XX^T\} = EDE^T \tag{3.17}$$

The goal is to convert data X into uncorrelated variables Y, where $Y = PX$ and the covariance matrix of Y is diagonal. So,

$$\begin{aligned} E\{XX^T\} &= ED^{\frac{1}{2}}D^{\frac{1}{2}}E^T \\ &= E\{P^{-1}YY^TP^{-T}\} \\ &= P^{-1}E\{YY^T\}P^{-T} \end{aligned} \tag{3.18}$$

By observation:

$$P = D^{-\frac{1}{2}} E^T$$

Finally, Y matrix can be written:

$$Y = P^{-\frac{1}{2}} E^T X \tag{3.19}$$

As a result the mixing matrix A is transformed into:

$$\tilde{A} = D^{-\frac{1}{2}} E^T A \tag{3.20}$$

It is evident that whitening reduces the number of parameters to be estimated. Instead of estimating n^2 parameters that are the elements of the original matrix A, only the new orthogonal matrix $\tilde{A}$ is estimated with $n\frac{n-1}{2}$ degrees of freedom.

Apart from whitening, the definition of independence governs the form of ICA algorithm. The most common approaches for independence are the *(1)* maximization of non-gaussianity and the *(2)* minimization of mutual information [49]. To put it differently, ICA measures high-order statistics such as Mutual Information, Negentropy and Kurtosis.

A classical method of non-gaussianity is kurtosis. Kurtosis is the forth standardized moment of a distribution and a measure of the "tailedness". For a more detailed explanation see subsection (3.1.3).

Another important measure of non-gaussianity is negentropy. Negentropy measures the difference in entropy between a given distribution and the Gaussian distribution with the same mean and variance. Negentropy is always non-negative. It is defined as follows:

$$J(s) = H(s_{gauss}) - H(s) \tag{3.21}$$

where s_{gauss} is a gaussian random variable, which its covariance equals s and

H stands for the entropy of a discrete random variable s_i, defined as follows:

$$H(x) = -\sum_{i=1}^{n} P(x_i) \log_b P(x_i) \tag{3.22}$$

Entropy is equal to zero if and only if the variables are statistically independent and it is always non-negative. The main disadvantage of negentropy is the computational complexity, since the pdf estimation is required in many cases.

Mutual Information (I) is the natural measure of the dependence between random variables. Mutual Information between m scalar random variables $y_i = 1, ..m$ is defined as follows:

$$I(y_1, y_2, ..., y_m) = \sum_{i=1}^{m} H(y_i) - H(y) \tag{3.23}$$

Furthermore, for y_i of unit variance entropy and negentropy differ only by a constant and a sign.

$$I(y_1, y_2, ..., y_m) = C - \sum_{i} J(y_i) \tag{3.24}$$

Extended Infomax Algorithm

The two most well known algorithms which implement ICA is Infomax and FastICA [50]. The first one, aims on the maximization of mutual information and the second one aims on the maximization of non-gaussianity. The initial Infomax algorithm implemented by Bell and Sejnowski (1995) [49], is based on an unsupervised learning algorithm and aims to maximize entropy in a single layer feed forward neural network. It is important to mention that the algorithm is effective in separating sources with super gaussian distributions while fails to separate sources with negative kurtosis. Let's assume that x is the input to the neural network whose outputs are of the form $\phi(\mathbf{w}_i^T x)$, where ϕ_i are non-linear scalar functions and $\mathbf{w}_i$ are the wight vectors of the

neurons. The goal is to maximize the entropy of the outputs:

$$L_2 = H(\phi_1(\mathbf{w}_1^T x), ..., \phi_n(\mathbf{w}_n^T x)), \tag{3.25}$$

which is known as the Infomax principle. According to previous research [51], [52], maximum likelihood estimation is equivalent to the principle of network entropy maximization. For the equivalence to hold, it is necessary to ensure that the non-linearities ϕ_i used in the neural network are chosen as the cumulative distribution functions corresponding to the dendrites f_i.

In this research work the algorithm used to implement ICA is Extended Infomax. Extended Infomax separates mixtures of super gaussian and sub gaussian sources using a learning rule. As derived above, the goal of ICA is to find a linear mapping $\mathbf{W}$ such that the unmixing signals

$$\mathbf{u}(t) = \mathbf{W}\mathbf{x}(t) = \mathbf{W}\mathbf{A}\mathbf{s}(t)$$

are statistically independent. The learning algorithm can be derived using the maximum likelihood formulation. The pdf of the observations x can be expressed as follows:

$$p(\mathbf{x}) = |det(\mathbf{W})|p(u), \tag{3.26}$$

where

$$p(u) = \Pi_{i=1}^{N} p_i(u_i),$$

is the hypothesized distribution of $p(\mathbf{s})$. The log-likelihood of the equation (3.26) is:

$$L(\mathbf{u}, \mathbf{W}) = \log|det(\mathbf{E})| + \sum_{i=1}^{N} \log p_i(u_i) \tag{3.27}$$

Maximizing the log-likelihood with respect to $\mathbf{W}$ derives a learning algorithm for $\mathbf{W}$:

$$\Delta W \propto [(\mathbf{W}^T)^{-1} - \phi(\mathbf{u})\mathbf{x}^T] \tag{3.28}$$

where

$$\phi(u) = -\frac{\frac{\partial p(\mathbf{u})}{\partial \mathbf{u}}}{p(\mathbf{u})} = [-\frac{\frac{\partial p(u_1)}{\partial u_1}}{p(\mathbf{u}_1)}, ..., -\frac{\frac{\partial p(u_N)}{\partial u_N}}{p(\mathbf{u}_N)}]^T$$

According to Amari(1998) [53], maximization of the log-likelihood can be achieved by following the natural gradient:

$$\Delta W \propto \frac{\partial L(\mathbf{u}, \mathbf{W})}{\partial \mathbf{W}} \mathbf{W}^T \mathbf{W} = [\mathbf{I} - \phi(\mathbf{u})\mathbf{u}^T]\mathbf{W} \tag{3.29}$$

Here, $W^T W$ re-scales the gradient, simplifies the learning rule in equation (3.28) and speeds convergence markedly. If $\phi(\mathbf{u})$ is a logistic function so that:

$$\phi(\mathbf{u}) = 2\tanh(\mathbf{u}) \tag{3.30}$$

the learning rule can be reduced to the initial Infomax algorithm introduced by Bell and Sejnowski (1995) [49] with the natural gradient:

$$\Delta W \propto [\mathbf{I} - 2\tanh(\mathbf{u})\mathbf{u}^T]\mathbf{W} \tag{3.31}$$

In order for the Extended Infomax Algorithm to separate sources with a variety of distributions, the following learning rules were introduced. The learning rules for subgaussian and supergaussian sources, correspondingly:

$$\Delta W \propto \begin{cases} [\mathbf{I} - \tanh(\mathbf{u})\mathbf{u}^T - \mathbf{u}\mathbf{u}^T]\mathbf{W} & : supergaussian \\ [\mathbf{I} + \tanh(\mathbf{u})\mathbf{u}^T - \mathbf{u}\mathbf{u}^T]\mathbf{W} & : subgaussian \end{cases}$$

The difference between the learning rules of supergaussian and subgaussian is the sign before the tanh function which can be determined using a switching criterion.

3.1.3 High Order Statistics

The term **High Order Statistics (HOS)** denote functions that use the third or higher moments. The HOS used at this research work are the third

standardized moment or skewness, the forth standardized moment or kurtosis and Rényi entropy to assist artifact detection. HOS especially estimate shape parameters, such as measuring the deviation of a distribution from the normal distribution. Consequently, the used HOS are briefly defined.

Kurtosis

According to the previous, kurtosis is the scaled version of the fourth moment of the distribution so it is related to the tails of the distribution. Higher kurtosis corresponds to outliers or greater deviations and it is defined as follows:

$$kurtosis = E\{y^4\} - 3(E\{y^2\})^2,$$

where y is a random variable. Usually is assumed that y has a unit variance, so the equation above is transformed into $E\{y^4\} - 3$. It is known that for a gaussian y, the fourth moment $E\{y^4\}$ equals $3(E\{y^2\})^2$. Consequently, kurtosis is zero for a gaussian random variable (mesokurtic). If $kurtosis > 3$ (positive kurtosis), the random variable y is called super-gaussian or leptokurtic. On the other hand, if $kurtosis < 3$ (negative kurtosis) then random variable y is called subgaussian or platykurtic. The different types of kurtosis are depicted on the Fig. 3.3[2].

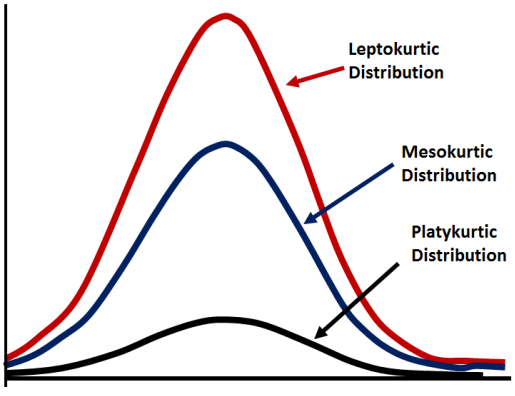

Figure 3.3: Different types of kurtosis.

[2] https://www.datavedas.com/measures-of-shape/

Skewness

Skewness measures the lack of symmetry or, in other words, characterizes the degree of asymmetry of a distribution. Skewness of a distribution is defined to be:

$$skewness = \frac{\mu_3}{\mu_2^{\frac{3}{2}}},$$

where $\mu_n = E\{(y - E\{y\})^n\}$ is the n_{th} central moment of the random variable y. A positive degree of skewness corresponds to a positively skewed distribution (distribution's right tail is longer). On the other hand, a negative degree of skewness corresponds to a negatively skewed distribution (negative skew) as shown in Fig. 3.4 [3].

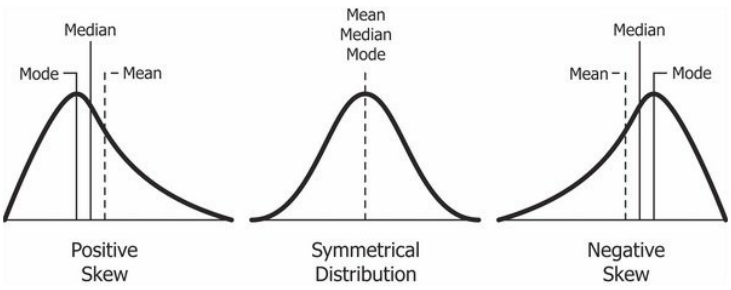

Figure 3.4: Different types of skewness.

Rényi entropy

Rényi entropy generalizes Shannon entropy and it is a measurement of uncertainty or randomness of a system. Rényi entropy is defined as:

$$H_\alpha(p_1, p_2, ..., p_n) = \frac{1}{1-\alpha} \ln \sum_{i=1}^{n} p_i^a,$$

where $\alpha > 0, \alpha \neq 1$. As $\alpha \to 1, H_\alpha(p_1, p_2, ..., p_n)$ converges to $H(p_1, p_2, ..., p_n)$, which is Shannon's measure of entropy.

[3] https://codeburst.io/2-important-statistics-terms-you-need-to-know-in\-data-science-skewness-and-kurtosis-388fef94eeaa

3.1.4 Correlation Coefficient

In this research work, the degree of data's correlation is measured using Pearson's correlation coefficient. More specific, Pearson's correlation coefficient is a statistical measurement of linear correlation and direction between two random variables X and Y. The values of correlation range between -1 and $+1$, where $+1$ denotes perfect positive correlation, -1 denotes perfect negative correlation and 0 denotes no linear correlation.

$$\rho_{X,Y} = \frac{cov(X,Y)}{\sigma_X \sigma_Y},$$

where σ_X and σ_Y stand for the standard deviation of X and Y, respectively.

3.1.5 Empirical Mode Decomposition

Empirical Mode Decomposition (EMD) [54] is an adaptive representation of non-stationary and non-linear signals. The fundamental deference between EMD and other decomposition methods such as Fourier Transform and Wavelet Decomposition, it is that the first one is purely data driven. In other words, on EMD data's decomposition is adaptively derived from the data [55]. Moreover, EMD is applicable on non-stationary and non-linear signals because it is based on the local characteristic time scale of the data. Large-scale brain responses satisfy both non-stationarity and non-linearity.

EMD decomposes a signal into basic functions called Intrinsic Mode Functions (IMFs) which have instantaneous frequency. The IMFs are computed by the iterative Algorithm 1.

According to Lindsen et. al (2010) [55] the procedure described on Algorithm 1 [4]is repeated until the resulting signal satisfies the three following criteria: *(1) the number of extremes and the number of zero crossings must either be equal or differ at most by one, (2) the mean value of the envelope defined by the local maxima and the envelope defined by the local minima must be zero at any time point, and (3) the difference between two consecutive repetitions, in terms of standard deviation, must not be smaller than some*

Algorithm 1 EMD Algorithm

Require: Given a signal $x(t)$
1) Set $r(t) := x(t)$ and $k = 0$
while $r(t)$ is not monotonous **do**
2) Set $m(t) = r(t)$
while $m(t)$ is nontrivial **do**
3) Interpolate between minima (resp. maxima), ending up withsome 'envelope' $e_{min}(t)$ (resp. $e_{max}(t)$)
4) Compute the average $m(t) = (e_{min}(t) + e_{max}(t))/2$
5) Extract the detail $c(t) = r(t) - m(t)$, and denote $c(t)$ as $r(t)$
end while
6) Set $k = k + 1$
7) Set $imf_k(t) = c(t)$
8) Set $r(t) = x(t) - \sum_{i=1}^{k} imf_i(t)$
end while
Output: $x(t) = \sum_{i}^{k} imf_i(t)$

predetermined criterion. Each resulting signal corresponds to an IMF and it is subtracted from the original data. The algorithm converges when the residue becomes a monotonic function or when it becomes negligibly small. The linear sum of the IMFs constitute the original signal.

3.1.6 Wavelet Decomposition

The Wavelet Transform (WT) is a Time-Frequency Representation and a Multi-Resolution Analysis (MRA) [1]. Wavelet Transform overcomes limitations introduced by classical Fourier techniques by providing optimal time-frequency localization for non-stationary signals, such as EEG and MEG time courses. As depicted in Fig. 3.5 [5], it produces good frequency localization at low frequencies (long time windows) and good time localization at high frequencies (short time windows), which is an advantage compared to short-time Fourier Transform (STFT). Also, reveals features related to the transient nature of the signal, that are not obvious by the Fourier Transform

[4] https://www.sciencedirect.com/science/article/abs/pii/S0957417418304901

techniques.

In practise, Discrete Wavelet Transform (DWT) is used usually instead of Wavelet Transform. The discrete counterpart [56] of Wavelet Transform is implemented by bandpass filter banks. Each filer has frequency band and central frequency half of the previous one. Given a signal $S(t)$, a convolution of S with a lowpass and a highpass filter extracts an approximation signal $A(t)$ and a detail signal $D(t)$, accordingly. The generalization of Wavelet Decomposition technique is depicted in Fig. 3.6 [6]. In the standard tree of decomposition only the approximation signal is convoluted with the filters of the second stage, and so again until the last level of the decomposition. An example wavelet decomposition of signal S analyzed at level 3 is depicted in Fig. 3.7 [6]. The Wavelet Series Expansion [1], [2] of a signal $x(t) \in L^2(\Re)$ is the following:

$$x(t) = \sum_k c_{j_0 k}\phi_{j_0 k}(t) + \sum_{j=j_0}^{\infty}\sum_k d_{jk}\psi_{jk}(t), \tag{3.32}$$

where the scaling function ϕ is creates approximations of the signal, by a differing factor of 2.

$$d_{jk} = \int x(t)\psi^*(t)dt \tag{3.33}$$

stands for the detail or wavelet coefficients and

$$\psi_{jk}(t) = \frac{1}{\sqrt{2^j}}\psi\left(\frac{t - k2^j}{2^j}\right) \tag{3.34}$$

are the wavelet functions, which encode the difference between the approximations. The approximation or scaling coefficients are:

$$c_{jk} = \int x(t)\phi^*_{jk}(t)dt, \tag{3.35}$$

[5] https://neuroimage.usc.edu/brainstorm/Tutorials/TimeFrequency#Hilbert_transform

[6] https://www.mathworks.com/help/wavelet/ref/wavedec.html

where

$$\phi_{jk}(t) = \frac{1}{\sqrt{2^j}}\phi\left(\frac{t - k2^j}{2^j}\right) \tag{3.36}$$

are the scaling functions. The details and the approximations are defined as follows:

$$D_j(t) = \sum_{k=-\infty}^{+\infty} d_{jk}\psi_{jk}(t) \tag{3.37}$$

$$A_j(t) = \sum_{k=-\infty}^{+\infty} c_{jk}\phi_{jk}(t) \tag{3.38}$$

The original signal can be reconstructed by the details and the approximations as described in equation 3.39, for fixed N:

$$S(t) = A_N(t) + D_1(t) + D_2(t) + ... + D_N(t) \tag{3.39}$$

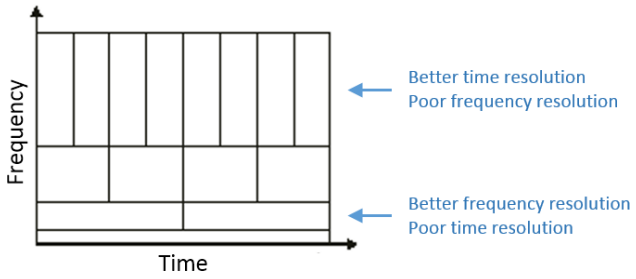

Figure 3.5: Trade-off between temporal and spectral resolution.

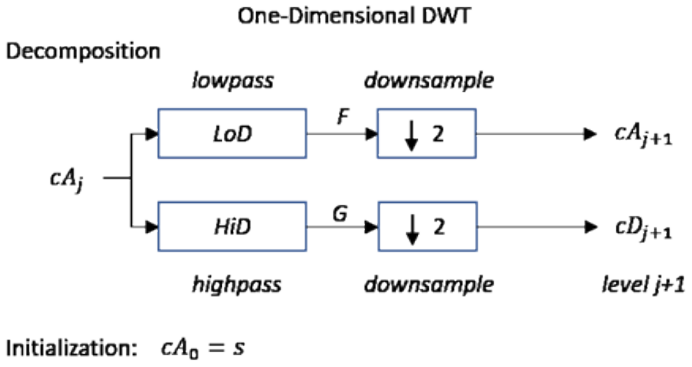

Figure 3.6: Generalization of Wavelet Decomposition.

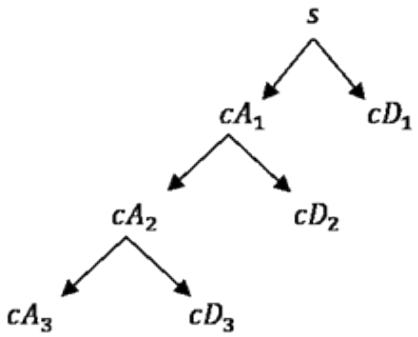

Figure 3.7: Tree of wavelet decomposition at level 3.

3.1.7 Signal Space Projection

Signal Space Projection (SSP) is another method for artifact correction. The sources of cerebral activity generate electric potential (or magnetic field) distributions with spatial distributions different from these generated by non-cerebral sources [57], [58]. SSP is based on the assumption that non-cerebral activity spans a low dimension linear space which is independent from the space spanned by the cerebral activity.

It is acceptable to decompose any $n - channel$ measurements $\mathbf{b}(t)$ into its signal and noise components respectively:

$$\mathbf{b}(t) = \mathbf{b}_s(t) + \mathbf{b}_n(t) \tag{3.40}$$

An integral part of the algorithm is the sufficient definition of noisy data $\mathbf{b}(t)$ using field patterns $\mathbf{b}_1 ... \mathbf{b}_m$:

$$\mathbf{b}_n(t) = \mathbf{U}\mathbf{c}_n(t) + \mathbf{e}(t), \tag{3.41}$$

where the columns of $\mathbf{U}$ form an orthonormal basis for $\mathbf{b}_1 ... \mathbf{b}_m$, $\mathbf{c}_n(t)$ is an $m - component$ column vector and $\mathbf{e}(t)$ introduces a small error with no consistent spatial distributions over time: $\mathbf{C}_e = E\{\mathbf{e}\mathbf{e}^T = \mathbf{I}\}$. The column space of $\mathbf{U}$ spans the noise subspace. The orthogonal complement operator

is calculated using the noise subspace and is defined as follow:

$$\mathbf{P}_{\perp} = \mathbf{I} - \mathbf{U}\mathbf{U}^{T} \tag{3.42}$$

The projection operator $\mathbf{P}_{\perp}$ is called the signal-space projection operator and is applied on the initial measurements yielding

$$\mathbf{b}(t) \approx \mathbf{P}_{\perp}\mathbf{b}_{s}(t), \tag{3.43}$$

given that $\mathbf{P}_{\perp}\mathbf{b}_{n}(t) = \mathbf{P}_{\perp}\mathbf{U}\mathbf{c}_{n}(t) \approx 0$. Generally, the signal-space projection suppress noise by a factor of 10 or more. The effectiveness of SSP depends on two factors:

1. The noise distributions should be well-defined by the basis set $\mathbf{b}_1 ... \mathbf{b}_m$.
2. The angles between the noise subspace spanned by $\mathbf{b}_1 ... \mathbf{b}_m$ and the signal vectors $\mathbf{b}_s(t)$ should be as close to $\frac{\pi}{2}$ as possible [7].

If the noise subspace is not well-defined, some noise will remain on the measurements: $\mathbf{P}_{\perp}\mathbf{b}_{n}(t) \neq 0$. If any of the brain signal vectors $\mathbf{b}_s(t)$ is close to the noise subspace the signal will be attenuated by the application of $\mathbf{P}_{\perp}$, too.

3.2 Semi-automated Detection of HFOs

High Frequency Oscillations (HFOs) visual marking is an extremely laborious and time-consuming process. Consequently, the HFOs detection based on automatic or semi-automatic algorithms has been extensively researched [7]. A variety of algorithms has been developed, some of them depend only on thresholding techniques in time domain, while others integrate an extra stage of identification in frequency domain [7], [59], [60], [9], [61], [62], [63], [64], [65], [66]. The algorithm implemented in the hereunto research work consists of three consecutive stages. The first stage of analysis is focused on time domain thresholding technique and aims on the detection of Events of Interest (EoIs),

[7] https://neuroimage.usc.edu/brainstorm/Tutorials/ArtifactsSsp

comprising of at least four cycles (oscillations) [7], [12]. The following second stage incorporate Time Frequency Representation (TFR) in order to visually distinguish the HFOs from the set of EoIs. In TFR, HFOs can be spotted as short-lived events with the characteristic morphology of an isolated blob in contrast with other transient events which form an elongated blob, extended in frequency [7], [12]. The third stage is the energy-based clustering of the detected HFOs.

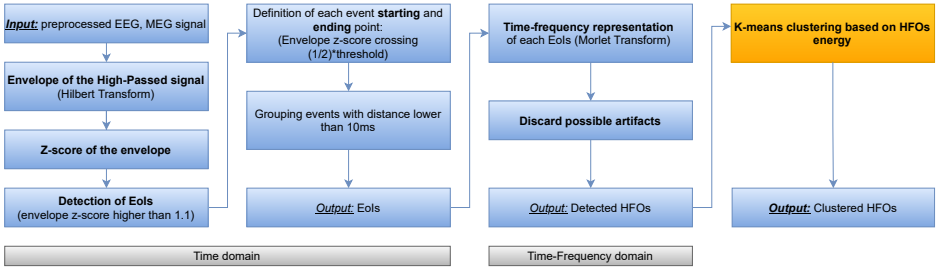

Figure 3.8: Schematic diagram of the algorithm steps.

Stage 1: Detection of EoIs

Firstly, the signal was band-passed filtered between 80 and 500Hz. It is highly recommended to use Finite Impulse Response (FIR) filter to restrict ringing effect and the "Gibbs" phenomenon. Then the signal is examined for EoIs with relative high amplitude and sufficient duration. The steps of the algorithm are:

1. Calculate the envelope of the band-pass signal using Hilbert Transform

2. Calculate the mean and standard deviation (SD) of the envelope over 10s sliding windows centered on each point of the signal. Estimate the overall mean and SD using the median values over all windows. This technique yields values of mean and SD which are more robust to segments of signals with a lot of HFOs and high SD [12].

3. Calculate the z-score of the envelope, using the previously calculated mean and SD values. Set a threshold equal to 1.1. Each event that exceeds the threshold is marked as EoIs.

4. Classify events as EoIs with duration of at least $37ms$. Merge EoIs with an inter-interval of less than $10ms$ into one EoI.
   NOTE: the maximum z-score threshold depends on the amplitude of artifacts that may exist in the recordings and its value should be calibrated with respect to the data [12].

Stage 2: Distinguish HFOs among EoIs

The second stage aims on recognising real HFOs among the EoIs. This step is necessary in order to reject possible artifacts (spurious EEG activity or filtering effects) that have been classified as EoIs on the first stage of the algorithm. According to literature, HFOs on time-frequency domain appear as short-lived events with an isolated spectral peak at a distinct frequency above $80Hz$. Hence, all the EoIs are divided into trials with duration from $-0.5ms$ to $0.5ms$, where the peak of the EoIs is mapped to $0ms$ and then transformed into time-frequency domain. For this transformation Morlet Wavelet Transform is used in the frequency range from $80Hz$ to $500Hz$ (central frequency = 1Hz, Full-Width-At-Half-Maximum = 3 s) [12].

Stage 3: Clustering of detected HFOs

After the detection has been completed, HFOs are clustered based on their energy. Energy has been calculated on consecutive segments of the signals with overlap 20%. The output of the *K-means* is the clustered HFOs.

3.2.1 Hilbert Transform

Since Hilbert Transform (HT) is used for the envelope calculation on the *HFOs Detection Algorithm*, it is simply illustrated in this section. HT is a part of Hilbert Huang transform [67] and for a given signal $x(t)$ is defined as:

$$\hat{x}(t) = H[x(t)] = \frac{\int_{\infty}^{-\infty} \frac{x(t)}{t-\tau} d\tau}{\pi} = x(t) * \frac{1}{\pi t} \tag{3.44}$$

The analytic signal can be defined as:

$$z(t) = x(t) + j\hat{x}(t) = \alpha(t)e^{j\theta(t)}, \tag{3.45}$$

where $j = \sqrt{-1}$ and $\alpha(t) = \sqrt{x^2 + \hat{x}^2}$ and $\theta(t) = \arctan\left(\frac{\hat{x}}{x}\right)$. Here, $\alpha(t)$ stands for the instantaneous amplitude and $\theta(t)$ for the instantaneous phase. From equation 3.45 derives that the analytic signal consists of a real part $x(t)$, which is the original data, and an imaginary part $\hat{x}(t)$ which contains the HT. The imaginary part is the original time series after a $\frac{\pi}{2}$ rotation. The instantaneous frequency is given by $\omega = \frac{d\theta}{dt}$. The Hilbert envelope spectrum is defined as:

$$h(f) = \int_{-\infty}^{\infty} \sqrt{x^2 + \hat{x}^2} e^{(-j2\pi ft)dt} \tag{3.46}$$

3.2.2 K-means clustering

K-means clustering is an iterative algorithm that partitions data and assigns n observations to exactly one of the k clusters which are defined by the centroids (mean or cluster center) [68]. The number of clusters k is one of the algorithm's inputs. The algorithm's steps are the following:

1. Choose k initial cluster centers, which are the centroids. The cluster center initialization can be implemented by choosing k random observations or using the K-means ++ algorithm [69].

2. Calculate the distances of points to the closest cluster centroid.

3. The assignment of the observations can be implemented by two different ways:

   - Each observation is assigned to the cluster with the closest centroid.
   - Individually assign observations to a different centroid if the reassignment decreases the sum of the within-cluster, sum-of-squares point-to-cluster-centroid distances[8].

[8] https://www.mathworks.com/help/stats/kmeans.html

4. For each cluster calculate the average of the observations in order to obtain k new centroid locations.

5. Repeat steps $2-4$ until no-changes on cluster assignments are detected or the algorithm has reached the maximum number of iterations.

3.3 Source Analysis

Source Analysis is the scientific field which studies modeling and estimating techniques of the neuronal currents throughout the brain that generate the electric potentials and magnetic fields measured by invasive or non-invasive data acquisition systems. The aim of Source Analysis techniques is to find the brain areas responsible for the generation of a particular type of activity. Especially in epilepsy, Source Analysis techniques are used in order to localize more accurately the epileptogenic zone, alongside with MRI, and facilitate the epilepsy surgery. Source Analysis consists of solving the so-called forward and inverse problem. Briefly, the Forward Problem models the potentials at the electrodes from a given electrical source in the brain. On the other hand, the Inverse Problem estimates the brain sources when knowing the potentials at the EEG electrodes. The forward modeling of head tissues and sensor characteristics are necessary to solve the Inverse Problem, so the latter is completed second.

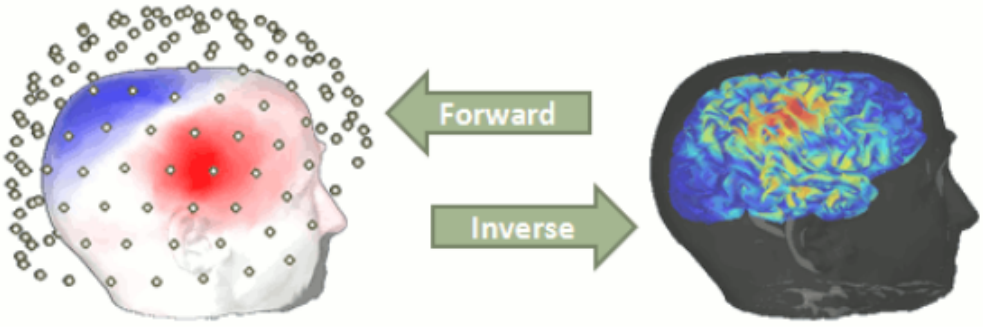

Figure 3.9: Forward and Inverse problems. Adapted from Brainstorm toolbox.

3.3.1 Forward Problem

Mathematical Formulation

The forward problem estimates the channels measurements by assuming all possible sources (dipoles), using a head model which is a simulation of the electromagnetic properties of the head. The sources span the source space (or source model) which express all candidate positions of the sources. Given the aforementioned definition of dipoles, sources are defined by their position and moment (amplitude and orientation), too. Their position is expressed in the Cartesian coordinate system, so only the amplitude is unknown hence the orientation is given by $\{\mathbf{e}_x, \mathbf{e}_y, \mathbf{e}_z\}$.

For N sensors and p dipoles:

$$\mathbf{m} = \begin{bmatrix} m(\mathbf{r}_1) \\ \vdots \\ m(\mathbf{r}_N) \end{bmatrix} = \begin{bmatrix} \mathbf{l}(\mathbf{r}_1, \mathbf{r}_{Q_1}) & \dots & \mathbf{l}(\mathbf{r}_1, \mathbf{r}_{Q_p}) \\ \vdots & \ddots & \vdots \\ \mathbf{l}(\mathbf{r}_N, \mathbf{r}_{Q_1}) & \dots & \mathbf{l}(\mathbf{r}_N, \mathbf{r}_{Q_p}) \end{bmatrix} \begin{bmatrix} \mathbf{s}_1\mathbf{e}_1 \\ \vdots \\ \mathbf{s}_p\mathbf{e}_p \end{bmatrix} \tag{3.47}$$

where $i = 1, ..., p$, the column indices, $j = 1, ..., N$, the row indices and s substitutes dipole's magnitude d_i (assume that the source is determined by one amplitude and orientation).

For N sensors, p dipoles (or sources) and n discrete time points:

$$\mathbf{M} = \begin{bmatrix} m(\mathbf{r}_1, 1) & \dots & m(\mathbf{r}_1, n) \\ \vdots & \ddots & \vdots \\ m(\mathbf{r}_N, 1) & \dots & m(\mathbf{r}_N, n) \end{bmatrix} = \mathbf{L}(\{\mathbf{r}_j, \mathbf{r}_{dip_i}\}) \begin{bmatrix} s_{1,1}\mathbf{e}_1 & \dots & s_{1,n}\mathbf{e}_1 \\ \vdots & \ddots & \vdots \\ s_{p,1}\mathbf{e}_p & \dots & s_{p,n}\mathbf{e}_1\mathbf{e}_p \end{bmatrix}$$

$$= \mathbf{L}(\{\mathbf{r}_j, \mathbf{r}_{dip_i}\})\mathbf{S} \tag{3.48}$$

where $\mathbf{M} \in \mathbb{R}^{Nxn}$ is the matrix of data measurements at different time points, $\mathbf{L}$ is the leadfield and $\mathbf{S}$ is the matrix of dipole magnitudes at various time instants. Each row of the leadfield $\mathbf{L} \in \mathbb{R}^{Nxp}$ is, also called leadfield and de-

scribes the current flow for a given sensor through each dipole position [70]. It is usually assumed that the apical dendrites that produce the measurements are oriented normally to the cortex, so dipoles are usually constrained to have such an orientation [70]. As a result, only the magnitude of the dipoles are unknown:

$$\begin{aligned}\mathbf{M} &= \begin{bmatrix} \mathbf{l}(\mathbf{r}_1, \mathbf{r}_{dip_1})\mathbf{e}_1 & \dots & \mathbf{l}(\mathbf{r}_1, \mathbf{r}_{dip_p})\mathbf{e}_p \\ \vdots & \ddots & \vdots \\ \mathbf{l}(\mathbf{r}_N, \mathbf{r}_{dip_1})\mathbf{e}_1 & \dots & \mathbf{l}(\mathbf{r}_N, \mathbf{r}_{dip_p})\mathbf{e}_p \end{bmatrix} \begin{bmatrix} \mathbf{s}_1 \\ \vdots \\ \mathbf{s}_p \end{bmatrix} \\ &= \mathbf{L}(\{\mathbf{r}_j, \mathbf{r}_{dip_i}\}, \mathbf{e}_i) \begin{bmatrix} s_{1,1} & \dots & s_{1,n} \\ \vdots & \ddots & \vdots \\ s_{p,1} & \dots & s_{p,n} \end{bmatrix} \qquad (3.49) \\ &= \mathbf{L}(\{\mathbf{r}_j, \mathbf{r}_{dip_i}, \mathbf{e}_i\})\mathbf{S} \qquad (3.50)\end{aligned}$$

All things considered, the data matrix $\mathbf{M}$ can be written as:

$$\mathbf{M} = \mathbf{LS} + \mathbf{n} \qquad (3.51)$$

where $\mathbf{n}$ stands for noise added to system. Generally, the noise is modelled as zero mean Gaussian random variable: $\mathbf{n} \sim N(0, \sigma^2\mathbf{I}_N)$, where σ^2 is the standard deviation of the noise and I_N is the identity matrix.

The electromagnetic field is the combination of the electric field $\mathbf{E}$ (V/m_2) and the magnetic field $\mathbf{B}$ (T) and it can be computed by *Maxwell's equations* and the *Continuity equation*.

Maxwell's equations

$$\nabla \mathbf{E} = \rho/\epsilon \tag{3.52}$$

$$\nabla \times \mathbf{E} = -\partial \mathbf{B}/\partial t \tag{3.53}$$

$$\nabla \mathbf{B} = 0 \tag{3.54}$$

$$\nabla \times \mathbf{B} = \mu(\mathbf{J} + \epsilon \partial \mathbf{E}/\partial t), \tag{3.55}$$

where μ stands for magnetic permeability in H/m and ϵ stands for the electrical permitivity of the material.

Continuity equation:

$$\nabla \mathbf{J} = -\frac{\partial \rho}{\partial t}, \tag{3.56}$$

where the total current density $\mathbf{J}$ is measured in A/m^2 and ρ stands for the charge density C/m^3.
Maxwell's equations can be simplified considering:

- the magnetic permeability of head tissue is equal to that of free space: $\mu = \mu_0$
- $\partial \mathbf{E}/\partial t$ and $\partial \mathbf{B}/\partial t$ can be neglected while computing $\mathbf{E}$ and $\mathbf{B}$

In order to take quasistatic approximations under consideration, the time-derivative terms have to be small compared to the ohmic current: $\left|\epsilon \frac{\partial \mathbf{E}}{\partial t}\right| \ll \left|\sigma \mathbf{E}\right|$, for example $\frac{2\pi f \epsilon}{\sigma} \ll 1$. The current density $\mathbf{J}^p$ consists of the primary current and the volume or return current $\mathbf{J}^u = \sigma \mathbf{E}$, which is passive and σ stands for microscopic conductivity. Primary current is produced by neural activity and it flows mainly inside or in the vicinity of a cell, while the volume current flows passively everywhere in the medium [31]. Mathematically speaking:

$$\mathbf{J} = \mathbf{J}^p + \sigma \mathbf{E} \tag{3.57}$$

Given that the expected frequency range of neural sources is less than $1kHz$, magnetic fields and electric currents behave as stationary at all time

instances. Consequently, the quasi-static approximation of Maxwell's equations can be used. By differentiating equation 3.57 and taking into account that $\nabla \mathbf{J} = 0$ in the quasistatic approximation:

$$\nabla \mathbf{J} = \nabla \mathbf{J}^p + \sigma \nabla \mathbf{E} \Rightarrow \nabla \mathbf{J}^p = -\sigma \nabla \mathbf{E} \tag{3.58}$$

Given that $\nabla \times \mathbf{E} = 0$ (quasistatic approximations), $\mathbf{E} = -\nabla V$ (V stands for a potential) the equation 3.58 can be written as follows:

$$\nabla \mathbf{J}^p = -\nabla(\sigma(\nabla V)) \tag{3.59}$$

The aim is to estimate V using analytical or numerical techniques. After calculating V, the computation of $\mathbf{B}$ is direct. The whole forward problem is summarized in the computation of the magnetic field $\mathbf{B}$ outside the head from a given primary current distribution $\mathbf{J}^p$ within the brain [31]. Taking into account that brain sources are represented as mathematical point dipoles:

$$\mathbf{J}^p = \mathbf{m}_0 \delta(x - x_0), \tag{3.60}$$

where $\mathbf{m}_0$ is the dipole moment, δ stands for the Dirac function and x_0 is the dipole position. Given that the magnetic potential A can be written as:

$$\mathbf{A}(x) = \frac{\mu}{4\pi} \int_\Omega \frac{\mathbf{J}^p(x') - \sigma(x')\nabla V(x')}{|x - x'|} dx' \tag{3.61}$$

The magnetic flux Ψ measured within a surface area S and circumference l can be written as:

$$\Psi = \int_S \mathbf{B} dS = \oint_l A(x) dx \tag{3.62}$$

$$\Psi = \frac{\mu}{4\pi} \left[\oint_l \int_\Omega \frac{\mathbf{J}^p(y)}{|x - y|} dy dx + \oint_l \int_\Omega \frac{-\sigma(y)\nabla V(y)}{|x - y|} dy dx \right] \tag{3.63}$$

where the first term is the primary magnetic flux and the second term is the secondary magnetic flux.

3.3.2 Conductivity

According to Ohm's law, the current density **J** is given by the electric field **E** as follows:

$$\mathbf{J} = \sigma \mathbf{E} \tag{3.64}$$

where $\sigma \in \mathbb{R}^{3x3}$ stands for the conductivity tensor in each position r:

$$\sigma = \begin{bmatrix} \sigma_{11} & \sigma_{12} & \sigma_{13} \\ \sigma_{21} & \sigma_{22} & \sigma_{23} \\ \sigma_{31} & \sigma_{32} & \sigma_{33} \end{bmatrix} \tag{3.65}$$

with units $A/(Vm) = S/m$.

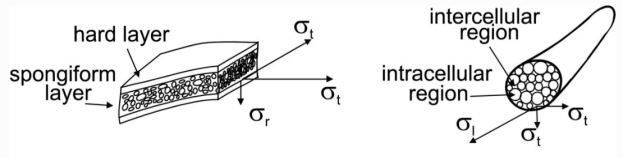

(a) On the left: the three layers of the skull (hard-spongiform-hard). Radial conductivity (σ_r) is 10 times smaller than the tangential conductivity (σ_t). On the right: white matter consists of different nerve fibers (axons grouped in bundles). The conductivity along the nerve bundle is 9 times larger than perpendicular to the nerve bundle. Adapted from Hallez et al., 2007.

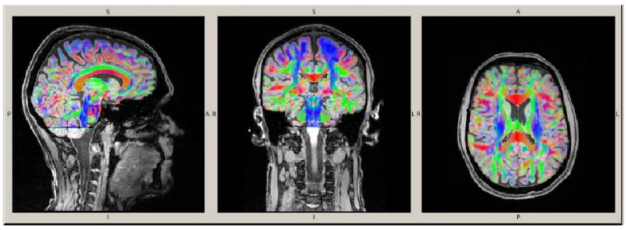

(b) The different colors indicate the primary fiber orientation (red: left-right, green: anterior-posterior and blue superior-inferior). Adapted from http://www.sci.utah.edu/~wolters/PaperWolters/2017/AntonakakisTalkBACI2017.pdf

Human head compartments are classified into two categories regarding

their conductivity: isotropic and anisotropic [71]. Isotropic conductivity denotes that the current flow is the same in every direction (conductivity is equal in all directions [72]). Grey matter, scalp and cerebro-spinal fluid (CSF) are characterized by isotropic conductivity and the position dependent conductivity tensor, σ, is reduced to a position dependent conductivity scalar. Anisotropic conductivity denotes conductivity inequality across the different directions since the electric field can induce a current density component perpendicular to it with the appropriate σ in equation 3.64 [72]. Skull and white matter are compartments of anisotropic conductivity; skull consists of two hard layers with relative low conductivity and a spongiform layer between them with higher conductivity. White matter consists of different nerve fibers with higher conductivity in the direction along them. According to Wolters et al. anisotropic conducting tissues jeopardize the forward problem calculation and consequently the inverse problem [73], [74].

3.3.3 Boundary Conditions

There are two boundary conditions that govern the interface between two compartments. The first boundary condition is based on the compartment's transparency. A ll the current that flows out from one compartment enters the neighboring compartment. This condition does not hold if one of the compartments is the air because of its very low conductivity [72]. For non-air compartments the Neumann boundary condition is defined as follows:

$$\mathbf{J}_1\mathbf{e}_n = \mathbf{J}_2\mathbf{e}_n \tag{3.66}$$

$$(\sigma_1\nabla V_1)\mathbf{e}_n = (\sigma_2\nabla V_2)\mathbf{e}_n \tag{3.67}$$

For air compartment the homogeneous Neumann boundary condition holds:

$$\mathbf{J}_1\mathbf{e}_n = 0 \tag{3.68}$$

$$(\sigma_1\nabla V_1)\mathbf{e}_n = 0 \tag{3.69}$$

For non-air compartments only, the potential between the compartments is continuous (Dirichlet boundary condition):

$$V_1 = V_2 \tag{3.70}$$

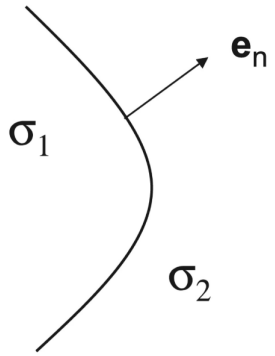

Figure 3.11: Boundary between two compartments with conductivities σ_1 and σ_2. $\mathbf{e}_n$ stands for the normal vector to the interface. Adapted from Hallez et al., 2007.

3.3.4 Head Volume Conductor Models

Head models can be classified into two major categories: simple and realistic head models. The former incorporates analytical homogeneous single spheres or multi-spheres while the latter use numerical solutions, such as Boundary Element Method and Finite Element Method (FEM), to approximate head geometry. MRI scan can be involved on both categories in order to assist head modeling for more accurate results [75].

Spherical Head Model

Spherical head models are the simplest and most popular models of head geometry in MEG/EEG. They consist of concentric spherical layers, where each spherical layer represents a different head tissue: scalp, skull, cerebrospinal fluid (CSF) and brain. Especially for MEG spherical head models, some unique properties are held. To explain, spherical MEG head models remain unaffected by the number of shells and their respective conductivity. That is

why a source inside concentric spherical layers with different conductivities generates the same MEG fields as if it was located inside a single homogeneous sphere, because only the distribution of secondary volume currents affect conductivity. Just to mention that secondary volume currents are suppressed by the original primary neural currents. According to the analytic formulation of Maxwell's equations in the spherical geometry, secondary currents do not generate any magnetic field outside the volume conductor [75]. As a result, measured MEG fields are not affected by the conductivity and the radius of each spherical layer [75], which is one of MEG's major advantages.

It is important to mention that MRI-scan can be used in spherical head modeling to optimize sphere's fitting to the participant's head. Moreover, outside the spherical volume conductor there are not any magnetic fields generated by radially oriented brain currents. This is the reason why currents generated at gyral crests or sulcal depths produce attenuated MEG signals in contrast with those signals generated by currents flowing perpendicularly to the sulcal walls [75]. Finally, another difference between MEG and EEG is the sensitivity to source orientation. MEG is considered less sensitive given that the magnitude of magnetic fields attenuates faster than the magnitude of the electrical potential. Although it is believed that MEG can detect mesial and subcortical brain structures, some studies prove the opposite [75], [76].

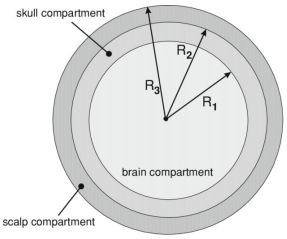

Figure 3.12: 3-concentric sphere head model. Adapted from G. Crevecoeur et al. 2008.

Realistic Head Model

Even though spherical models are simple to be applied and not computationally demanding, they lead to poor source estimations due to rough approximations of the human's head. A number of realistic head models has been

proposed in order to face the aforementioned disadvantages. Realistic head models solve Maxwell's equations with numerical methods. The two major numerical approaches are the: Boundary Element Method (BEM) and Finite Element Method (FEM). In these approaches MRI scan of the subject's head is necessary in order to extract the geometric tessellations of the various envelopes forming the head tissues [75].

Boundary Element Method: is a numerical technique based on homogeneous and isotropic head compartments. This method calculates the potential values. In this method MRI yields triangulated segmented envelopes. Therefore, BEM uses triangles (boundary elements) as building blocks. Surface boundaries are defined upon each triangle. The tissue envelope is produced after calculating the potential difference at each triangle between the two compartments with different conductivities. The potential difference is induced of a current source inside the brain, such as a dipole. Interfaces are defined by separating volume regions with different conductivities while the boundary is the outer surface of the compartment and distinguishes the non-conducting air from the conducting volume [72]. For instance, a typical head model comprises of 3 surfaces: brain-skull interface, skull-scalp interface and outer surface.

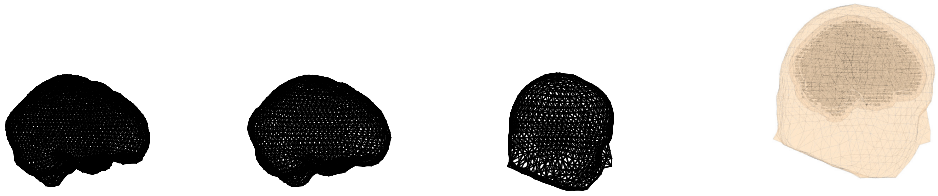

(a) Brain compartment. (b) Skull compartment. (c) Scalp compartment. (d) Altogether the compartments.

Figure 3.13: BEM head model consisting of three compartments, generated using FieldTrip Toolbox.

Finite Element Method: is also a numerical technique which uses as a building block, elementary volumes such as tetrahedron or hexahedrons [73], [72], [77], [15]. The potential difference is calculated on the vertices of the building blocks. FEM, also, allows anisotropic tissue conductivity, such as the

three-layered skull bone (compacta-spongiosa-compacta), CSF and the white matter. The modelled compartments are: the scalp, the skull compacta, the skull spongiosa, the CSF and the gray and white matter. Finally, FEM's calculation is a laborious and complex task.

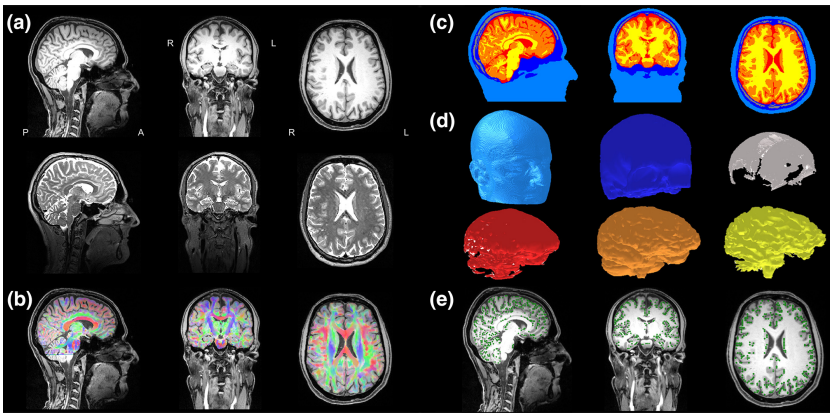

Figure 3.14: Six-compartment anisotropic realistic head model and source space. Adapted from https://onlinelibrary.wiley.com/doi/full/10.1002/hbm.24754

3.3.5 Inverse Problem

The Inverse Problem (IP) applied on non-invasive or invasive electromagnetic (EM) recording technologies is dedicated on estimating and modeling the spatiotemporal dynamics of neuronal currents that flow through the brain and induce the electric potentials and magnetic fields measured at sensor level. The Inverse Problem is also addressed in literature as Neuroelectromagnetic source imaging (NSI). The Inverse Problem is classified as ill-posed. To elaborate, the given sensor topography could be generated by an infinite number of active brain sources. The reason behind this, is the existence of sources who do not generate any measurable EM signals (silent sources) but they contribute to the solution without affecting the data fit. Assumptions that results in a priori information are a standard comping mechanism of non-uniqueness in order to restrict the solution space. Mainly, the assumptions made determine the nature of the sources, for example their quantity, anatomical and neurophysiological constraints, a priori probability density

functions and covariance models. Source localization accuracy depends on variant reasons such as head and source modelling errors and of course biological and non-biological noise.

3.3.6 Mathematical Formulation

Keeping in mind equation 3.51, the IP is summarized in finding an estimation $\hat{\mathbf{S}}$ of the dipole magnitude matrix given sensor positions and measurements $\mathbf{M}$, using the leadfield $\mathbf{L}$ calculated in the forward problem.

$$\hat{\mathbf{S}} = \mathbf{L}^{-1}\mathbf{M} \tag{3.71}$$

In mathematical terms, the ill-posed Inverse Problem is explained because of $N << p$, $\mathbf{L}$ is ill-conditioned and so equation 3.51 is under-determined. Moreover the forward model computed for the EEG data can be applied to solve the IP for the MEG data given that the magnetic field can be calculated by the electrical potential by integration.

Mathematical models aiming on the inverse solutions depend on assumptions about number, position, magnitude and orientation of dipoles and whether they are known or unknown. According to literature [70], [78], models can be classified as:

- Single dipole with unknown position, orientation and magnitude that change over time.
- A predetermined number of dipoles with predetermined unknown positions and orientations but different amplitudes.
- Predetermined dipole positions and different orientations and amplitudes.
- Different number of dipoles with constraints.

Regarding the dipole moments constraints, four models can be classified:

- Constant unknown dipole moment.

- Predetermined known dipole moment orientation and varying moment magnitude.
- Predetermined unknown dipole moment orientation with varying moment magnitude.
- Varying dipole moment orientation and magnitude.

The two main categories of Inverse Problem's solutions are the non-parametric and parametric methods [70]. Briefly, in non-parametric models a number of dipole sources with predetermined locations and orientations are allocated alongside the brain volume or cortical surface. Regarding the parametric methods, the aim is to find the best dipole position and orientation. The model consists either of a single dipole in a spherical head model or of multiple dipoles in a realistic head model. Also, dipole orientations can be predetermined or varying. On the other hand, non-parametric techniques estimate dipole's moment in a predetermined source space, leading on a linear problem. In this research work, only non-parametric methods have been used, so an attempt to briefly explain them is made. The mathematical derivation following is based on the Bayesian framework.

In order to define the conditional probability density of **M** given **S**, the likelihood density is given by the following formula:

$$p_{li}(m|s) = (\frac{1}{2\pi\sigma^2})^{\frac{N}{2}} exp(-\frac{1}{2\sigma^2}||m - \mathbf{L}s||_2^2) \tag{3.72}$$

Given **M** is ill-posed, the a-priori information of **S** is encrypted in its density probability $p_{pr}(s)$ and Bayes' rule is applied as follows [78]:

$$p_{post}(s|m) = \frac{p_{li}(m|s)p_{pr}(s)}{p(m)} \tag{3.73}$$

where p_{post} stands for the posterior, the conditional density of **S** given **M**. The derivation of point estimates for the values of **S** can be achieved either by *Maximum A-posteriori Estimate (MAP)* or the *Conditional Mean Estimate (CM)*. The first method uses the maximum of the posterior distribution (mode) while the second method is the mean or expected value of the

posterior [78]:

$$\hat{s}_{MAP} := \arg\max_{s\in\mathbb{R}^n} p_{post}(s|m) \tag{3.74}$$

$$\hat{s}_{CM} := \mathbb{E}[s|m] = \int dp_{post}(s|m)ds \tag{3.75}$$

In order to link the aforementioned methods with other widely used techniques *Gibbs distributions* are used as priors:

$$p_{pr}(s) \propto exp(-\frac{\lambda}{2\sigma^2}P(s)) \tag{3.76}$$

where *P(s)* is an energy function, affecting features independent of d and $\lambda > 0$ is called regularization parameter and scales the values of *P(s)*.

$$\begin{aligned}\hat{s}_{MAP} : &= \arg\max_{s\in\mathbb{R}^n}\left\{exp\left(-\frac{1}{2\sigma^2}||m-\mathbf{L}s||_2^2+\frac{\lambda}{2\sigma^2}P(s)\right)\right\} \\ &= \arg\max_{s\in\mathbb{R}^n}\left\{||m-\mathbf{L}s||_2^2+\lambda P(s)\right\}\end{aligned} \tag{3.77}$$

$$\hat{\mathbf{S}}_{MNE} = \mathbf{G}^T(\mathbf{G}\mathbf{G}^T+\lambda\mathbf{I}_m)^{-1}\mathbf{B}, p > m \tag{3.78}$$

3.3.7 Standardized low resolution brain electromagnetic tomography (sLORETA)

Standardized low resolution brain electromagnetic tomography (sLORETA) [70], [78], [79] is based on the standardized current density estimate given by the *MNE*.

For each source p *sLORETA* yields the estimate of standardized current density power:

$$\hat{\mathbf{S}}_{MNE,p}^T\{[\mathbf{V}_{\hat{\mathbf{S}}_{pp}}]\}^{-1}\hat{\mathbf{S}}_{MNE,p} \tag{3.79}$$

where $\hat{\mathbf{S}}_{MNE,p} \in \mathbb{R}^{3x1}$ is the current density estimate at the *pth* voxel given by the minimum norm estimate and $\{[\mathbf{V}_{\hat{\mathbf{S}}_{pp}}]\} \in \mathbb{R}^{3x3}$ is the *pth* diagonal block of $\mathbf{V}_{\hat{\mathbf{S}}}$ (*MNE* variance). Compared with the *MNE*, *sLORETA* yields the lowest

localization errors, according to noisy simulations [70]. Finally, *sLORETA* detects more accurately deep sources even multiple sources which are not temporally related or their leadfields are uncorrelated [17].

Chapter 4

Methodology and Results

In this chapter the methodologies followed and the experimental results are shown. The pipeline given in Fig. 3.1 is followed. Beginning from *preprocessing* an extended explanation of the methodlogy and the corresponding figures is given. Consequently, the *HFOs detection and clustering* module is further elaborated in the Fig. 4.12, while examples of HFOs and spurious events are given in order to assist the reader understanding the HFOs and the bottleneck of the detection algorithms in literature. The chapter continuous with the results in the section 4.3, where an explorative work regarding the solutions of the Forward Problem is given, while the main focus is on the *FEM head models* and *sLORETA* as a combination yielding more accurate results in terms of source estimation. On the other hand, in section 4.4 only the results of the combination *FEM head models* and *sLORETA* are shown. Finally, a brief comparison between HFOs-based and interictal spikes-based results is made.

4.1 Preprocessing and Spike Detection

In this research work measurements were acquired by EEG and MEG recording procedures, simultaneously. The MEG system was provided by a CTF setup from VSM MedTech Ltd. which was placed in a properly modified Magnetic Shielded Room and was equipped with 275 axial gradiometers of which the 4 were bad sensors. The EEG system is equipped with 72 HydroGel electrodes (along with 6 EOG and 1 ECG channel). Also, there are reference channels that record non-cerebral activity such as ocular and cardiac activity ('EOG' and 'ECG' channels) which are used for denoising techniques. Additionally, the subject underwent a Magnetic Resonance Imaging (MRI)

recording to obtain head's images for possible lesions and abnormal areas. The MRI system is a 3 Tesla MAGNETOM recording setup offering mm^3 accuracy by Siemens Medical Solutions. Data was acquired from a 49-year-old female suffering from drug resistant focal onset epilepsy since the second year of her life. The measurements were acquired by seven runs. During the first run (7 min long) skull conductivity was calibrated for the head model (stimulation of median nerve of patient's right arm with electrical pulses above the motor threshold) [17]. The rest six runs were 8 min long with sampling rate $2400Hz$ and interictal epileptic discharges were measured. The MRI recordings were performed on T1, T2 and Diffusion Tensor Imaging (DTI) sequences and were completed with $1.89mm$ edge length, one flat diffusion gradient image and 20 volumes. The subject signed all the consent forms which were approved by the ethics committee.

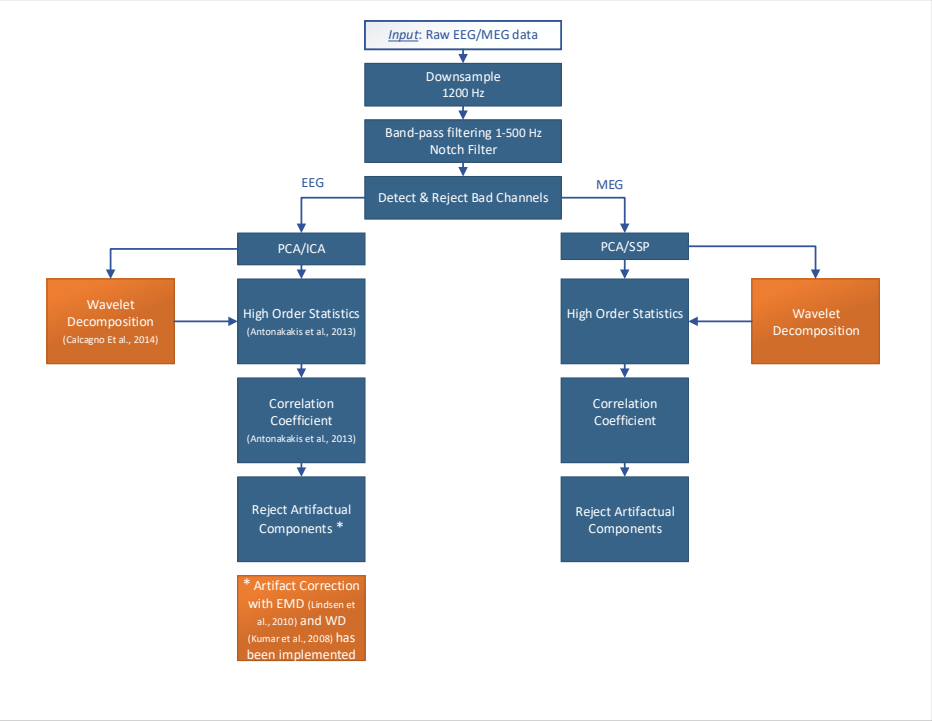

Figure 4.1: Preprocessing pipeline

As can be seen in Fig. 4.1, the first steps of the implementation are the downsampling, band-pass and notch filtering and the detection and rejection

of any bad channels. Those steps are applied independently on EEG and MEG data. On the other hand, the artifact correction process is different for each modality. PCA is applied on the EEG data in order to define the number of the Independent Components (IC) of ICA. The number of the components that explain the 95% of data's information has been defined by the metric PUI as explained in the subsection 3.1.2. The ICs that contain mostly artifactual activity are removed. For MEG data, PCA has been applied in order to find the spatial components that explain better the artifacts to be removed. The number of the Principal Components (PCs) is equal to the number of the MEG sensors. After the identification of the artifactual Principal Components, SSP calculates the linear projectors that will be applied on the recordings in order to correct them from the artifacts. The identification of the artifactual components in EEG and MEG recordings is a sophisticated approach which is depicted in Fig. 4.4. For the cleaning of the artifactual ICs two approaches have been implemented but not integrated yet into the preprocessing pipeline.

As explained in section 3.1, firstly the original data were sampled at $2400Hz$, initially and then downsampled by a sampling rate of $1200Hz$. In this research work, the band of interest ranges between $1Hz$ and $500Hz$. In that frequency range occur the most abnormal frequency activities ($1Hz - 100Hz$) [80] and also HFOs can be found ($80Hz - 500Hz$) [81]. In that case the implemented band-pass filter is a 4^{th} order (steep transition band) Butterworth (flat frequency response in the passband). The PLN is delivered at $50Hz$ (frequency of power utility in Europe) and its harmonics are removed by a Notch filter.

After filtering, it is important to inspect data on frequency domain and check filters implementation. As shown in Fig. 4.3, Notch filter removed any PLN and its harmonics on the corresponding frequencies.

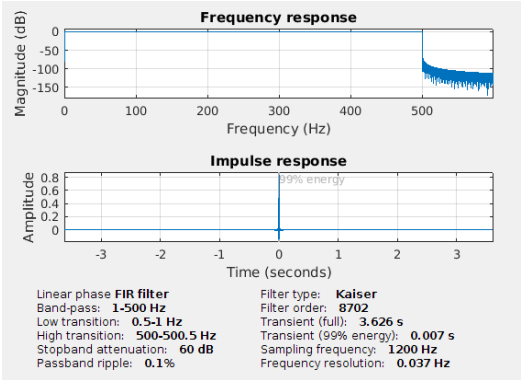

(a) Specifications of the used band-pass filter.

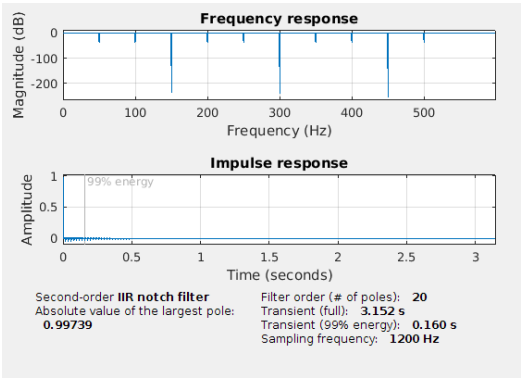

(b) Specifications of the used Notch filter.

Figure 4.2: Specifications of the used filters.

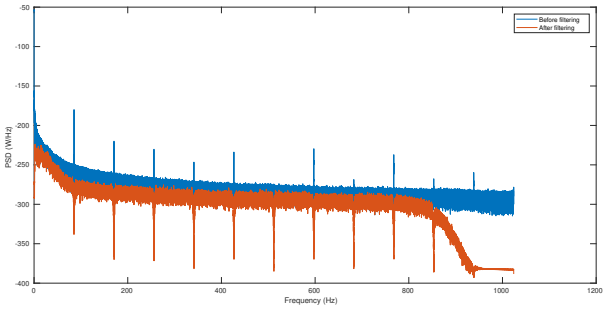

Figure 4.3: PSD of EEG channels before and after filtering

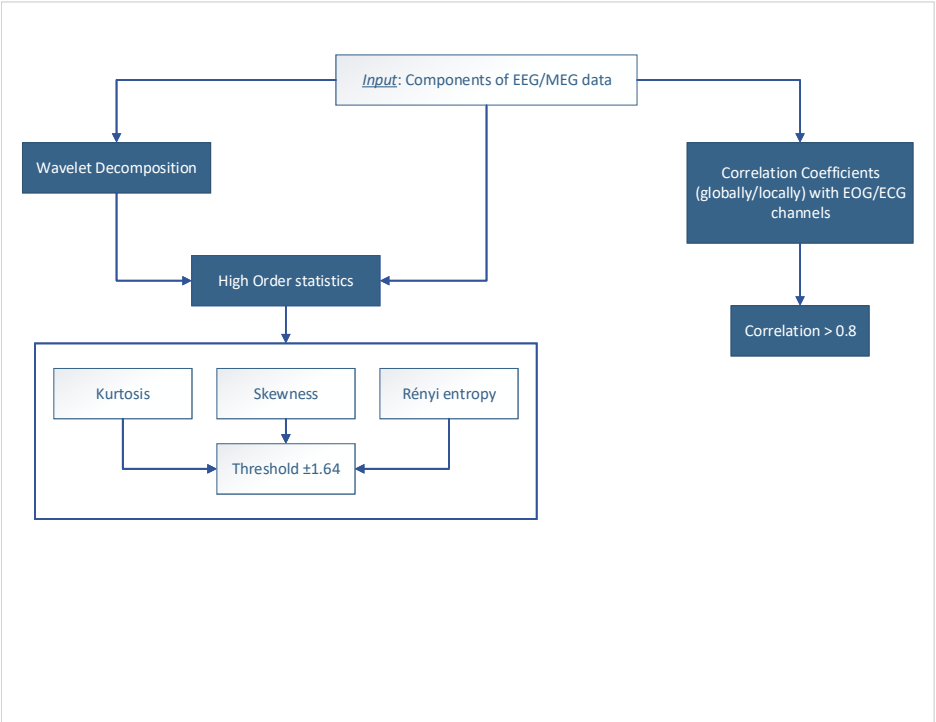

Figure 4.4: Pipeline for the detection of artifactual components

As the figure 4.4 illustrates, three different approaches have been implemented in order to identify the artifactual components. Firstly, correlation coefficients have been calculated between the components and the reference channels globally and locally. The term globally denotes that the correlation coefficients have been calculated upon all the duration of the component and the reference channels. Locally indicates that the components and the reference channels have been segmented into portions with duration $2s$. Correlation coefficients have been calculated for each segment. In order to classify a component as an outlier, the global correlation coefficients should be greater that 0.8 and the local correlation coefficients should exceed the threshold of the 0.8 in more than 20% of the segments [82], [83]. The local correlation coefficients approach is applied only for the identification of ocular activity. Ocular activity is non-periodic and spontaneous while cardiac activity appears periodically and contaminates the component alongside its whole duration. On the second approach High Order Statistics have been

calculated directly on the components. The metrics that have been used are the *Kurtosis*, *Skewness* and *Rényi entropy*. A component is classified as an outlier if the z-scored values of the metrics exceed the empirically defined threshold which is set to ±1.64. Finally, Wavelet Decomposition (WD) is applied on each component. High Order Statistics are calculated on all the wavelet coefficients that WD yielded. The same thresholding technique (with the application of HOS directly on the components) has been followed to identify the outlier components. Even though a complicated artifact correction methodology has been implemented the results are always inspected visually in order to avoid any false identifications.

In Fig. 4.5 the topologies of the ICs of the EEG data are depicted. The typical artifactual topographies are *IC2* and *IC8* for ocular and cardiac activity, respectively.

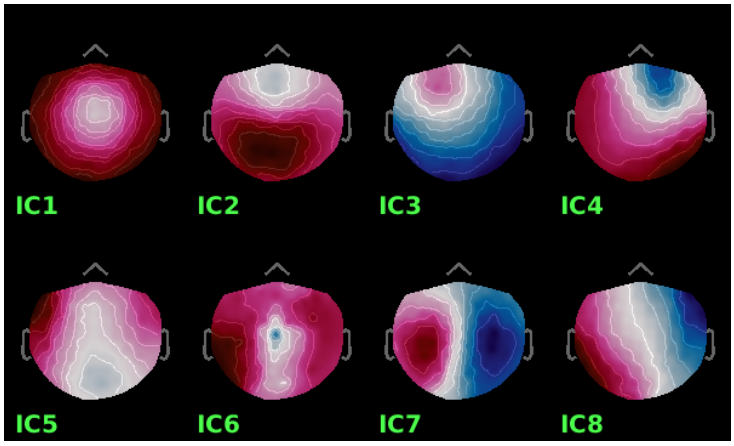

Figure 4.5: Topographies of ICs of EEG data

Although *IC1* does not depict a typical artifactual topography, by observing the corresponding time series in Fig. 4.6a some eye movement can be spotted, such as saccades and blinks. This case explains the necessity of implementing an artifact detection algorithm since the topography is not always representative of the activity.

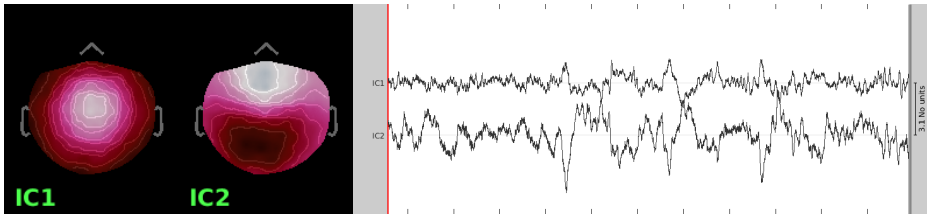

(a) ICs containing ocular activity

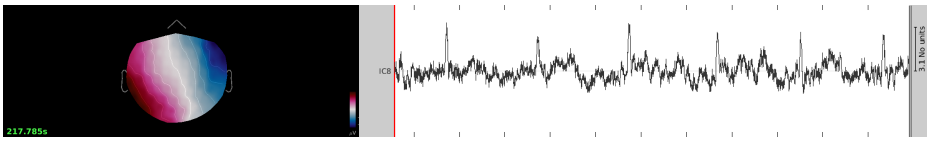

(b) IC containing cardiac activity

Figure 4.6: Artifactual ICs

In Fig. 4.7, the subfigures 4.7a, 4.7b, 4.7c illustrate the z-scored High Order Statistics calculated in time. All metrics classify *IC6* as an outlier. According to Fig. 4.5 *IC6* does not illustrate a representative topography of cardiac artifact so it is not classified as an outlier. On the other hand in the subfigures 4.7d, 4.7e and 4.7f the z-scored High Order Statistics are calculated on the ICs wavelet coefficients and yield better results. The metrics classify as outliers *IC1* and *IC8* which contain ocular and cardiac activity, respectively. This example enhances the contribution of WD on the detection of the artifactual components.

For the MEG data, PCA is applied for each type of artifact in order to identify the spatial components of the artifact to be removed. Consequently, SSP is applied separately for the correction of each type of artifact. Firstly, many examples of the artifact to be removed have been identified. A short time window is extracted around each of these event markers and all the small blocks of the recordings are concatenated in time. PCA is applied on the concatenated artifacts in order to get a decomposition in various spatial components (number of components = number of sensors). The aim is to identify the spatial components that are representative of the artifacts to be removed. The pipeline depicted in Fig. 4.4 is followed to identify the most representative spatial components. A linear projector for each spatial component to remove is computed and applied on the recordings. As explained in

subsection 3.1.7 the order matters so components containing cardiac activity are calculated first.

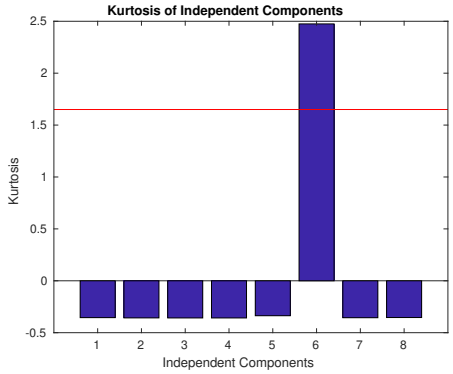

(a) Z-scored kurtosis of ICs

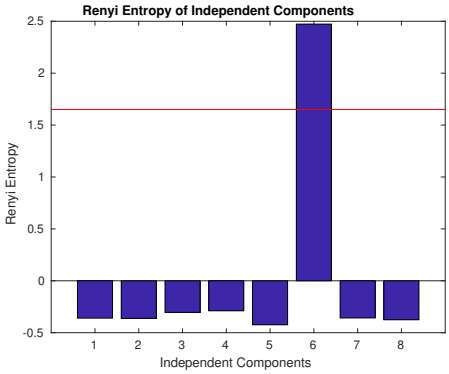

(b) Z-scored Rényi entropy of ICs

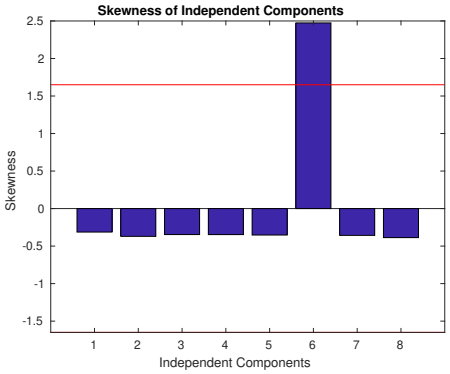

(c) Z-scored skewness of ICs

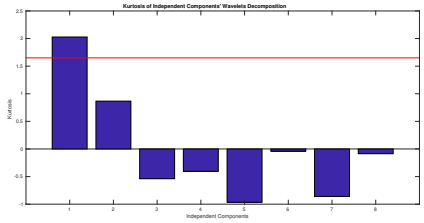

(d) Z-scored kurtosis of ICs wavelet coefficients

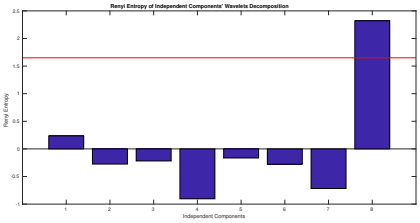

(e) Z-scored Rényi entropy of ICs wavelet coefficients

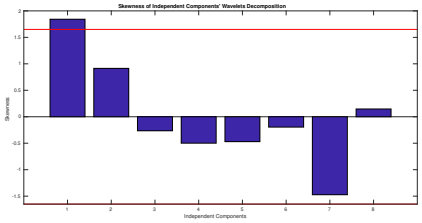

(f) Z-scored skewness of ICs wavelet coefficients

Figure 4.7: High Order Statistics on ICs

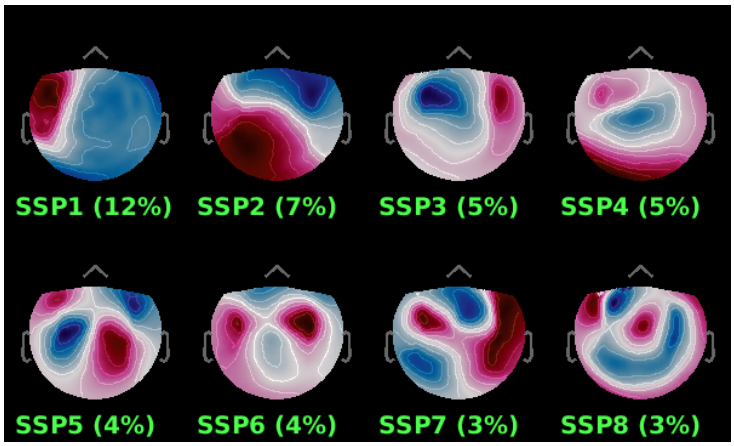

(a) Spatial Components of cardiac activity

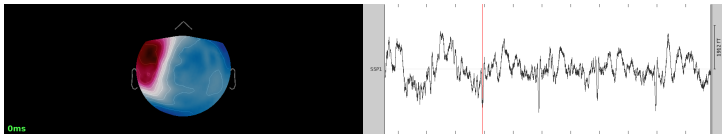

(b) Spatial Components of cardiac activity to remove. *Spatial component 1* illustrates a representative topography of cardiac activity.

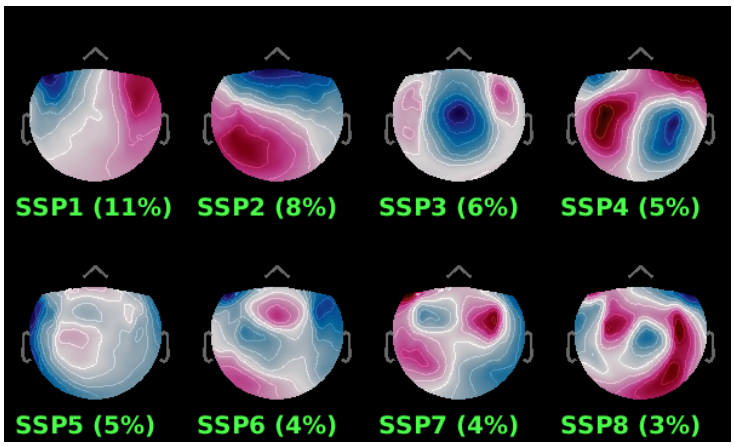

(c) Spatial Components of ocular activity

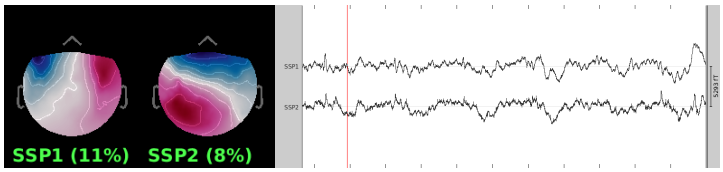

(d) Spatial Components of ocular activity to remove. *Spatial component 1* and *2* illustrate representative topographies of ocular activities.

Figure 4.8: Spatial components of MEG data. The percentage denotes the normalized singular value of each component. It indicates the amount of signal that was captured by the component during the decomposition. Higher percentages indicate that the component is more representative of the artifact recordings that were used to calculate it.

The artifact correction approach should be concentrated only on the artifactual activity without affecting the useful brain information. In this research work the annotated spikes are the useful information that will be examined. In order to assure that the annotated spikes have been remained intact after the implementation of the preprocessing, each spike has been segmented into a trial from $[-0.5s, 0.5s]$, where *zero* is mapped to the peak of the spike and all trials have been arithmetically averaged. This approach has been implemented for the spikes before and after the preprocessing and independently for the MEG and EEG spikes.

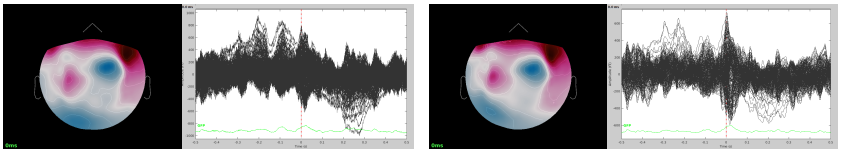

(a) Averaged MEG spikes before artifact correction

(b) Averaged MEG spikes after artifact correction

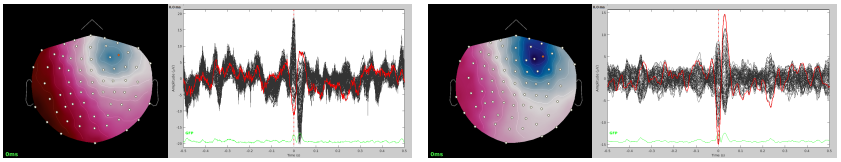

(c) Averaged EEG spikes before artifact correction

(d) Averaged EEG spikes after artifact correction

Figure 4.9: Examination of annotated spikes before and after artifact cleaning.

Comparing the Fig. 4.9a and 4.9b, no significant differences can be spotted. In Fig. 4.9b the topology in the vicinity of the left FCD is slightly enhanced and also the amplitude of the spikes' peaks. For the EEG spikes, the channel with maximum negativity (F6) is depicted in red colour (EEG-dominant epilepsy case). Comparing the Fig. 4.9c and 4.9d, the topography after the preprocessing has been enhanced, illustrating clearly the maximum negativity at F6 and that the amplitudes of the spikes' peaks have been significantly increased.

As it is shown in 4.1 for the correction of the artifactual ICs two approaches have been implemented but not integrated yet into the preprocess-

ing pipeline. These approaches are based on the local correlation coefficients and they are used to correct only ocular activity. The aim is to correct only the segments of the components that have been contaminated. The contaminated segments have been detected by the local correlation coefficients approach and they are corrected using Empirical Mode Decomposition (EMD) and Wavelet Decomposition (WD), independently.

EMD calculates the Intristic Mode Functions (IMFs) of the contaminated segments. A thhresholding technique is applied in order to classify the IMFs that contain mostly ocular activity. Specifically, the standard deviation (SD) of all IMFs is calculated and the IMFs that their SD is α times bigger than the SD of the first IMF are classified as artifactual. Mathematically speaking, $SD_1 < \alpha SD_i$, where $i = 1, ..., N$, N stands for the number of IMFs and α is empirically defined. In Fig. 4.10, $IMF3 - IMF5$ contain ocular activity. For the segment's reconstruction only the remaining IMFs have been used. The corrected signal consists of the sum of the IMFs which satisfy the aforementioned inequality. In Fig. 4.11a an example of a contaminated signal is illustrated before and after the correction of the blinks.

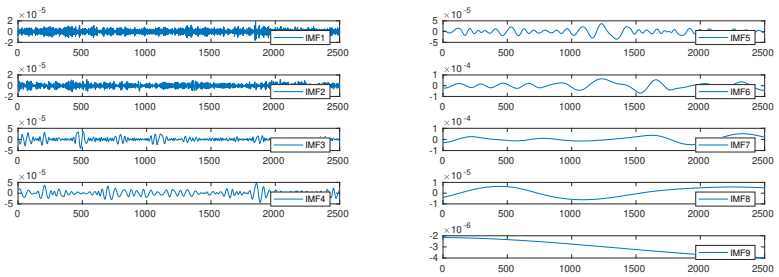

(a) Intrinsic Mode functions high frequencies

(b) Intrinsic Mode functions low frequencies

Figure 4.10: IMFs after EMD has been applied on a specific segment

WD transforms the contaminated segments into time-frequency domain. Daubechies have been used as mother wavelet and the decomposition level is 3. A thresholding technique has been applied on all the wavelet coefficients. Specifically, the amplitude of the wavelet coefficients that exceed the threshold are downscaled by a factor 0.2. The threshold is defined as the product

of a regularization factor and the segment's standard deviation. In Fig. 4.11 a comparison between the two methods is made. In both examples the initial contaminated segment is the same. In 4.11a the reconstructed signal is clear of the blinks but it is possible that some useful information has been extracted, too. On the other hand, the WD approach interferes less to the signal and downscales the blinks.

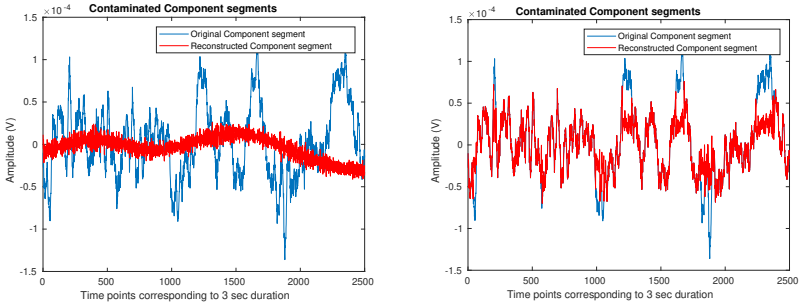

(a) EMD example (b) WD example

Figure 4.11: Comparison between EMD and WD artifact correction. EMD discards a lot information of the signal, while WD it is possible to form sharp peaks while downscaling the wavelet coefficients.

The main advantage of both approaches is that interfere only on segments containing non-cerebral activity, leaving intact portions of the component that may contain useful information.

4.2 HFOs detection and clustering

For the HFOs detection the algorithm explained in Fig. 3.2 in section 3.2 has been implemented. The algorithm has been applied independently for the EEG and MEG data. From now on, HFOs detected on EEG data will be called EEG HFOs and HFOs detected on MEG data will be referred to as MEG HFOs. The algorithm searches for HFOs in the time vicinity of the annotated spikes. Specifically, a time window with duration $10ms$ around the spikes is examined. Given the topologies in Fig. 4.9d and 4.9b in section 4.1 the regions responsible for the underlying epileptic activity are known. This a-priori information is used to examine only the corresponding sensors

for any possible HFOs. As it is illustrated in Fig. 4.12 the input of this module is the preprocessed EEG and MEG data. A high-pass filter between the frequencies $80 - 500Hz$ is applied on the recordings because HFOs live in that frequency range. The module give two outputs: clustered EEG and MEG HFOs.

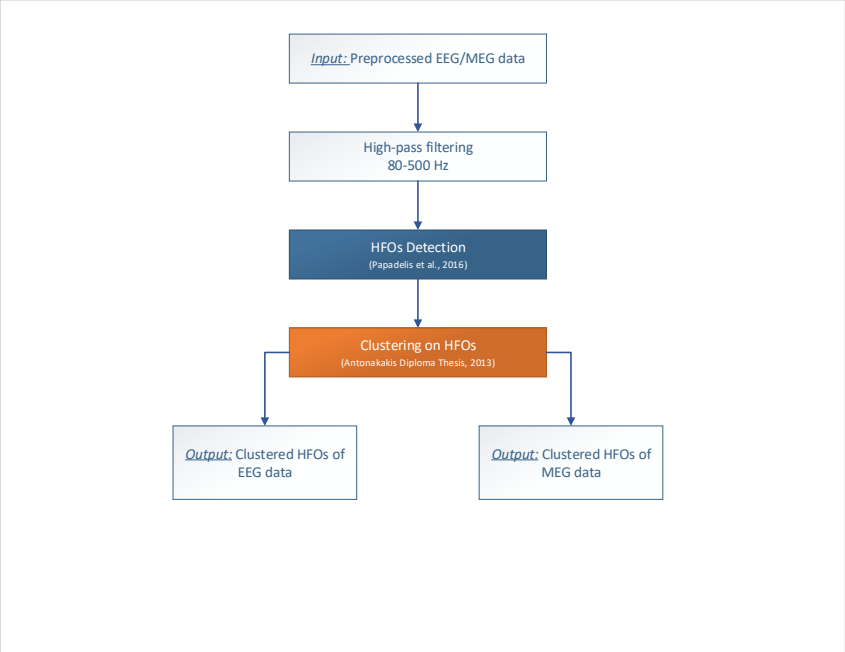

Figure 4.12: Pipeline of the HFOs detection and clustering module

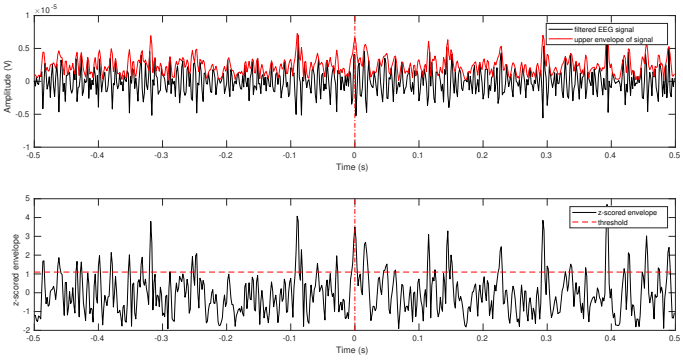

Figure 4.13: Filtered signal and Hilbert Transform

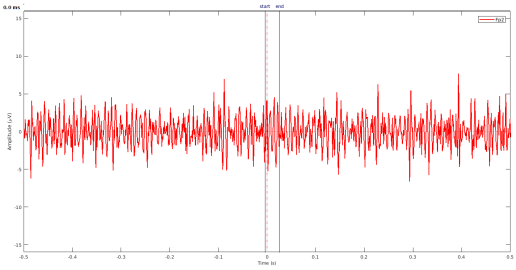

(a) Filtered EEG signal. The starting and ending point of the HFOs are denoted. The red dotted vertical line denotes the peak of the event.

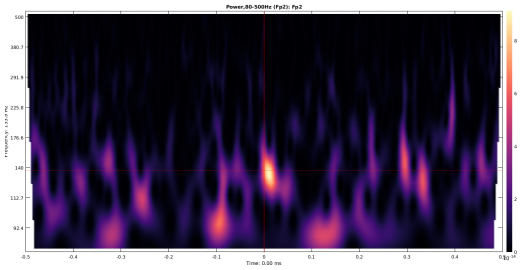

(b) Time-frequency representation of filtered EEG signal.

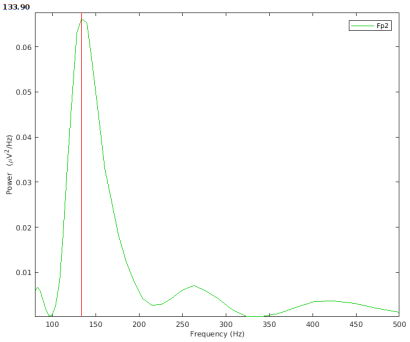

(c) Instantaneous Power Spectrum of the peak.

Figure 4.14: Example of a detected EEG HFOs.

In Fig. 4.13 an example of a segment of a signal is illustrated. Specifically, in the upper subfigure the segments of the signal and its corresponding upper envelope are illustrated. Signal's envelope has been calculated using Hilbert Transform. In the lower subfigure the z-scored upper envelope of the channel's segment is illustrated. The red vertical line denotes the threshold while the vertical red line denotes the peak of an event that exceeds the threshold.

In Fig. 4.14 is illustrated an example of a detected EEG HFOs. In 4.14a is shown the segment of the signal that the HFOs detected. The starting and ending point of the event are denoted by the blue vertical lines, while the red vertical line denotes the peak of the event. The event consists of at least 4 oscillations in order to be well-distinguished from spurious EEG activity or transient events. An indispensable part of the algorithm is to

review the segment of the event in time-frequency domain. In Fig. 4.14b the segment of the channel depicted in 4.14a has been transformed using Morlet Transformation. The vertical line denotes the peak of the HFOs. As can be seen, the signature of the event is well-restricted in frequency, well-distinguishable from the background and resembles an isolated island it time-frequency domain. In 4.14 the instantaneous power spectrum of the peak is above the $80Hz$ as it is required.

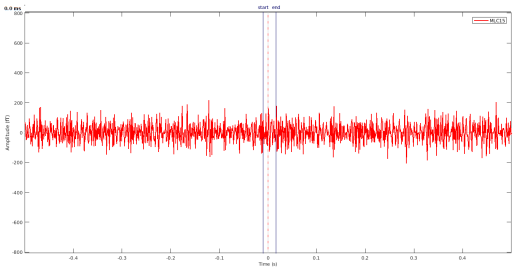

(a) Filtered MEG signal. The starting and ending point of the HFOs are denoted.

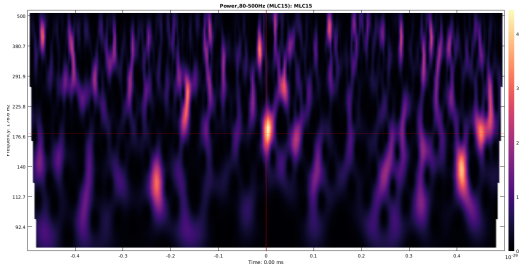

(b) Time-frequency representation of filtered MEG signal.

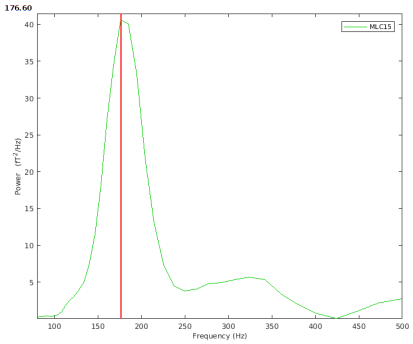

(c) Instantaneous Power Spectrum.

Figure 4.15: Example of a detected MEG HFOs.

In 4.15 is illustrated an example of a detected MEG HFOs. Similarly with the Fig. 4.14, the event consists of at least 4 oscillations, its signature in frequency is well- restricted and represented by an isolated peak in time-frequency plot (restricted activity that resembles an "island"). In 4.15c the instantaneous power spectrum of the peak is above the $80Hz$ as it is required and well-distinguishable from the background activities.

In Fig. 4.16 an example of a false identification is given in order to fully understand the importance of visual inspection in time-frequency domain. As can be seen in Fig. 4.16a the peak of the event exceeds the threshold and in Fig. 4.16b more than 4 oscillations between the starting and ending point of the event can be distinguished. However, the time-frequency plot gives valuable information of the event's frequency signature as it is extended as an elongated blob. Also, the instantaneous power spectrum of the peak is not above $80Hz$ as it is required for an event to be considered as an HFOs. That event has been excluded from the process.

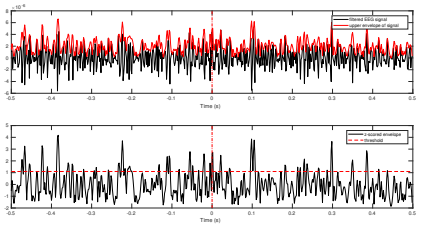

(a) Upper Fig: filtered signal and its upper envelope. Lower Fig.: z-scored upper envelope of the filtered signal.

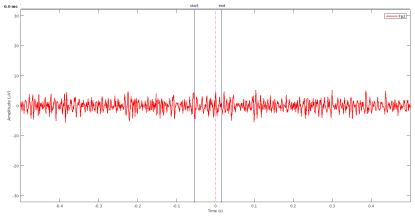

(b) Event on filtered signal. The starting and ending point of the event are denoted.

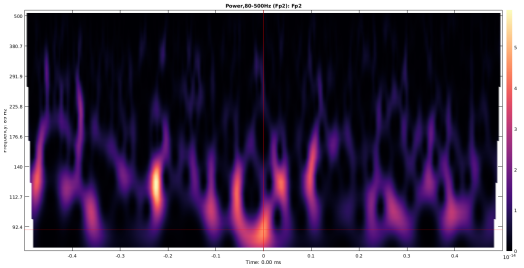

(c) Time-frequency representation of filtered signal.

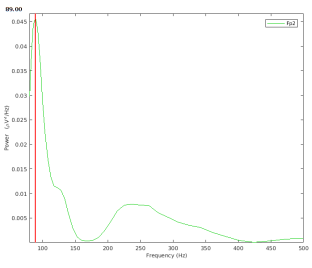

(d) Instantaneous Power Spectrum.

Figure 4.16: Example of **erroneous** HFOs detection.

Visually inspection of the EoIs in time-frequency domain is an indispensable part of the algorithm and a laborious and time-consuming task. Since it is a humans in the loop process, errors caused by the human factor are possible. In order to restrict the false identifications one more step has been added to the detection algorithm. All the HFOs that have been detected and visually reviewed are grouped into clusters according to their energy.

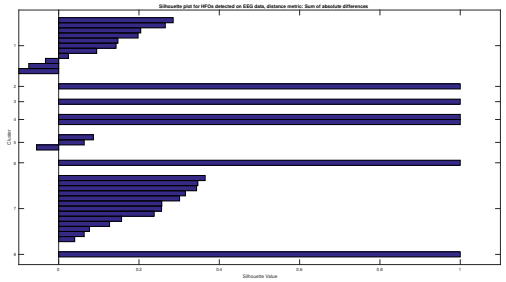

(a) Silhouette plot for optimal number of clusters in EEG

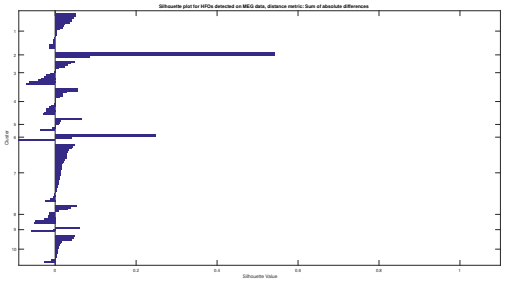

(b) Silhouette plot for optimal number of clusters in MEG

Figure 4.17

The clustering is implemented by *K-means* algorithm with energy feature. *K-means* requires as input the number of clusters. The optimal number of clusters is selected by silhouette plots. In Fig. 4.17 the silhouette plots for the HFOs detected on EEG and MEG data are depicted. For the EEG HFOs the cluster that yielded optimal results in terms of source reconstruction is the 1^{st}, while for MEG HFOs is the 6^{th} cluster.

The HFOs of each cluster are arithmetically averaged in time domain. In Fig. 4.18a the averaged EEG HFOs are shown. The red vertical dotted line denotes the peak of the averaged events at $0s$ while the duration of the trials is $1s$ ($[-0.5s, 0.5s]$ around the HFOs peak). As can be seen the peaks of the HFOs are significantly enhanced. A fact that is clearly observed in Fig. 4.18b. On the other hand, in Fig. 4.18c the peaks of the averaged MEG HFOs are not clearly distinguishable from the background. In Fig.

4.18d is clearly shown that the peak of the averaged MEG HFOs have been significantly attenuated.

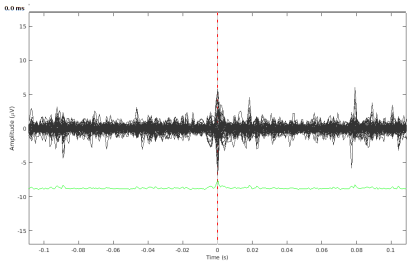

(a) Averaged EEG HFOs

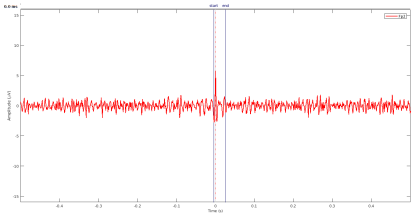

(b) Channel example of averaged EEG HFOs

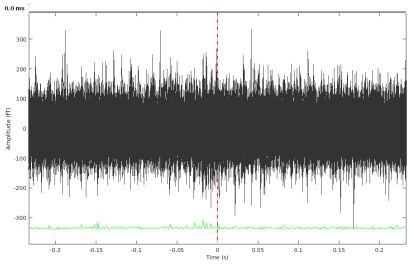

(c) Averaged MEG HFOs

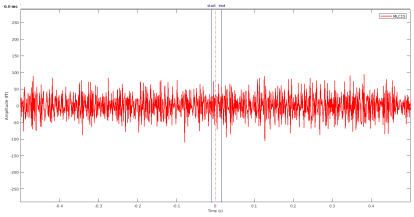

(d) Channel example of averaged MEG HFOs

Figure 4.18: Averaged HFOs

4.3 Interictal Spikes-based Source Analysis

The aim of this section is to explore the brain areas which generate the epileptic activity. The source estimation is based on interictal spikes, well established and widely used biomarkers of epilepsy. An explorative approach has been followed, using different Forward Models and Inverse Solutions in order to designate the most appropriate combination of the aforementioned for the current subject.

Overall, all the Forward Solutions are based on the subject's head anatomy in order to obtain accurate and realistic solution for the Inverse Problem. Briefly, for the EEG data, the Forward Models which have been tested are *3-shell sphere*, *BEM* (based on FieldTrip implementation [84]) and *FEM* (based on FieldTrip implementation [84]). All this methods used only the T1 image MRI scan in order to generate the head model, while for MEG data *single-sphere* was used as a head model obtained from the T1 image MRI scan. In order to obtain accurate and realistic results by the Inverse Problem, the Forward Problem was solved using FEM as a head model combined with Venant principle. The FEM uses hexahedral as finite elements and the head model includes brain anisotropy and calibrated skull conductivities. The head model consists of six tissues (skin, skull compacta, skull spongiosa, CSF, gray and white matter) and it is constructed by the images of MRI $T1w-$ and $T2w-$ using MATLAB and SPM12, FieldTrip [84]. Finally, combined EEG/MEG (EMEG) approach has been tested, only for the FEM head modelling case. The source space has 40468×3 dimensions while the leadfield used for the reconstruction is a concatenated form of the EEG and MEG leadfield. In all cases tested the noise covariance has been calculated around $[-500ms, -200ms]$ before the spike's rising flag. *sLORETA* yielded more satisfying results in terms of source estimation. The regularization parameter λ has been empirically set equal to 25.

For the demonstrating results, the Forward Problem has been solved using *3-shell sphere*, *single-sphere* and *FEM*, while for the Inverse Problem solution, *sLORETA* has been applied.

EEG data and 3-shell sphere head modeling

The *3-shell sphere* as depicted in Fig. 4.19, is estimated based on scalp. The sphere is aligned with brain.

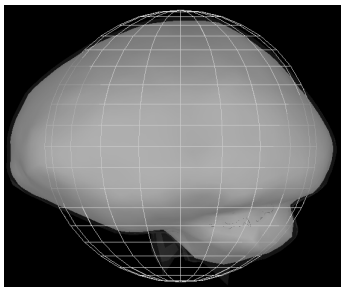

Figure 4.19: *3-shell sphere* as head modeling.

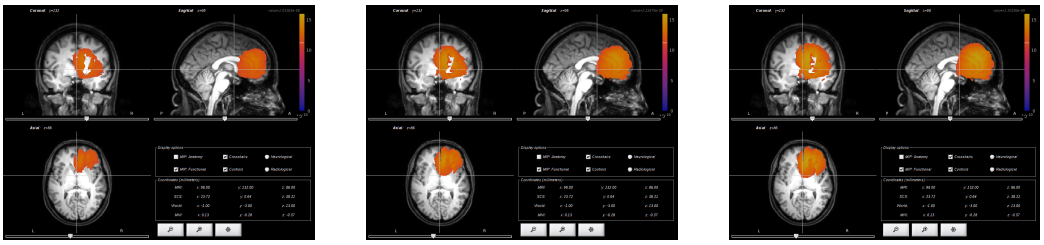

(a) $-5\ ms$ (b) $-3.3\ ms$ (c) $0\ ms$

Figure 4.20: Source estimation on EEG data: *3-shell sphere* head model and sLORETA.

The Fig. 4.20 depicts the results yielded from *sLORETA* for different time instances. As can be seen, the left fronto-central FCD is not detected and the propagation phenomenon, which begins from the fronto-central FCD and ends at the right FCD, is also not illustrated. However, a gradually increasing brain activity is depicted on the different time instances encircling the right FCD and an extensive region around it. A threshold of 70% of the maximum activation has been applied in order to display the final maps.

MEG data and single sphere head modeling

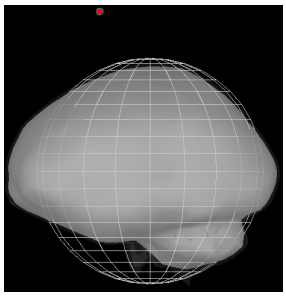

Figure 4.21: *Single sphere* as head modeling.

In Fig. 4.21, the head model has been estimated based on scalp.

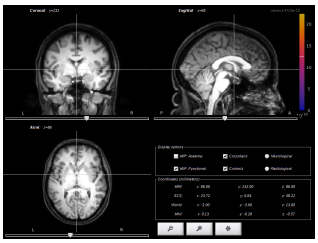

(a) $-5\ ms$

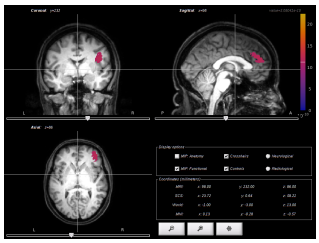

(b) $-3.3\ ms$

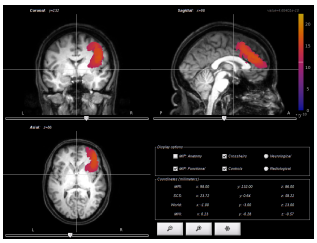

(c) $0\ ms$

Figure 4.22: Source estimation on MEG data: *single sphere* head model and sLORETA.

By observing Fig. 4.22 at $-5ms$, no source activity has been detected. At $-3.3ms$ source activity can be detected on the vicinity of the right FCD which gradually increased until $0ms$. The subtle left FCD is undetectable by MEG, too. As can been observed on the following results, using FEM to solve the Forward Problem, the Inverse Problem yields accurate spatial results for different time instances before the seizure onset. In Fig. 4.23, EEG fails to detect the left FCD but still illustrates source activity at the central brain region at $-23.3ms$. The propagation phenomenon is shown. In Fig. 4.24, source activity around the vicinity of the subtle left FCD has been detected, which propagates across the different time instances from the left to the right brain region. The right FCD is well-detected.

EEG data and FEM head modeling

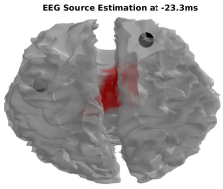

(a) $-23.3\ ms$

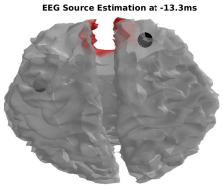

(b) $-13.3\ ms$

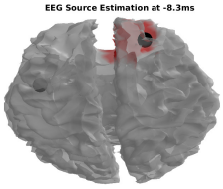

(c) $-8.3\ ms$

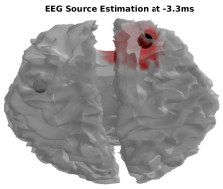

(d) $-3.3\ ms$

Figure 4.23: *FEM head model* and *sLORETA* on EEG spikes.

MEG data and FEM head modeling

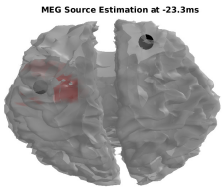

(a) $-23.3\ ms$

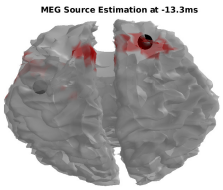

(b) $-13.3\ ms$

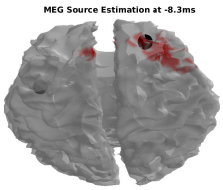

(c) $-8.3\ ms$

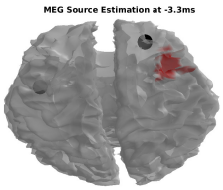

(d) $-3.3\ ms$

Figure 4.24: *FEM head model* and *sLORETA* on MEG spikes.

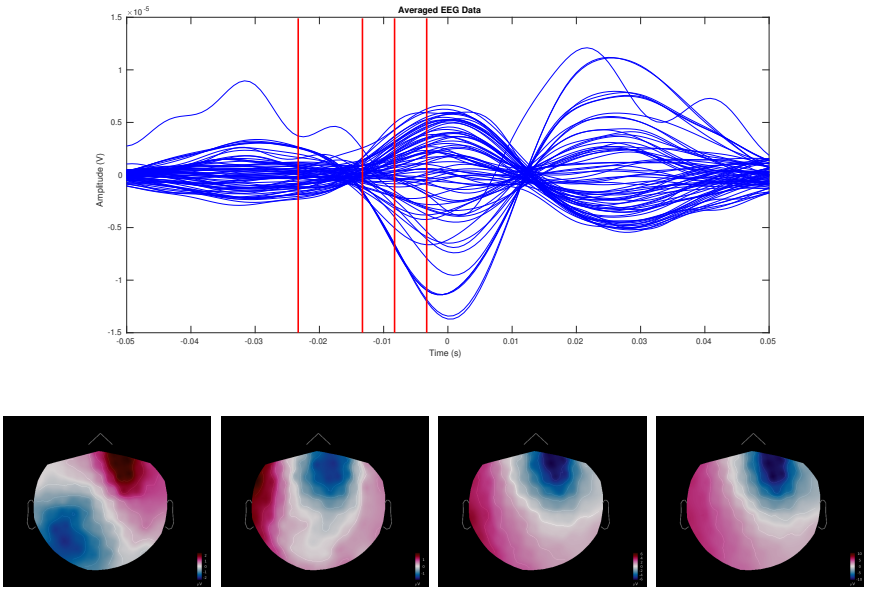

(a) $-23.3\ ms$ (b) $-13.3\ ms$ (c) $-8.3\ ms$ (d) $-3.3\ ms$

Figure 4.25: Topologies of averaged spikes on EEG.

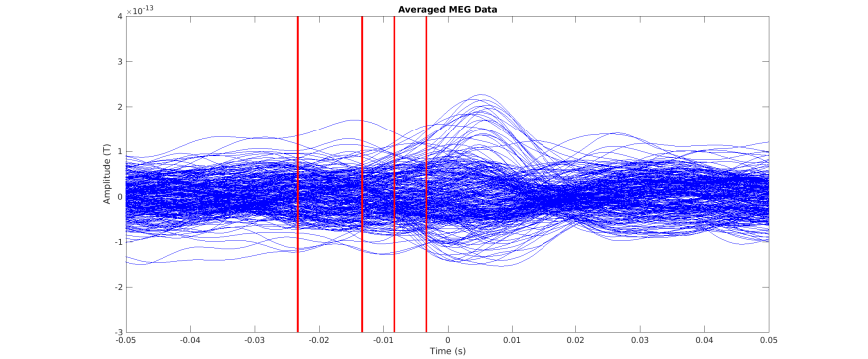

(a) $-23.3\ ms$ (b) $-13.3\ ms$ (c) $-8.3\ ms$ (d) $-3.3\ ms$

Figure 4.26: Topologies of averaged spikes on MEG.

In Fig. 4.25 the corresponding topographies of the time instances source reconstruction can been observed. Topographies are, also, a valuable source of information since on EEG they clearly depict only the right FCD with maximum negativity at F6 channel. Compared to the Fig. 4.25, in Fig. 4.26 the left FCD is detected by MEG, an observation deriving from source reconstruction, too. The topographies show not corrected ocular activity, which have been remained intact on purpose in order to not discard any useful information, currently the interictal spikes.

EMEG data and FEM head modeling

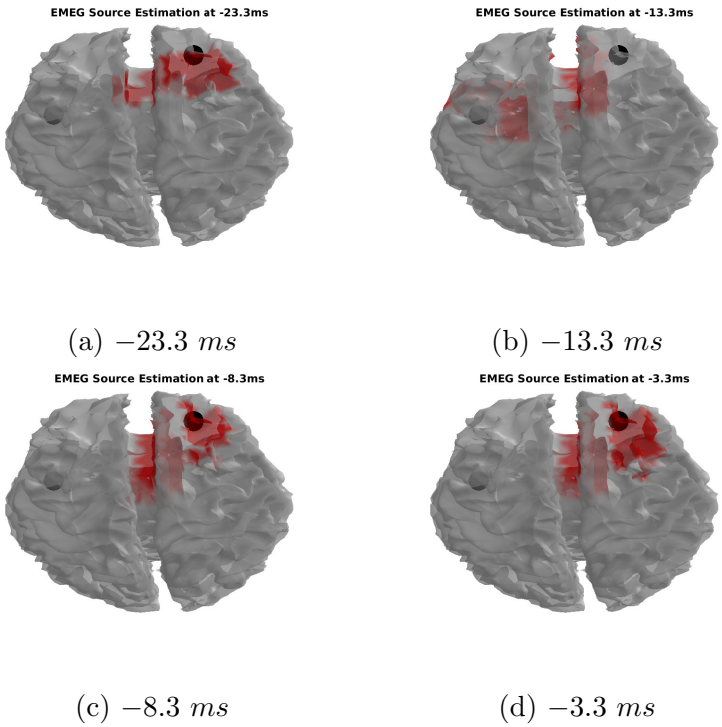

(a) $-23.3\ ms$ (b) $-13.3\ ms$

(c) $-8.3\ ms$ (d) $-3.3\ ms$

Figure 4.27: *FEM head model* and *sLORETA* on EMEG spikes.

In Fig. 4.27 the results of the combined EEG/MEG are shown. Brain activity is more pronounced in EEG compared to MEG. At $-23.3ms$ the contribution of MEG can been seen since there is source activity in vicinity of the left FCD. The right FCD is detected including an extended brain region.

4.4 HFOs-based Source Reconstruction

For the HFOs-based source reconstruction the Forward Problem has been solved using the same realistic FEM head modeling in section 4.3. Specifically, the leadfields calculated to solve the Forward Problem of the cases described in 4.3 has been used for solving the Forward Problem of the HFOs-based source reconstruction. The Inverse Problem has been solved using *sLORETA*. As explained in section 4.2 HFOs were grouped in clusters. Source reconstruction was applied on each HFOs cluster. For the EEG HFOs the cluster that yielded optimal results in terms of source reconstruction is the 1^{st}, while for MEG HFOs is the 6^{th} cluster. Only the results of those clusters are shown in this section.

EEG data and FEM head modeling

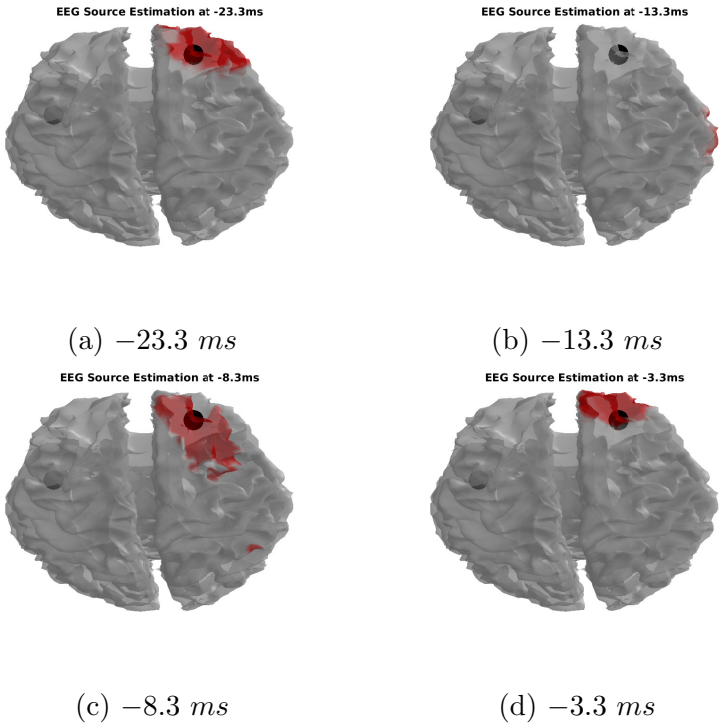

(a) $-23.3\ ms$ (b) $-13.3\ ms$

(c) $-8.3\ ms$ (d) $-3.3\ ms$

Figure 4.28: *FEM head model* and *sLORETA* on EEG HFOs.

As can be seen in Fig. 4.28, EEG fails to detect the left FCD but detects accurately the right FCD. The same behaviour can be seen in the section 4.3. EEG is unable to detect any source activity around the left FCD, but it detects accurately the right FCD.

MEG data and FEM head modeling

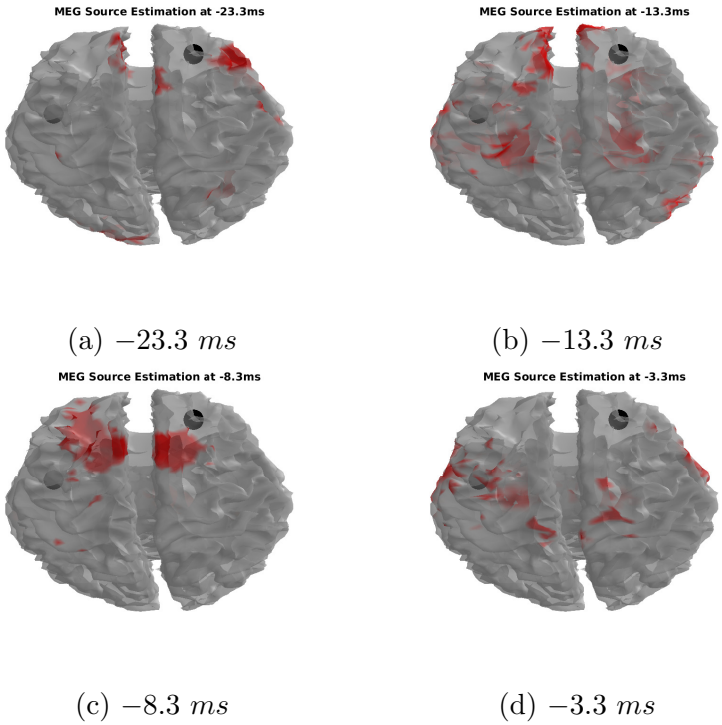

(a) $-23.3\ ms$ (b) $-13.3\ ms$

(c) $-8.3\ ms$ (d) $-3.3\ ms$

Figure 4.29: *FEM head model* and *sLORETA* on MEG HFOs.

The Fig. 4.29 illustrates the source estimation results from MEG data. The source maps show extended activity, some of which is placed in the vicinity of the left FCD. However, there are, also, more brain regions highlighted while the right FCD is not accurately detected.

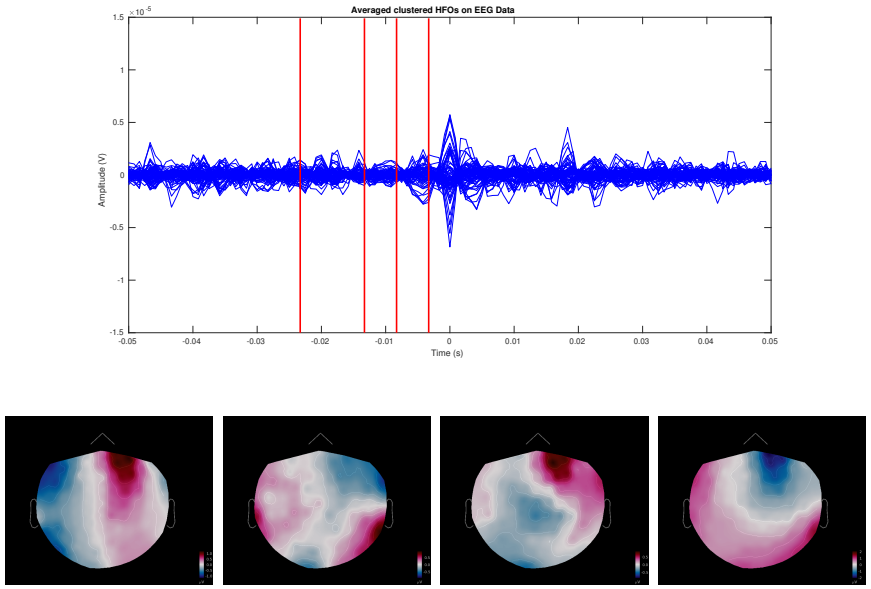

(a) $-23.3\ ms$ (b) $-13.3\ ms$ (c) $-8.3\ ms$ (d) $-3.3\ ms$

Figure 4.30: Topologies of averaged HFOs on EEG.

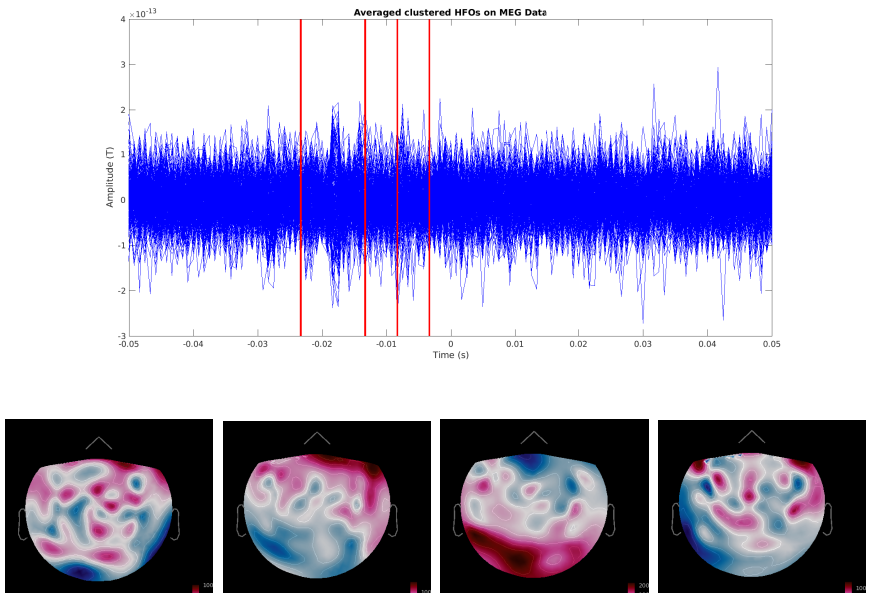

(a) $-23.3\ ms$ (b) $-13.3\ ms$ (c) $-8.3\ ms$ (d) $-3.3\ ms$

Figure 4.31: Topologies of averaged HFOs on MEG.

In Fig. 4.30 the topographies of the averaged EEG HFOs show a clear resemblance with the corresponding topographies of the averaged spikes. In concordance with the spikes-based source reconstruction at the time instance $-3.3ms$, negativity is spotted on the right FCD. The difference is that maximum negativity is shifted upwards at FP2 channel. Similarly with the spikes-based source reconstruction, EEG fails to illustrate the subtle left FCD. In Fig. 4.31d the topography shows brain activity around the two FCDs.

EMEG data and FEM head modeling

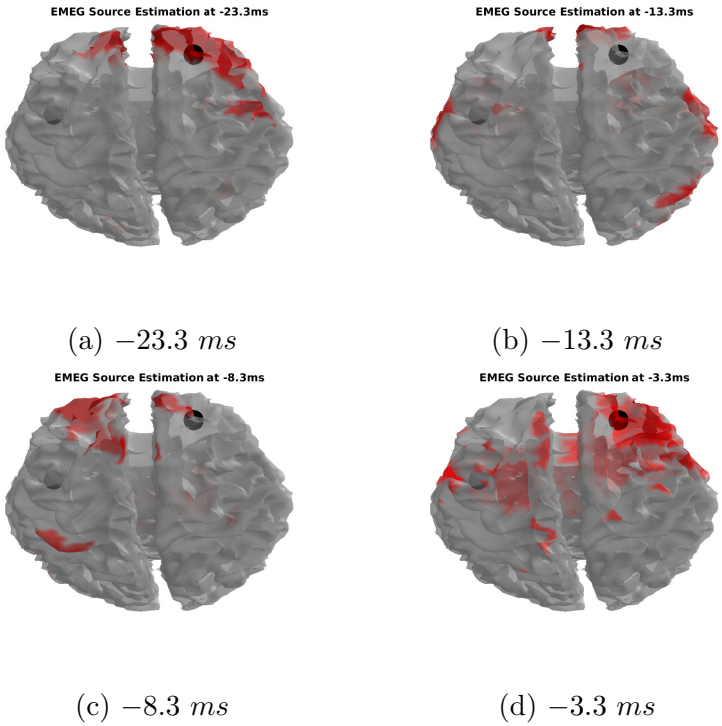

(a) $-23.3\ ms$ (b) $-13.3\ ms$

(c) $-8.3\ ms$ (d) $-3.3\ ms$

Figure 4.32: FEM head model and sLORETA on EMEG HFOs.

In Fig. 4.32 the combined EMEG can detect the right FCD and yields source activity in the left FCD, which is the contribution of the MEG. In concordance with the results in 4.3, HFOs-based source reconstruction results show an EEG-dominant epilepsy case.

4.5 Comparison between HFOs-based and Interictal Spikes-based Source Analysis

In order to compare the results of the HFOs-based and Interictal Spikes-based Source Analysis, a table of a specific time instance of the source localization for all modalities is shown. The holy grail of the presurgery epileptic studies is to accurately localize the seizure onset zone and therefore the epileptic zone. HFOs and Interictal Spikes are used as indicators of the seizure onset zone. The question that arises is if the HFOs are capable or even better indicators of the Interictal Spikes. According to the Fig. 4.33, HFOs indicate the right FCD accurately. Interictal Spikes yield source activity on the vicinity of the left FCD and also, seem to detect the propagation phenomenon. However, HFOs yield source activity closer to seizure onset zone that Interictal Spikes.

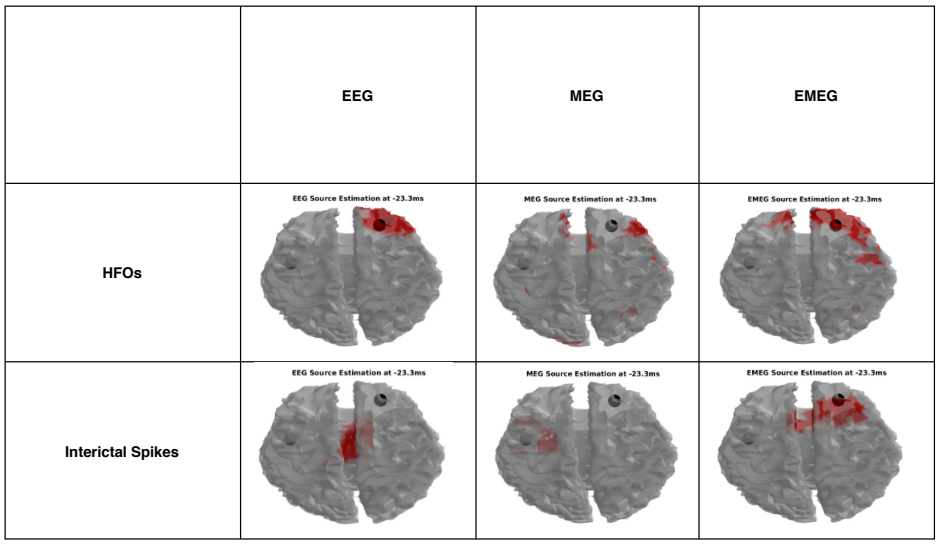

Figure 4.33: Comparison between HFOs-based and Interictal Spikes Source Analysis.

Chapter 5

Discussion, Conclusion and Future Work

5.1 Discussion

In this thesis an explorative work at low and high frequencies independently has been done. The aim of this thesis is to study HFOs as indicators of the seizure onset zone in epilepsy cases in comparison with interictal spikes. The first module implemented is preprocessing. Filtering is used as a first approach for noise cancellation such as Power Line Noise. For artifacts such as blinks, saccades and the heartbeats (the typical QRS complex) the cleaning process is more sophisticated. A different cleaning approach was followed for EEG and MEG data. ICA performed well on on EEG data in terms of distinguishing artifactual from brain sources. The automatic identification of artifactual components can be a complicated task. Partially, this is one of the reasons behind the implementation of the complex pipeline illustrated in Fig. 4.4. The other reason emerges from the necessity to reject only the most representative artifactual components without affecting useful brain signal. Wavelet Decomposition was applied in order to enhance signal's properties in time-frequency domain. As can been seen in Fig. 4.7, ICs representation on time-frequency domain improved the algorithm's results. On the other hand, on MEG recordings, SSP cleaned the artifacts sufficiently. As can been seen in Fig. 4.9 the artifactual components' rejection process did not affected the useful information, which in that case is the annotated interictal spikes. As explained in section 4.1 two more artifact cleaning approaches have been implemented but not integrated on the pipeline. In Fig. 4.11 the results of EMD and WD in terms of artifact cleaning are shown and compared. EMD

and WD are only used for ocular artifact cleaning because blinks and saccades contaminate signals on specific segments. The main merit of these approaches is that interfere with the components only on the contaminated segments, without affecting the brain activity. The interictal spikes were annotated by an epileptologist, meaning that no further job had to be done regarding their detection. On the contrary, HFOs had to be detected by us, so one of the main thesis goals was to develop a robust HFOs detection algorithm. As explained in section 4.2, the implemented algorithm is based on literature's previous implementations with an additional clustering module in order to stabilize and increase algorithm's robustness. Energy-based clustering serves as an extra filtering step for the detected HFOs since it distinguishes any erroneously detected spurious EEG or MEG events from real HFOs. In Fig. 4.14, 4.15 examples of detected EEG and MEG HFOs are shown, while in Fig. 4.16 an example of erroneous detection is shown in order to highlight the importance of visual inspection and clustering. Even though the algorithm detects real HFOs, it also includes spurious events that resemble HFOs. To put it differently, high sensitivity has been ensured in trade-off to a low specificity to obtain a large number of EoIs. Proceeding with the source analysis techniques, it is based on HFOs and interictal spikes. Averaging spikes for source localization is a well established approach. The same explorative approach was followed for HFOs-based source localization. Even though averaging of HFOs is not recommended, since they are not time-locked events , in Fig. 4.18a it is obvious that HFOs peaks' have been enhanced. On the contrary, averaging of MEG HFOs did not yielded sufficient results according to Fig. 4.18c where the HFOs peaks' are shown attenuated. For the FP a realistic head model with realistic connectivities was used for both HFOs-based and interictal spikes-based source localization, while the IP was solved by sLORETA on both cases. As can be seen in Fig. 4.28 and 4.29 EEG modality detectes accurately the right FCD, while it fails to detect the left FCD. On the other hand, MEG's superiority is shown on the detection of source activity around the vicinity of the left FCD. In Fig. 4.32 the combination of both modalities yields better results. The same trend is spotted on interictal spikes-base source localization according to Fig.

4.23 and 4.24. In that case, MEG yields more sufficient results for the detection of both FCDs. The complementary nature of EEG and MEG towards each other in EMEG can lead to a sufficient and stable result suppressing simultaneously any spurious brain signals not associated with the epileptic activity. Spikes-based source localization confirms HFOs indications about an EEG dominant epilepsy case. Overall, HFOs and interictal spikes successfully indicate the seizure onset zone, with HFOs being more accurate.

5.2 Conclusion

This thesis study proposes a subject specific pipeline for the exploration of scalp HFOs as epileptic indicators of seizure onset zone compared with interictal spikes on non-invasive EEG and MEG recordings. Detection scalp HFOs is an intriguing and not fully exploited task with many developing possibilities. Under this light we implemented an existed detection algorithm adding a clustering module for stabilizing and making the algorithm more robust. Furthermore, it takes into account the combined EMEG that can bring out the complementary information of the EEG and MEG, which enhances the main merits of each modality. Last but not least, the realistic head model that is used in source localization comprises six compartments (skin, skull compacta, skull spongiosa, cerebrospinal fluid (CSF), gray and white matter) including the anisotropies of the white matter and skull.

5.3 Future Work

As future work we propose machine learning and tensor decomposition, using PARAFAC, for a fully automated artifact detection and cleaning algorithm. Such an approach should facilitate and improve preprocessing approaches. Moreover, deep learning techniques could be used as HFOs detection algorithms in order to significantly decrease time complexity and human's involvement. Finally. the integrated pipeline could be applied on more epilepsy cases for validation.

Chapter 6

Comparison between toolboxes

There are many available open source software toolboxes or applications with online tutorials that can be used for EEG and/or MEG analysis. In this research work, two different open source tools have been used: FieldTrip [84] and Brainstorm [85]. In this chapter a comparison between the two toolboxes is made regarding the preprocessing approaches, denoising techniques and the source analysis. The comparison is made on this topics only, because they are in the scope of this thesis work.

To begin with, Fieldtrip runs only via Matlab, while Brainstorm gives the choice to the user to run it via Matlab or as a stand alone application. The two toolboxes are structured in a very different philosophy and they are addressed to users with a wide academic background. Specifically, Fieldtrip is a software only toolbox, so a basic Matlab coding knowledge is mandatory. On the other hand, Brainstorm is a user friendly application with an easy to learn GUI and does not require any programming knowledge, making it suitable for physicians.

Preprocessing

Regarding the proprocessing approach, both FieldTrip and Brainstorm offer quite similar choices in terms of processes. In FieldTrip, preprocessing is achieved using the built-in function *ft_preprocessing* (6.1a). To explain, processes like reading data, removing linear trend, subtracting baseline DC offset and applying filters (e.g. Notch or band-specific filters) are all implemented via *ft_preprocessing*. For data resampling and the conversion of 1st order gradiometers to 3rd order, the functions *ft_resampledata* and *ft_denoise_synthetic* were used, respectively. It is important to mention that the preprocessing option *cfg.dftfilter*, which removes line noise using Discrete Fourier Trans-

form (DFT), and the *cfg.dftfreq*, which accepts the line noise frequencies in Hz for DFT, does not run properly. Instead, a band-stop filter can be used with stop-band bandwidth on the frequencies of the line noise. Regarding epileptic data, the recordings are continuous, meaning that they are not segmented into portions or as they called trials. When using a toolbox, it is required to define if the data contain any trials or not. In FieldTrip this is defined by the preprocessing option *cfg.continuous*. An integral step of preprocessing is to detect any bad channels. Usually, most bad channels are identified by the technician during the measurements acquisition. However, it is always advisable to examine data for any noisy channels or jumps on channels. Visual inspection is necessary and should always be used. FieldTrip has implemented the function *ft_rejectvisual*, which illustrates the preprocessed data in all channels and allows the user to make a visual selection of the data that should be rejected (6.2b). Different metrics such as variance, kurtosis or z-value, for example (the metric is defined by the preprocessing option *cfg.metric*), are computed for each channel. The outliers denote bad or noisy channels. Although this function can be useful for indicating the bad channels, it is necessary to always review the results and inspect visually the data. In some cases, when source analysis is not in the scope of the study, the detected bad channels can be repaired. FieldTrip via the function *ft_channelrepair*, repairs the bad channels by replacing them with information given by the neighbors channels. The method used for repairing is selected by the preprocessing option *cfg.method*.

On the other hand, all the aforementioned processes are applied via GUI on Brainstorm (6.1b). To mention that CTF MEG/EEG system stores the recordings into two types of files: epoched (.ds) or continuous (_AUX.ds). In Brainstorm the files are saved as small blocks of recordings of a constant time length. All these time blocks are continuous, without any gap between them. By default Brainstorm imports the .ds folders as epoched, so it is necessary to manually switch from any epoched data to continuous data using the GUI command *Switch epoched/Continuous*. In order to correct the order of the gradiometers the process *Apply SSP & CTF compensation* must by applied. Consequently, the remaining aforementioned processes can

be applied. The processes are selected only via GUI and can be applied on one pass. Regarding bad channels detection, Brainstorm suggests to inspect the Power Spectrum Density of all channels. Usually, noisy or bad channels have greater PSD amplitude and stand out from the recordings (6.2a). For bad channels repair, Brainstorm provides the built-in process *Interpolate bad electrodes*, which allows the user to define the maximum distance between the neighbors. However, Brainstorm has integrated the Fieldtrip function *ft_channelrepair* which has been explained before, allowing users to choose different repairing methods.

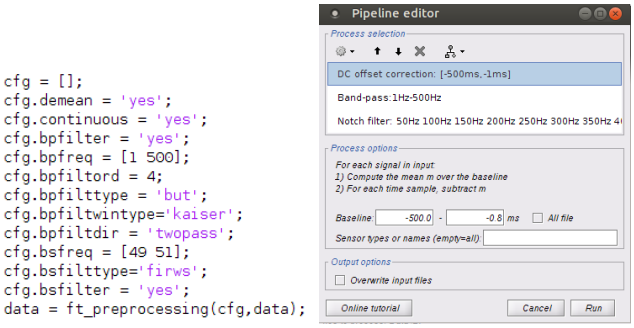

(a) (b)

Figure 6.1: Figure 6.1a shows a batch of code on FieldTrip, while figure 6.1b shows Brainstorm's GUI running the same processes as FieldTrip does.

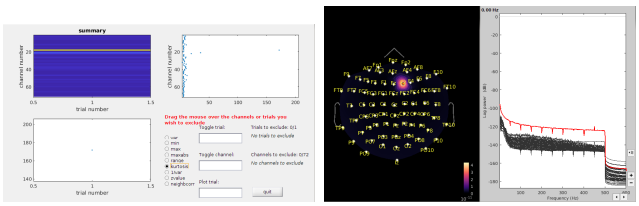

(a) (b)

Figure 6.2: Figure 6.2a shows FieldTrip's interface for detection and rejection of bad channles. Figure 6.2b shows Brainstorm's approach for bad channels detection. The PSD of all channels has been computed. The red channel which shows an increased amplitude is a bad channel and it can excluded from the further processing with right click on figure and selecting the option *Mark selected as bad*.

Artifact Cleaning Techniques

FieldTrip and Brainstorm contain built-in functions for automatic artifact detection. Both toolboxes can detect various artifacts; FieldTrip allows the user to detect ocular, cardiac and muscle activity or even detects jumps and channels that clip. Brainstorm, also detects subject movements, EOG and ECG events, while it supports the detection of custom events, not necessarily artifacts, based on the signal power in a specific frequency band. Component analysis techniques are used to clean the detected artifacts of both EEG and MEG recordings. FieldTrip supports variations of ICA, for instance binary ICA, Fast ICA, JADE, while algorithms such as SVD and PCA can be computed. Each method is accompanied by method-specific options, giving a lot of liberties to the user when applying a method. On the other hand, Brainstorm has integrated Infomax and JADE ICA only. The main difference between Brainstorm and FieldTrip regarding the artifact cleaning techniques is that the former uses extensively SSP for artifact cleaning on MEG recordings. Before apply SSP, is vital to detect the events that the algorithm will clear. In general, SSP algorithm is avoided when dealing with low-density EEG recordings.

Source Analysis

As has been extensively explained in Chapter 3, Source Analysis comprises of the Forward Problem and the Inverse Problem. At this point it is important to explain how the subject's anatomy is imported into the toolboxes. Brainstorm tutorials begin by importing subject's MRI and allows the user to calculate and apply the MNI transformation in order to use the normalized MNI coordinate system for concordance with literature. Brainstorm uses an affine co-registration with the MNI ICBM152 template from the SPM software as an extra step of normalization in order to obtain the MNI coordinates. The anatomical characteristics are saved on a separate tab from the recordings and are used for solving the FP 6.3b. On the other hand, in FieldTrip, because all variables are saved on MATLAB's workspace, it is recommended to import the subject's MRI when it comes to solving the FP and the IP.

The next step after importing, is to spatially align the anatomical MRI with head coordinates based on external fiducials or anatomical landmarks, using the built-in function *ft_volumerealign*. The next step belongs to a standard procedure that is always followed when solving FP, and it is the reslice of the anatomical MRI. FieldTrip uses the built-in function *ft_volumereslice*. All toolboxes co-register the given anatomical MRI with templates of typical adult heads and brains. Consequently, the volume has to be segmented into a specific number of compartments (3) and create the corresponding meshes. FieldTrip uses the built-in functions *ft_volumesegment* and *ft_prepare_mesh*, respectively. In Brainstorm the meshes can be produced by right-clicking on the subject's MRI, which is displayed on the anatomy tab. Also, Brainstorm has integrated FieldTrip's function *ft_volumesegment*. In both toolboxes, the geometry of the head is defined following the same standard procedure explained above.

A crucial part of solving the FP is the accurate construction of the head model. Both toolboxes support the widely used head models (3-shell sphere, single sphere, BEM) with FieldTrip providing more options. The major difference is that FieldTrip has implemented FEM, based on SimBio and DUNEuro, for EEG only, while Brainstorm's FEM based on DUNEuro is not yet available for public use. In both toolboxes FEM for MEG recordings has not yet implemented. The major disadvantage of both toolboxes is that they do not support combined EEG/MEG, which yields superior results in terms of source estimation as explained in chapter 4.

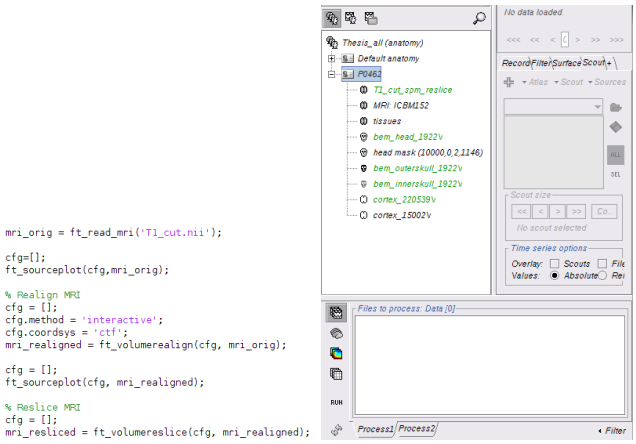

(a) (b)

Figure 6.3: Figure 6.3a shows a batch of code on FieldTrip about processing anatomical MRI, while figure 6.3b shows Brainstorm's GUI about processing amatomical MRI.

For solving the IP a variety of source reconstruction algorithms, such as minimum-norm solutions, beamformers and dipole modeling, are provided by the two toolboxes. An important aspect of Brainstorm is that it has incorporated FieldTrip built-in functions such as *ft_dipolefitting* and *ft_sourceanalysis*, allowing the user to apply more source reconstruction algorithms such as eLORETA for example, which is not implemented on Brainstorm. Moreover, Brainstorm has integrated the toolbox BEst – "Brain Entropy in space and time", that implements several EEG/MEG source localization techniques within the "Maximum Entropy on the Mean (MEM)" framework. These methods are effective on estimating brain activity sources of EEG/MEG together with their spatial extent along the cortical surface. For instance, when it comes to HFOs source localization, wMEM has been proved to yield accurate results because it was designed to localize single-trial events of oscillatory transient cortical activity, usually associated with low signal-to-noise ratio. Finally, on FieldTrip the methods DICS (Dynamic Imaging of coherent sources) and PCC (partial canonical correlation/coherence) are for frequency or time-frequency domain data.

Conclusion

The main differences between FieldTrip and Brainstorm can be summarized on the users experience. FieldTrip can be confusing at parts when coding skills are not fully developed, but it allows the user to extract easily the data and processes them further. On the contrary Brainstorm is quite suitable for users with none or limited coding background, while it is not always straightforward to extract the desired signals for further processing. The main merit of Brainstorm is the general organization of the application, which automatically positions the figures and allows multiple views of the same data, with common x-axis (mainly representing time). Visualizations are extremely valuable when it comes to signal processing and data review. Brainstorm creates accurate visualizations and provides an easy navigation system across them, facilitating the comparison and the review of the results.

Bibliography

[1] B Azzerboni, M Carpentieri, F La Foresta, and FC Morabito. Neural-ica and wavelet transform for artifacts removal in surface emg. In *2004 IEEE International Joint Conference on Neural Networks (IEEE Cat. No. 04CH37541)*, volume 4, pages 3223–3228. IEEE, 2004.

[2] Salvatore Calcagno, Fabio La Foresta, and Mario Versaci. Independent component analysis and discrete wavelet transform for artifact removal in biomedical signal processing. *American Journal of Applied Sciences*, 11(1):57, 2014.

[3] Fengyu Cong, Qiu-Hua Lin, Li-Dan Kuang, Xiao-Feng Gong, Piia Astikainen, and Tapani Ristaniemi. Tensor decomposition of eeg signals: a brief review. *Journal of neuroscience methods*, 248:59–69, 2015.

[4] Maarten De Vos, Lieven De Lathauwer, Bart Vanrumste, Sabine Van Huffel, and Wim Van Paesschen. Canonical decomposition of ictal scalp eeg and accurate source localisation: Principles and simulation study. *Computational intelligence and neuroscience*, 2007, 2007.

[5] Hanna Becker, Pierre Comon, and Laurent Albera. Tensor-based preprocessing of combined eeg/meg data. In *2012 Proceedings of the 20th European Signal Processing Conference (EUSIPCO)*, pages 275–279. IEEE, 2012.

[6] Evrim Acar, Canan Aykut-Bingol, Haluk Bingol, Rasmus Bro, and Bülent Yener. Multiway analysis of epilepsy tensors. *Bioinformatics*, 23(13):i10–i18, 2007.

[7] Sergey Burnos, Peter Hilfiker, Oguzkan Sürücü, Felix Scholkmann, Niklaus Krayenbühl, Thomas Grunwald, and Johannes Sarnthein. Hu-

man intracranial high frequency oscillations (hfos) detected by automatic time-frequency analysis. *PloS one*, 9(4):e94381, 2014.

[8] Stephen V Gliske, Zachary T Irwin, Kathryn A Davis, Kinshuk Sahaya, Cynthia Chestek, and William C Stacey. Universal automated high frequency oscillation detector for real-time, long term eeg. *Clinical Neurophysiology*, 127(2):1057–1066, 2016.

[9] Andrew B Gardner, Greg A Worrell, Eric Marsh, Dennis Dlugos, and Brian Litt. Human and automated detection of high-frequency oscillations in clinical intracranial eeg recordings. *Clinical neurophysiology*, 118(5):1134–1143, 2007.

[10] Katsuhiro Kobayashi, Yoshiaki Watanabe, Takushi Inoue, Makio Oka, Harumi Yoshinaga, and Yoko Ohtsuka. Scalp-recorded high-frequency oscillations in childhood sleep-induced electrical status epilepticus. *Epilepsia*, 51(10):2190–2194, 2010.

[11] Danilo Bernardo, Hiroki Nariai, Shaun A Hussain, Raman Sankar, Noriko Salamon, Darcy A Krueger, Mustafa Sahin, Hope Northrup, E Martina Bebin, Joyce Y Wu, et al. Visual and semi-automatic non-invasive detection of interictal fast ripples: A potential biomarker of epilepsy in children with tuberous sclerosis complex. *Clinical Neurophysiology*, 129(7):1458–1466, 2018.

[12] Christos Papadelis, Eleonora Tamilia, Steven Stufflebeam, Patricia E Grant, Joseph R Madsen, Phillip L Pearl, and Naoaki Tanaka. Interictal high frequency oscillations detected with simultaneous magnetoencephalography and electroencephalography as biomarker of pediatric epilepsy. *JoVE (Journal of Visualized Experiments)*, (118):e54883, 2016.

[13] Jiayang Guo, Kun Yang, Hongyi Liu, Chunli Yin, Jing Xiang, Hailong Li, Rongrong Ji, and Yue Gao. A stacked sparse autoencoder-based detector for automatic identification of neuromagnetic high fre-

quency oscillations in epilepsy. *IEEE transactions on medical imaging*, 37(11):2474–2482, 2018.

[14] Marco De Curtis and Giuliano Avanzini. Interictal spikes in focal epileptogenesis. *Progress in neurobiology*, 63(5):541–567, 2001.

[15] Moritz Dannhauer, Benjamin Lanfer, Carsten H Wolters, and Thomas R Knösche. Modeling of the human skull in eeg source analysis. *Human brain mapping*, 32(9):1383–1399, 2011.

[16] Marios Antonakakis. Combined eeg/meg source analysis for presurgical epilepsy diagnosis using calibrated realistic volume conductor model.

[17] Ü Aydin, S Rampp, A Wollbrink, H Kugel, J-H Cho, Thomas R Knösche, C Grova, J Wellmer, and CH Wolters. Zoomed mri guided by combined eeg/meg source analysis: a multimodal approach for optimizing presurgical epilepsy work-up and its application in a multi-focal epilepsy patient case study. *Brain topography*, 30(4):417–433, 2017.

[18] Ümit Aydin, Johannes Vorwerk, Matthias Dümpelmann, Philipp Küpper, Harald Kugel, Marcel Heers, Jörg Wellmer, Christoph Kellinghaus, Jens Haueisen, Stefan Rampp, et al. Combined eeg/meg can outperform single modality eeg or meg source reconstruction in presurgical epilepsy diagnosis. *PloS one*, 10(3):e0118753, 2015.

[19] Aljoscha Thomschewski, Ana-Sofía Hincapié, and Birgit Frauscher. Localization of the epileptogenic zone using high frequency oscillations. *Frontiers in neurology*, 10:94, 2019.

[20] Ida A Nissen, Nicole EC van Klink, Maeike Zijlmans, Cornelis J Stam, and Arjan Hillebrand. Brain areas with epileptic high frequency oscillations are functionally isolated in meg virtual electrode networks. *Clinical Neurophysiology*, 127(7):2581–2591, 2016.

[21] Hans O Lüders, Imad Najm, Dileep Nair, Peter Widdess-Walsh, and William Bingman. The epileptogenic zone: general principles. *Epileptic disorders*, 8(2):1–9, 2006.

[22] Kevin J Staley and F Edward Dudek. Interictal spikes and epileptogenesis. *Epilepsy Currents*, 6(6):199–202, 2006.

[23] Felix Rosenow and Hans Lüders. Presurgical evaluation of epilepsy. *Brain*, 124(9):1683–1700, 2001.

[24] Anatol Bragin, Charles L Wilson, Joyel Almajano, Istvan Mody, and Jerome Engel Jr. High-frequency oscillations after status epilepticus: epileptogenesis and seizure genesis. *Epilepsia*, 45(9):1017–1023, 2004.

[25] Nikolai Axmacher, Christian E Elger, and Juergen Fell. Ripples in the medial temporal lobe are relevant for human memory consolidation. *Brain*, 131(7):1806–1817, 2008.

[26] Maeike Zijlmans, Premysl Jiruska, Rina Zelmann, Frans SS Leijten, John GR Jefferys, and Jean Gotman. High-frequency oscillations as a new biomarker in epilepsy. *Annals of neurology*, 71(2):169–178, 2012.

[27] Jerome Engel Jr, Anatol Bragin, Richard Staba, and Istvan Mody. High-frequency oscillations: what is normal and what is not? *Epilepsia*, 50(4):598–604, 2009.

[28] Maeike Zijlmans, Gregory A Worrell, Matthias Dümpelmann, Thomas Stieglitz, Andrei Barborica, Marcel Heers, Akio Ikeda, Naotaka Usui, and Michel Le Van Quyen. How to record high-frequency oscillations in epilepsy: a practical guideline. *Epilepsia*, 58(8):1305–1315, 2017.

[29] Elena Urrestarazu, Rahul Chander, Francçois Dubeau, and Jean Gotman. Interictal high-frequency oscillations (100–500 hz) in the intracerebral eeg of epileptic patients. *Brain*, 130(9):2354–2366, 2007.

[30] Saeid Sanei and Jonathon A Chambers. *EEG signal processing*. John Wiley & Sons, 2013.

[31] Matti Hämäläinen, Riitta Hari, Risto J Ilmoniemi, Jukka Knuutila, and Olli V Lounasmaa. Magnetoencephalography—theory, instrumentation, and applications to noninvasive studies of the working human brain. *Reviews of modern Physics*, 65(2):413, 1993.

[32] Peter Hansen, Morten Kringelbach, and Riitta Salmelin. *MEG: an introduction to methods*. Oxford university press, 2010.

[33] Riitta Hari and Aina Puce. *MEG-EEG Primer*. Oxford University Press, 2017.

[34] Ming-Xiong Huang, Tao Song, Donald J Hagler Jr, Igor Podgorny, Veikko Jousmaki, Li Cui, Kathleen Gaa, Deborah L Harrington, Anders M Dale, Roland R Lee, et al. A novel integrated meg and eeg analysis method for dipolar sources. *Neuroimage*, 37(3):731–748, 2007.

[35] M Hamalainen and R Hari. Rj lmoniemi, j. knuutila, and ov lounasmaa,"magnetoencephalography—theory, instrumentation and applications to noninvasive studies of the working human brain,". *Rev. Mod. Phys*, 65:413–497, 1993.

[36] George Dassios, Athanassios S Fokas, and Demetra Hadjiloizi. On the complementarity of electroencephalography and magnetoencephalography. *Inverse Problems*, 23(6):2541, 2007.

[37] Jens Haueisen, Michael Funke, Daniel Güllmar, and Roland Eichardt. Tangential and radial epileptic spike activity: different sensitivity in eeg and meg. *Journal of Clinical Neurophysiology*, 29(4):327–332, 2012.

[38] Ümit Aydin, Johannes Vorwerk, Philipp Küpper, Marcel Heers, Harald Kugel, Andreas Galka, Laith Hamid, Jörg Wellmer, Christoph Kellinghaus, Stefan Rampp, et al. Combining eeg and meg for the reconstruction of epileptic activity using a calibrated realistic volume conductor model. *PLoS One*, 9(3):e93154, 2014.

[39] Manfred Fuchs, Michael Wagner, Hans-Aloys Wischmann, Thomas Köhler, Annette Theißen, Ralf Drenckhahn, and Helmut Buchner. Improving source reconstructions by combining bioelectric and biomagnetic data. *Electroencephalography and clinical neurophysiology*, 107(2):93–111, 1998.

[40] Masaki Iwasaki, Elia Pestana, Richard C Burgess, Hans O Lüders, Hiroshi Shamoto, and Nobukazu Nakasato. Detection of epileptiform activity by human interpreters: blinded comparison between electroencephalography and magnetoencephalography. *Epilepsia*, 46(1):59–68, 2005.

[41] S Knake, E Halgren, H Shiraishi, K Hara, HM Hamer, PE Grant, VA Carr, D Foxe, S Camposano, E Busa, et al. The value of multichannel meg and eeg in the presurgical evaluation of 70 epilepsy patients. *Epilepsy research*, 69(1):80–86, 2006.

[42] Joachim Gross, Sylvain Baillet, Gareth R Barnes, Richard N Henson, Arjan Hillebrand, Ole Jensen, Karim Jerbi, Vladimir Litvak, Burkhard Maess, Robert Oostenveld, et al. Good practice for conducting and reporting meg research. *Neuroimage*, 65:349–363, 2013.

[43] Alan V Oppenheim. *Discrete-time signal processing*. Pearson Education India, 1999.

[44] Hervé Abdi and Lynne J Williams. Principal component analysis. *Wiley interdisciplinary reviews: computational statistics*, 2(4):433–459, 2010.

[45] Jon Shlens. A tutorial on principal component analysis: derivation, discussion and singular value decomposition. *Mar*, 25(1):16, 2003.

[46] Marios Antonakakis, Giorgos Giannakakis, Manolis Tsiknakis, Sifis Micheloyannis, and Michalis Zervakis. Synchronization coupling investigation using ica cluster analysis in resting meg signals in reading difficulties. In *13th IEEE International Conference on BioInformatics and BioEngineering*, pages 1–5. IEEE, 2013.

[47] Simon Haykin and Zhe Chen. The cocktail party problem. *Neural computation*, 17(9):1875–1902, 2005.

[48] Aapo Hyvärinen and Erkki Oja. Independent component analysis: algorithms and applications. *Neural networks*, 13(4-5):411–430, 2000.

[49] Anthony J Bell and Terrence J Sejnowski. An information-maximization approach to blind separation and blind deconvolution. *Neural computation*, 7(6):1129–1159, 1995.

[50] Aapo Hyvärinen and Erkki Oja. A fast fixed-point algorithm for independent component analysis. *Neural computation*, 9(7):1483–1492, 1997.

[51] J-F Cardoso. Infomax and maximum likelihood for blind source separation. *IEEE Signal processing letters*, 4(4):112–114, 1997.

[52] Barak A Pearlmutter and Lucas C Parra. Maximum likelihood blind source separation: A context-sensitive generalization of ica. In *Advances in neural information processing systems*, pages 613–619, 1997.

[53] Shun-Ichi Amari. Natural gradient works efficiently in learning. *Neural computation*, 10(2):251–276, 1998.

[54] Norden E Huang, Zheng Shen, Steven R Long, Manli C Wu, Hsing H Shih, Quanan Zheng, Nai-Chyuan Yen, Chi Chao Tung, and Henry H Liu. The empirical mode decomposition and the hilbert spectrum for nonlinear and non-stationary time series analysis. *Proceedings of the Royal Society of London. Series A: mathematical, physical and engineering sciences*, 454(1971):903–995, 1998.

[55] Job P Lindsen and Joydeep Bhattacharya. Correction of blink artifacts using independent component analysis and empirical mode decomposition. *Psychophysiology*, 47(5):955–960, 2010.

[56] Nazareth P Castellanos and Valeri A Makarov. Recovering eeg brain signals: artifact suppression with wavelet enhanced independent component analysis. *Journal of neuroscience methods*, 158(2):300–312, 2006.

[57] Mikko A Uusitalo and Risto J Ilmoniemi. Signal-space projection method for separating meg or eeg into components. *Medical and Biological Engineering and Computing*, 35(2):135–140, 1997.

[58] G Nolte and MS Hämäläinen. Partial signal space projection for artefact removal in meg measurements: a theoretical analysis. *Physics in Medicine & Biology*, 46(11):2873, 2001.

[59] Richard J Staba, Charles L Wilson, Anatol Bragin, Itzhak Fried, and Jerome Engel Jr. Quantitative analysis of high-frequency oscillations (80–500 hz) recorded in human epileptic hippocampus and entorhinal cortex. *Journal of neurophysiology*, 88(4):1743–1752, 2002.

[60] Benoît Crépon, Vincent Navarro, Dominique Hasboun, Stéphane Clemenceau, Jacques Martinerie, Michel Baulac, Claude Adam, and Michel Le Van Quyen. Mapping interictal oscillations greater than 200 hz recorded with intracranial macroelectrodes in human epilepsy. *Brain*, 133(1):33–45, 2010.

[61] Gwenael Birot, Amar Kachenoura, Laurent Albera, Christian Bénar, and Fabrice Wendling. Automatic detection of fast ripples. *Journal of neuroscience methods*, 213(2):236–249, 2013.

[62] Matthias Dümpelmann, Julia Jacobs, Karolin Kerber, and Andreas Schulze-Bonhage. Automatic 80–250 hz "ripple" high frequency oscillation detection in invasive subdural grid and strip recordings in epilepsy by a radial basis function neural network. *Clinical Neurophysiology*, 123(9):1721–1731, 2012.

[63] Rina Zelmann, F Mari, J Jacobs, M Zijlmans, R Chander, and J Gotman. Automatic detector of high frequency oscillations for human recordings with macroelectrodes. In *2010 Annual International Conference of the IEEE Engineering in Medicine and Biology*, pages 2329–2333. IEEE, 2010.

[64] Sahbi Chaibi, Tarek Lajnef, Zied Sakka, Mounir Samet, and Abdennaceur Kachouri. A comparaison of methods for detection of high frequency oscillations (hfos) in human intacerberal eeg recordings. *American Journal of Signal Processing*, 3(2):25–34, 2013.

[65] Pariya Salami, Maxime Lévesque, Jean Gotman, and Massimo Avoli. A comparison between automated detection methods of high-frequency oscillations (80–500 hz) during seizures. *Journal of neuroscience methods*, 211(2):265–271, 2012.

[66] Tomoyuki Akiyama, Bláthnaid McCoy, Cristina Y Go, Ayako Ochi, Irene M Elliott, Mari Akiyama, Elizabeth J Donner, Shelly K Weiss, O Carter Snead III, James T Rutka, et al. Focal resection of fast ripples on extraoperative intracranial eeg improves seizure outcome in pediatric epilepsy. *Epilepsia*, 52(10):1802–1811, 2011.

[67] Yaguo Lei. *Intelligent fault diagnosis and remaining useful life prediction of rotating machinery*. Butterworth-Heinemann, 2016.

[68] Stuart Lloyd. Least squares quantization in pcm. *IEEE transactions on information theory*, 28(2):129–137, 1982.

[69] A David. Vassilvitskii s.: K-means++: The advantages of careful seeding. In *18th annual ACM-SIAM symposium on Discrete algorithms (SODA), New Orleans, Louisiana*, pages 1027–1035, 2007.

[70] Roberta Grech, Tracey Cassar, Joseph Muscat, Kenneth P Camilleri, Simon G Fabri, Michalis Zervakis, Petros Xanthopoulos, Vangelis Sakkalis, and Bart Vanrumste. Review on solving the inverse problem in eeg source analysis. *Journal of neuroengineering and rehabilitation*, 5(1):25, 2008.

[71] Hannah McCann, Giampaolo Pisano, and Leandro Beltrachini. Variation in reported human head tissue electrical conductivity values. *Brain topography*, 32(5):825–858, 2019.

[72] Hans Hallez, Bart Vanrumste, Roberta Grech, Joseph Muscat, Wim De Clercq, Anneleen Vergult, Yves D'Asseler, Kenneth P Camilleri, Simon G Fabri, Sabine Van Huffel, et al. Review on solving the forward problem in eeg source analysis. *Journal of neuroengineering and rehabilitation*, 4(1):46, 2007.

[73] Carsten H Wolters, Alfred Anwander, Xavier Tricoche, D Weinstein, Martin A Koch, and Robert S Macleod. Influence of tissue conductivity anisotropy on eeg/meg field and return current computation in a realistic head model: a simulation and visualization study using high-resolution finite element modeling. *NeuroImage*, 30(3):813–826, 2006.

[74] Johannes Vorwerk, Jae-Hyun Cho, Stefan Rampp, Hajo Hamer, Thomas R Knösche, and Carsten H Wolters. A guideline for head volume conductor modeling in eeg and meg. *NeuroImage*, 100:590–607, 2014.

[75] Sylvain Baillet. Forward and inverse problems of meg/eeg., 2014.

[76] Yohan Attal and Denis Schwartz. Assessment of subcortical source localization using deep brain activity imaging model with minimum norm operators: a meg study. *PLoS One*, 8(3):e59856, 2013.

[77] Michael Rullmann, Alfred Anwander, Moritz Dannhauer, Simon K Warfield, Frank H Duffy, and Carsten H Wolters. Eeg source analysis of epileptiform activity using a 1 mm anisotropic hexahedra finite element head model. *NeuroImage*, 44(2):399–410, 2009.

[78] Felix Lucka, Sampsa Pursiainen, Martin Burger, and Carsten H Wolters. Hierarchical bayesian inference for the eeg inverse problem using realistic fe head models: depth localization and source separation for focal primary currents. *NeuroImage*, 61(4):1364–1382, 2012.

[79] Roberto Domingo Pascual-Marqui et al. Standardized low-resolution brain electromagnetic tomography (sloreta): technical details. *Methods Find Exp Clin Pharmacol*, 24(Suppl D):5–12, 2002.

[80] Dragoljub Gajic, Zeljko Djurovic, Stefano Di Gennaro, and Fredrik Gustafsson. Classification of eeg signals for detection of epileptic seizures based on wavelets and statistical pattern recognition. *Biomedical Engineering: Applications, Basis and Communications*, 26(02):1450021, 2014.

[81] Rina Zelmann, Maeike Zijlmans, Julia Jacobs, Claude-E Châtillon, and Jean Gotman. Improving the identification of high frequency oscillations. *Clinical Neurophysiology*, 120(8):1457–1464, 2009.

[82] Antonino Greco, Nadia Mammone, F Carlo Morabito, and Mario Versaci. Kurtosis, renyi's entropy and independent component scalp maps for the automatic artifact rejection from eeg data. *International Journal of Signal Processing*, 2(4):240–244, 2006.

[83] Marios Antonakakis, Michalis Zervakis, Catharina EM van Beijsterveldt, Dorret I Boomsma, Eco JC De Geus, Sifis Micheloyannis, and Dirk JA Smit. Genetic effects on source level evoked and induced oscillatory brain responses in a visual oddball task. *Biological psychology*, 114:69–80, 2016.

[84] Robert Oostenveld, Pascal Fries, Eric Maris, and Jan-Mathijs Schoffelen. Fieldtrip: open source software for advanced analysis of meg, eeg, and invasive electrophysiological data. *Computational intelligence and neuroscience*, 2011, 2011.

[85] François Tadel, Sylvain Baillet, John C Mosher, Dimitrios Pantazis, and Richard M Leahy. Brainstorm: a user-friendly application for meg/eeg analysis. *Computational intelligence and neuroscience*, 2011, 2011.